

# Quantifying Atmospheric Methane Point Sources with High-Resolution Satellite Observations

A DISSERTATION PRESENTED  
BY  
DANIEL J. VARON  
TO  
THE DEPARTMENT OF ENGINEERING AND APPLIED SCIENCE  
  
IN PARTIAL FULFILLMENT OF THE REQUIREMENTS  
FOR THE DEGREE OF  
DOCTOR OF PHILOSOPHY  
IN THE SUBJECT OF  
ENVIRONMENTAL SCIENCE AND ENGINEERING  
  
HARVARD UNIVERSITY  
CAMBRIDGE, MASSACHUSETTS  
MAY 2020

©2020 – DANIEL J. VARON  
ALL RIGHTS RESERVED.

# Quantifying Atmospheric Methane Point Sources with High-Resolution Satellite Observations

## ABSTRACT

The GHGSat-D demonstration satellite instrument launched in 2016 and operated by GHGSat Inc. has unlocked the possibility of monitoring atmospheric methane emissions at the facility level from space. Previous satellite missions for methane focused on improving global- and regional-scale understanding of concentrations and emissions, which required instruments with global coverage and kilometer-scale pixels. Among these were the SCIAMACHY ( $60 \times 30 \text{ km}^2$  pixels) and GOSAT ( $\sim 10\text{-km}$  resolution) instruments, which dramatically improved methane source and sink accounting, but were by design unable to resolve individual point sources. The 2017 launch of TROPOMI aboard the Sentinel-5P satellite enabled global methane mapping at unprecedented 7-km resolution, but this is still too coarse to detect all but the most extreme methane point sources. In contrast, the GHGSat measurement concept trades spatial coverage for orders of magnitude finer imaging resolution. The demonstration instrument observes methane at  $\leq 50\text{-m}$  resolution over targeted  $12 \times 12 \text{ km}^2$  domains. These measurements offer new capabilities for national emission reporting and global methane budget analyses.

Here we develop source rate retrieval algorithms for interpreting high-resolution satellite observations of methane point source plumes in terms of the corresponding facility-level emissions, and evaluate the algorithms' performance on synthetic plume datasets generated by large eddy simulation (Chapter 1). We apply these algorithms to the GHGSat-D discovery of anomalously large methane emissions in an oil/gas field in Central Asia to estimate emissions from individual oil/gas production facilities (Chapter 2). We then develop wind-adjusted time-averaging techniques to improve the GHGSat detection threshold by combining plume observations from multiple satellite passes, and use the techniques to estimate time-averaged methane emissions from individual coal mine vents in the United States, Australia, and China (Chapter 3).

# Contents

1	QUANTIFYING METHANE POINT SOURCES FROM FINE-SCALE SATELLITE OBSERVATIONS OF ATMOSPHERIC METHANE PLUMES	1
1.1	Introduction . . . . .	3
1.2	Review of methods for retrieving point sources from observations of column plumes . . . . .	5
1.3	Synthetic GHGSat observations of methane plumes . . . . .	9
1.4	Inadequacy of the Gaussian plume and source pixel methods . . . . .	12
1.5	Computing the source rate by the IME method . . . . .	14
1.6	Computing the source rate by the CSF method . . . . .	22
1.7	Inferring the effective wind speed from meteorological databases . . . . .	25
1.8	Conclusions . . . . .	28
2	SATELLITE DISCOVERY OF ANOMALOUSLY LARGE METHANE POINT SOURCES FROM OIL/GAS PRODUCTION	31
2.1	Introduction . . . . .	32
2.2	GHGSat-D observations . . . . .	34
2.3	TROPOMI observations . . . . .	38
2.4	Source rate quantification methods . . . . .	39
2.5	Source rate estimates . . . . .	42
2.6	Conclusion . . . . .	45
3	QUANTIFYING TIME-AVERAGED METHANE EMISSIONS FROM INDIVIDUAL COAL MINE VENTS WITH GHGSAT-D SATELLITE OBSERVATIONS	47
3.1	Introduction . . . . .	49
3.2	Materials and methods . . . . .	50
3.3	Results and discussion . . . . .	60
	APPENDIX A SUPPLEMENTAL INFORMATION FOR CHAPTER 2	66
A.1	GHGSat measurements and retrievals . . . . .	73
A.2	Quantifying TROPOMI plumes . . . . .	78
A.3	Plume mask for GHGSat-D plume quantification . . . . .	79
A.4	GHGSat-D source rate error analysis . . . . .	80

A.5	TROPOMI source rate error analysis . . . . .	83
APPENDIX B SUPPLEMENTAL INFORMATION FOR CHAPTER 3		85
B.1	Source rate retrieval error analysis . . . . .	85
REFERENCES		99

The following authors contributed to Chapter 1:

Daniel J. Jacob, Jason McKeever, Berke O. A. Durak, Yan Xia, and Yi Huang

The following authors contributed to Chapter 2:

Jason McKeever, Dylan Jervis, Joannes D. Maasakkers, Sudhanshu Pandey, Sander Houweling, Ilse Aben, Tia Scarpelli, Daniel J. Jacob

The following authors contributed to Chapter 3:

Daniel J. Jacob, Dylan Jervis, Jason McKeever

# Listing of figures

1.1	Figure 1.1. Methane plume pseudo-observations generated by LES . . . . .	12
1.2	Figure 1.2. Gaussian plume fitting for a large CO <sub>2</sub> power plant plume . . . . .	13
1.3	Figure 1.3. Procedure for constructing plume masks . . . . .	15
1.4	Figure 1.4. Relationship between effective and 10-m winds in the IME method . .	18
1.5	Figure 1.5. IME retrieval algorithm flow chart . . . . .	20
1.6	Figure 1.6. Evaluation of the IME method on LES test data . . . . .	21
1.7	Figure 1.7. Relationship between effective and 10-m winds in the CSF method . .	23
1.8	Figure 1.8. Evaluation of the CSF method on LES test data . . . . .	24
1.9	Figure 1.9. Evaluation of GEOS-FP for estimating local 10-m winds . . . . .	27
2.1	Figure 2.1. GHGSat-D observations of Korpezhe oil/gas field methane plumes . .	35
2.2	Figure 2.2. Emissions inventory data and surface imagery for the GHGSat scene .	37
2.3	Figure 2.3. TROPOMI observations of Korpezhe oil/gas field methane plumes . .	38
2.4	Figure 2.4. Time series of emissions from the Korpezhe 12 × 12 km <sup>2</sup> scene . . . .	43
3.1	Figure 3.1. GHGSat-D single-pass plume observations of the San Juan mine . . .	52
3.2	Figure 3.2. Evaluation of GEOS-FP and DarkSky local wind estimates . . . . .	54
3.3	Figure 3.3. Relationships between time-averaged effective and 10-m winds . . . .	59
3.4	Figure 3.4. Time-averaged methane plumes from three coal mine vents . . . . .	61
A.1	Figure A.1. DigitalGlobe imagery of pipeline near source #2 under construction .	68
A.2	Figure A.2. Relationships between effective and 10-m winds for Korpezhe . . . .	69
A.3	Figure A.3. Summary of GHGSat-D source rate retrievals for Korpezhe . . . .	70
A.4	Figure A.4. Full GHGSat-D column retrieval for 13 January 2019 observation . .	71
A.5	Figure A.5. Evaluation of scaling error from GHGSat-D retrieval imperfections .	72

TO MY FRIENDS AND FAMILY, WHO MADE THIS POSSIBLE.

# Acknowledgments

LOREM IPSUM DOLOR SIT AMET, consectetuer adipiscing elit. Morbi commodo, ipsum sed pharetra gravida, orci magna rhoncus neque, id pulvinar odio lorem non turpis. Nullam sit amet enim. Suspendisse id velit vitae ligula volutpat condimentum. Aliquam erat volutpat. Sed quis velit. Nulla facilisi. Nulla libero. Vivamus pharetra posuere sapien. Nam consectetuer. Sed aliquam, nunc eget euismod ullamcorper, lectus nunc ullamcorper orci, fermentum bibendum enim nibh eget ipsum. Donec porttitor ligula eu dolor. Maecenas vitae nulla consequat libero cursus venenatis. Nam magna enim, accumsan eu, blandit sed, blandit a, eros.

# 1

# Quantifying Methane Point Sources from Fine-scale Satellite Observations of Atmospheric Methane Plumes

ANTHROPOGENIC METHANE EMISSIONS ORIGINATE from a large number of relatively small point sources. The planned GHGSat satellite fleet aims to quantify emissions from individual point sources by measuring methane column plumes over selected  $\sim 10 \times 10 \text{ km}^2$  domains with  $\leq 50 \times 50 \text{ m}^2$  pixel resolution and 1–5% measurement precision. Here we develop algorithms for retrieving point source rates from such measurements. We simulate a large ensemble of instantaneous methane column plumes at  $50 \times 50 \text{ m}^2$  pixel resolution for a range of atmospheric conditions using the Weather Research and Forecasting model (WRF) in large eddy simulation (LES) mode and adding instrument noise. We show that standard methods to infer source rates by Gaussian plume inversion or source pixel mass balance are prone to large errors because the turbulence cannot be properly parameterized on the small scale of instantaneous methane plumes. The integrated mass enhancement (IME) method, which relates total plume mass to source rate, and the cross-sectional flux (CSF) method, which infers source rate from fluxes across plume transects, are better adapted to the problem. We show that the IME method with local measurements of the 10-m wind speed can infer source rates with an error of  $0.07\text{--}0.17 \text{ t h}^{-1} + 5\text{--}12\%$  depending on instrument precision

(1–5%). The CSF method has slightly larger errors ( $0.07\text{--}0.26 \text{ t h}^{-1}$  + 8–12%) but a simpler physical basis. For comparison, point sources larger than  $0.3 \text{ t h}^{-1}$  contribute more than 75% of methane emissions reported to the U.S. Greenhouse Gas Reporting Program. Additional error applies if local wind speed measurements are not available and may dominate the overall error at low wind speeds. Low winds are beneficial for source detection but detrimental for source quantification.

## 1.1 INTRODUCTION

Satellite instruments can measure atmospheric methane columns from solar backscatter in the short-wave infrared (SWIR) with near-uniform sensitivity down to the surface (Frankenberg et al., 2005). There is considerable interest in using these measurements to quantify methane emissions (Jacob et al., 2016). Most current and planned instruments have pixel resolutions of 1–10 km and column precisions of 0.1–1% (Bovensmann et al., 1999; Butz et al., 2011; Veefkind et al., 2012; Polonsky et al., 2014; Kuze et al., 2016). Jacob et al. (2016) show that these measurements can successfully map regional methane emissions but have limited ability to resolve individual methane point sources, even with imaging capabilities, because the sources tend to be relatively small and spatially clustered (e.g., oil/gas fields, livestock operations, landfills, coal mine vents). The GHGSat microsatellite fleet (Germain et al., 2017; McKeever et al., 2017) aims to address this gap by observing methane columns over selected scenes of order  $10 \times 10 \text{ km}^2$  with  $\leq 50 \times 50 \text{ m}^2$  effective pixel resolution and moderate precision (1–5%). Here we present algorithms for interpreting the instantaneous plumes observed by this instrument in terms of the implied point source (facility-level) emissions and estimate the associated errors and detection limits as a function of instrument precision.

Aircraft remote sensing of methane columns over oil/gas and coal mining facilities shows that the instantaneous plumes have irregular shapes and detectable sizes of order 0.1–1 km (Thorpe et al., 2016; Thompson et al., 2015, 2016; Frankenberg et al., 2016). A standard method used to re-

trieve source rates from plume observations is to assume Gaussian plume behaviour, as expected from statistically averaged turbulence (Bovensmann et al., 2010; Krings et al., 2011, 2013; Rayner et al., 2014; Fioletov et al., 2015; Nassar et al., 2017; Schwandner et al., 2017). This method may induce large errors for small instantaneous plumes, which generally do not follow steady-state Gaussian behaviour. Several authors have addressed this difficulty. Krings et al. (2011, 2013) proposed a cross-sectional flux (CSF) method to derive the source rate as the product of the local wind and the concentration integrated over a plume cross section, expanding on a similar method used for in situ plume measurements (White et al., 1976; Cambaliza et al., 2014; Conley et al., 2016). Jacob et al. (2016) described a mass balance method for inferring the source rate solely based on the enhancement in the source pixel. Frankenberg et al. (2016) inferred the source rate empirically from the total detectable mass of methane in the plume (integrated mass enhancement or IME).

A common feature of all these methods for retrieving the point source rate  $Q$  from plume observations is their need for independent knowledge of the wind speed  $U$  driving transport of the plume. In the CSF method applied to in situ aircraft observations, methane and local wind speed are measured concurrently (Conley et al., 2016). In remote sensing, however, the wind speed for the instantaneous column plume is not directly measured and may be variable both vertically and horizontally across the plume.

Here we use observing system simulation experiments to develop algorithms for retrieving individual point source rates from fine-scale satellite observations of instantaneous methane plumes. We review previously used plume inversion methods and show with large eddy simulations (LES) that the IME and CSF methods are best suited to the problem. We further develop the IME method to provide a physical basis for its general application. We consider different combinations of instrument precision, meteorological environment, and wind information to test the methods and quantify errors. Our work is motivated by GHGSat but is more generally applicable to any fine-scale plume observations from space.

## 1.2 REVIEW OF METHODS FOR RETRIEVING POINT SOURCES FROM OBSERVATIONS OF COLUMN PLUMES

A methane point source produces a turbulent plume of atmospheric methane with characteristics determined by the strength of the source, the wind field, and turbulence that depends on atmospheric stability and surface roughness. Four different methods have been proposed to quantify point source rates from plume observations: (1) the Gaussian plume inversion method (Bovensmann et al., 2010; Krings et al., 2011, 2013; Rayner et al., 2014; Fioletov et al., 2015; Nassar et al., 2017; Schwandner et al., 2017), (2) the source pixel method (Jacob et al., 2016; Buchwitz et al., 2017), (3) the CSF method (White et al., 1976; Conley et al., 2016; Krings et al., 2011, 2013; Tratt et al., 2011, 2014; Frankenberg et al., 2016), and (4) the IME method (Thompson et al., 2016; Frankenberg et al., 2016). Here we discuss these methods for remote sensing observations of column plumes. This is a somewhat different problem than for in situ observations of plumes. In situ observations benefit from a stronger signal but require characterization of the plume in the vertical dimension, which is integrated in a column measurement.

Satellite remote sensing of methane plumes retrieves column concentrations with vertical sensitivity that depends on atmospheric scattering and absorption. Clear-sky observations in the SWIR have near-unit sensitivity throughout the tropospheric column, while observations in the thermal infrared (TIR) have strong vertical dependence determined by temperature contrast with the surface (Worden et al., 2013). Here we focus on SWIR observations, where we can ignore vertical dependence in sensitivity. TIR remote sensing has been used effectively to detect methane plumes from low-flying aircraft (Tratt et al., 2014; Frankenberg et al., 2016) but is not practical from space because of interference from the background methane column above the plume (Jacob et al., 2016).

Methane column concentrations retrieved from remote sensing are commonly expressed in the literature as column-average dry molar mixing ratio  $X$  [ppb]. The plume is then characterized by

an enhancement  $\Delta X = X - X_b$  relative to the local background  $X_b$ . For our purposes of relating plume observations to the source rate  $Q$  [ $\text{kg s}^{-1}$ ], a more useful measure of plume concentration is the column mass enhancement  $\Delta\Omega$  with units [ $\text{kg m}^{-2}$ ].  $\Delta\Omega$  is related to  $\Delta X$  by

$$\Delta\Omega = \frac{M_{CH_4}}{M_a} \Omega_a \Delta X \quad (1.1)$$

where  $M_{CH_4}$  and  $M_a$  are the molar masses of methane and dry air [ $\text{kg mol}^{-1}$ ] and  $\Omega_a$  is the column of dry air [ $\text{kg m}^{-2}$ ].

### 1.2.1 GAUSSIAN PLUME INVERSION METHOD

The Gaussian plume inversion method fits a Gaussian plume model to the measured columns. Assuming a steady wind  $U$  oriented along the  $x$  axis and integrating the three-dimensional Gaussian plume equation vertically, one obtains an expression for  $Q$  in terms of the vertical column enhancement  $\Delta\Omega(x, y)$  downwind of a point source located at the origin (Bovensmann et al., 2010):

$$Q = U\Delta\Omega(x, y) \left( \sqrt{2\pi}\sigma_y e^{\frac{y^2}{2\sigma_y^2}} \right) \quad (1.2)$$

The empirical dispersion parameter  $\sigma_y(x)$  [m] describes the horizontal spread of the plume along the  $y$  axis orthogonal to the wind direction. It is commonly parameterized as (Martin, 1976)

$$\sigma_y(x) = \alpha \left( \frac{x}{x_0} \right)^{0.894} \quad (1.3)$$

where  $x_0 = 1000$  m, and the dispersion coefficient  $\alpha$  [m] depends on atmospheric stability as defined by the Pasquill-Gifford atmospheric stability categories (Pasquill, 1961). The solution to Equation 1.2 may involve non-linear optimal estimation fitting of  $\alpha$  to the observed plume (Krings et al., 2011). The fit may not be successful if the instantaneous plume shows large departure from

steady-state Gaussian behaviour.

### 1.2.2 SOURCE PIXEL METHOD

In the source pixel method used by Jacob et al. (2016) to compare different satellite-observing configurations, emissions are inferred solely from methane enhancements in the source pixel relative to the local background. For an observation pixel of dimension  $W$  [m] containing a methane point source ventilated by a uniform wind speed  $U$  [m s<sup>-1</sup>], the source rate  $Q$  [kg s<sup>-1</sup>] is calculated from the mean source pixel enhancement  $\Delta\Omega$  [kg m<sup>-2</sup>]:

$$Q = \frac{UWp}{g\Omega_a} \Delta\Omega \quad (1.4)$$

where  $p$  is the surface pressure and  $g$  is the acceleration of gravity. The source pixel method ignores additional information from the plume downwind and is therefore not optimal. In addition, the instantaneous wind  $U$  may have large uncertainty for small pixels because of turbulence. The method is also vulnerable to systematic errors in the column enhancement retrieved over the source pixel (e.g., due to different reflectance properties of the emitter compared to the surrounding area) and errors in the local background estimate.

### 1.2.3 CROSS-SECTIONAL FLUX (CSF) METHOD

In the CSF method, the source rate is estimated by computing the flux through one or more plume cross sections orthogonal to the plume axis. This approach is commonly used for aircraft in situ observations (White et al., 1976; Mays et al., 2009; Cambaliza et al., 2014, 2015; Conley et al., 2016). Krings et al. (2011, 2013) and Tratt et al. (2011, 2014) extended it to methane columns observed by aircraft remote sensing. By mass balance, the source rate  $Q$  must be equal to the product of the wind speed and the column plume transect along the  $y$  axis perpendicular to the wind:

$$Q = \int_{-\infty}^{\infty} U(x, y) \Delta\Omega(x, y) dy \quad (1.5)$$

where the integral is approximated in the observations as a discrete summation of the product

$U(x, y) \Delta\Omega(x, y)$  over the detectable width of the plume.

Compared to in situ aircraft measurements, an advantage of remote sensing is that the full vertical extent of the plume is covered by the measurement. A disadvantage is that the wind  $U(x, y)$  is not as well characterized: it must describe some vertical average over the plume extent and there is generally no information on its horizontal variability over the scale of the plume. This may require estimation of an effective wind speed  $U_{\text{eff}}$  applied to the cross-plume integral  $C$  [ $\text{kg m}^{-1}$ ] of the column along the  $y$  axis:

$$Q = CU_{\text{eff}}, \text{ with } C = \int_{-\infty}^{\infty} \Delta\Omega(x, y) dy \quad (1.6)$$

If  $U_{\text{eff}}$  is assumed uniform with distance  $x$  downwind of the source, then the integral  $C$  is independent of  $x$  and can be computed for different values of  $x$  to improve accuracy through averaging. We show in Section 1.6 how to estimate  $U_{\text{eff}}$  for use in Equation 1.6.

#### 1.2.4 INTEGRATED MASS ENHANCEMENT (IME) METHOD

The IME method relates the source rate to the total plume mass detected downwind of the source.

The IME of an observed column plume comprising  $N$  pixels of area  $A_j$  ( $j = 1 \dots N$ ) is

$$\text{IME} = \sum_{j=1}^N \Delta\Omega_j A_j \quad (1.7)$$

Frankenberg et al. (2016) defined an empirical linear relationship between IME and  $Q$  for their methane plumes detected from aircraft by using independent estimates of a few sources from the

CSF method. They then applied this linear relationship to all their observed plumes.

More fundamentally, the relationship between IME and  $Q$  is defined by the residence time  $\tau$  of methane in the detectable plume:  $Q = \text{IME}/\tau$ . One can express  $\tau$  dimensionally in terms of an effective wind speed  $U_{\text{eff}}$  [ $\text{m s}^{-1}$ ] and a plume size  $L$  [m]:

$$Q = \frac{1}{\tau} \text{IME} = \frac{U_{\text{eff}}}{L} \text{IME} = \frac{U_{\text{eff}}}{L} \sum_{j=1}^N \Delta \Omega_j A_j \quad (1.8)$$

$U_{\text{eff}}$  and  $L$  would have simple physical meanings of wind speed and plume length if dissipation of the plume occurred by uniform transport to a terminal distance downwind of the source. But the actual mechanism for plume dissipation is turbulent diffusion, which takes place in all directions.

$U_{\text{eff}}$  and  $L$  must therefore be viewed as operational parameters to be related to observations of wind speed  $U$  and plume extent. In Section 1.5 we derive these relationships from synthetic plumes generated by LES. The detectable plume size  $L$  depends on  $Q$  and  $U$ , introducing non-linearity in Equation 1.8.

### 1.3 SYNTHETIC GHGSAT OBSERVATIONS OF METHANE PLUMES

We generate synthetic GHGSat plumes with the Weather Research and Forecasting model in LES mode (WRF-LES; Moeng et al., 2007; Skamarock et al., 2008) to evaluate the ability of the methods described in Section 1.2 to retrieve methane point source rates from satellite observations. The WRF-LES simulations are conducted at  $50 \times 50 \text{ m}^2$  resolution and are sampled virtually with the GHGSat instrument by column integration and with consideration of instrument precision. In this section, we briefly describe the GHGSat instrument and the application of LES to produce synthetic plumes.

### 1.3.1 THE GHGSAT INSTRUMENT

GHGSat is a lightweight satellite instrument ( $\sim 15$  kg) designed by GHGSat, Inc. to detect atmospheric methane plumes from individual point sources. A demonstration instrument (GHGSat-D) was launched in June 2016 into sun-synchronous orbit (local solar viewing time of 09:30 on the descending node) to test the instrument performance and column retrieval algorithm. The launch of the first operational satellite is scheduled for early 2019. The long-term plan is for a constellation of sun-synchronous GHGSat microsatellites in low Earth orbit, providing frequent observations of different sources of interest.

GHGSat measures backscattered solar SWIR radiation at 1635–1670 nm (0.1 nm spectral resolution) over  $\sim 10 \times 10$  km $^2$  targeted domains (12  $\times$  12 km $^2$  for GHGSat-D) with  $\leq 50 \times 50$  m $^2$  pixels. The design precision for the methane column retrieval is 1–5%. This is coarser precision than that of other satellite instruments (e.g., 0.6% for TROPOMI, 0.7% for GOSAT), but for observations of point sources it is more than offset by the finer pixel resolution (Jacob et al., 2016).

### 1.3.2 LARGE EDDY SIMULATIONS (LES)

We apply WRF-LES to simulate turbulent plume transport at 50  $\times$  50 m $^2$  horizontal resolution and 30 m vertical resolution over a 6  $\times$  6 km $^2$  domain. We use a modified version of the WRF v3.8 default LES case with cloud-free conditions and no topography (WRF User’s Guide, 2018; Moeng et al., 2007). Simulations are performed with one-way nesting from an external simulation over a 7.5  $\times$  7.5 km $^2$  domain with 150  $\times$  150 m $^2$  resolution and periodic boundary conditions. A uniform sensible heat flux  $H = 100$  W m $^{-2}$  is applied at the surface to drive buoyant turbulence. Mechanical turbulence is generated by surface drag with an aerodynamic roughness height of 0.1 m. Forcing from a large-scale pressure gradient maintains momentum across the domain.

Each LES simulates 5 h of atmospheric transport. The first 3 h spin up realistic turbulence and

the final 2 h are used for analysis. We use a range of initial mixing depths and wind speed soundings to produce different simulations. The potential temperature soundings are uniform at 290 K from the surface to a mixing depth set at either 500, 800, or 1100 m altitude, with an inversion above that altitude and the model top set 700 m above the inversion. For each of these three mixing depths, we conduct simulations using five initially uniform southerly wind profiles with speeds of 2–8 m s<sup>−1</sup>. The resulting LES ensemble of 15 simulations is broadly representative of the range of meteorological conditions that could be sampled with a SWIR daytime instrument.

We use the WRF-LES passive tracer transport capability (Nottrott et al., 2014; Nunalee et al., 2014) to generate a plume from a single constant point source in the WRF-LES meteorological environment. From there we integrate the plume over vertical columns and add random noise to produce GHGSat pseudo-observations. We archive the tracer column field every 30 s as an independent realization of the instantaneous plume. From the 15 WRF-LES simulations we thus archive a collection of 3600 scenes, representing our statistical ensemble for different possible realizations of turbulence.

The WRF-LES point source in the archived ensemble has a normalized source rate, which we subsequently scale from the output to simulate source rates  $Q$  in the range 0.05–2.25 t CH<sub>4</sub> h<sup>−1</sup> (0.5–20 kt a<sup>−1</sup>). This range covers the top 25% of sources reporting to the US Greenhouse Gas Reporting Program (GHGRP) and contributing 75% of total GHGRP methane emissions (Jacob et al., 2016). A uniform background methane column of 0.01 kg m<sup>−2</sup> (roughly 1850 ppb) is added to the tracer column. Uncorrelated measurement noise is then added as a random increment of the background sampled from a normal distribution with zero mean bias and standard deviation  $\sigma = 1\text{--}5\%$ , corresponding to the range of expected instrument precision. The column enhancement  $\Delta\Omega$  is then inferred by subtracting the 0.01 kg m<sup>−2</sup> background, which is therefore assumed to be known.

Figure 1.1 shows examples of synthetic plume observations produced in this manner for a source

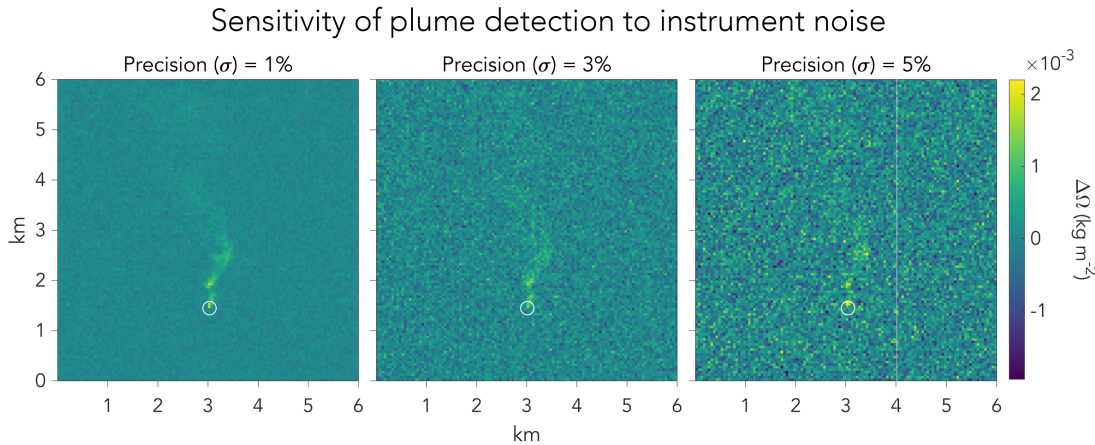


**Figure 1.1:** Examples of column plume pseudo-observations generated by an LES on a  $50 \times 50 \text{ m}^2$  grid. The circle identifies the location of the source. Each panel shows the same synthetic plume observation for a source  $Q = 1 \text{ t h}^{-1}$ , with instrument precision  $\sigma$  varying from 1% to 5%.

$Q = 1 \text{ t h}^{-1}$ , assuming different levels of instrument precision. As the precision decreases, the plume is increasingly difficult to detect.

#### 1.4 INADEQUACY OF THE GAUSSIAN PLUME AND SOURCE PIXEL METHODS

Previous studies of CO<sub>2</sub> column observations from the OCO-2 satellite instrument with  $\sim 1.3 \times 2.25 \text{ km}^2$  nadir pixel resolution (Crisp et al., 2017) have shown that the Gaussian plume inversion method can be effective for quantifying very large CO<sub>2</sub> emissions from power plants (Nassar et al., 2017) and volcanoes (Schwandner et al., 2017). We find here that the approach fails when applied to fine-scale methane plumes, because the plumes depart too much from Gaussian behaviour. CO<sub>2</sub> point sources can be considerably larger relative to background concentrations and instrument precision levels, and the resulting plumes can then be observed over distances of tens of kilometres. Such a large size allows for statistical averaging of eddies and hence better approximation of Gaussian behaviour, even for an instantaneous plume. To demonstrate this, Figure 1.2 shows an LES snapshot of a large power plant emitting  $3.75 \text{ kt CO}_2 \text{ h}^{-1}$  in a 72 km domain with  $300 \times 300 \text{ m}^2$

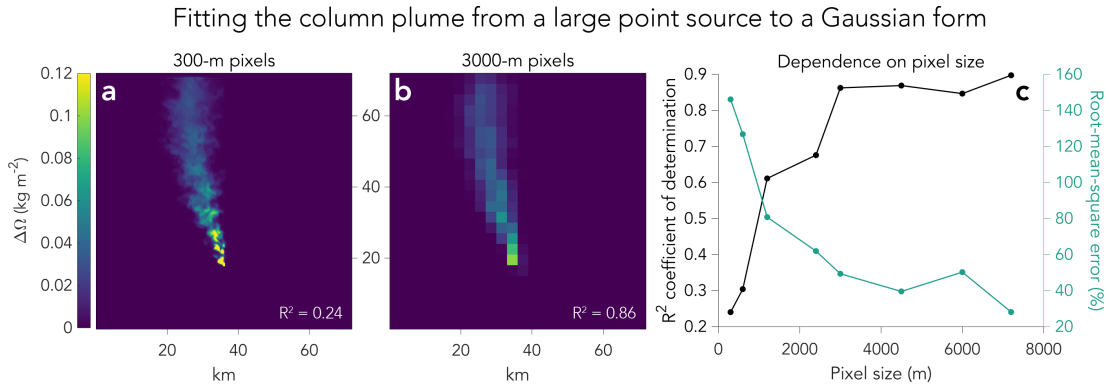


**Figure 1.2:** CO<sub>2</sub> column enhancements relative to background for a 3.75 kt CO<sub>2</sub> h<sup>-1</sup> (33 Mt CO<sub>2</sub> a<sup>-1</sup>) power plant plume simulated by LES at 300 m resolution. (a) shows the plume with 300 m pixel resolution and (b) shows the same plume but with pixel resolution degraded to 3000 m. The coefficient of determination ( $R^2$ ) inset measures the ability to fit each LES plume to a Gaussian form (Eqs. 1.2–1.3). (c) shows how the coefficient of determination and the root-mean-square error (expressed as a percentage of the median pixel enhancement) vary with pixel resolution.

pixel resolution. Fitting a Gaussian plume to the 300 m pixel enhancements yields a coefficient of determination  $R^2$  of only 0.24, but  $R^2$  increases to 0.86 when the LES image is averaged over  $3 \times 3$  km<sup>2</sup> pixels. Spatial averaging of turbulence over kilometre-scale pixels thus greatly improves the accuracy of Gaussian plume models, but this requires sufficiently large plumes. Methane plumes are generally too small to allow such averaging (Frankenberg et al., 2016).

The source pixel retrieval method only considers the column enhancement over the point source pixel, thus inferring the source rate from ventilation of that pixel by the local wind. It assumes in effect that the near-field plume is diluted over the source pixel and neglects information from the plume downwind. This can be an effective method when pixel resolution is coarse, so that most of the information is in the source pixel and the mean wind across the pixel can be well defined (Buchwitz et al., 2017). However, it has three major shortcomings when applied to GHGSat 50 × 50 m<sup>2</sup> pixels: (1) it does not exploit the information from downwind pixels, where most of the plume mass typically resides; (2) small-scale turbulence generates strong variability in the wind; and (3) source pixel ventilation may take place by turbulent horizontal diffusion rather than advection by the mean

wind, leading to negative bias. With regard to (2), the residence time in a GHGSat pixel is only  $\sim 30$  s, and there is large variability in the wind on such a short timescale that cannot be described deterministically. For example, in a typical LES under moderately unstable conditions we find a 10-m wind speed of  $2.45 \pm 0.8 \text{ m s}^{-1}$ , where the standard deviation is for the 30 s data. This 30 s variability in wind speed alone thus introduces a factor of 30% uncertainty in the source estimate. With regard to (3), the relative importance of turbulent diffusion and advection is diagnosed by the Péclet number  $Pe = UL/K_H$ , where  $K_H$  is the turbulent horizontal diffusion coefficient (Brasseur and Jacob, 2017). For a typical  $K_H = 50 \text{ m}^2 \text{ s}^{-1}$  (d'Isidoro et al., 2010) with  $U = 2 \text{ m s}^{-1}$  and  $L = 50$  m we find  $Pe \sim 1$ , so that turbulent diffusion and advection are of comparable importance.

## 1.5 COMPUTING THE SOURCE RATE BY THE IME METHOD

We showed in Section 1.2.4 how the IME method for retrieving the point source rate  $Q$  from the measured IME hinges on knowledge of the residence time of methane in the detectable plume. We refer to this residence time as the plume lifetime  $\tau = \text{IME}/Q$ , which in turn is related to two parameters: an effective wind speed  $U_{\text{eff}}$  and a characteristic plume size  $L$ . IME and  $L$  can be inferred from the plume observations, while  $U_{\text{eff}}$  can be inferred from the observable 10-m wind speed  $U_{10}$  at the point of emission.

### 1.5.1 INFERRING THE PLUME MASS (IME) AND SIZE ( $L$ )

Inferring IME and  $L$  from the plume observations requires that we define the horizontal extent of the plume through a pixel selection procedure that separates signal from noise. Careful selection is important. Consider an array of  $N$  pixels of equal area and with retrieved column enhancements  $\Delta\Omega_j$  ( $j = 1\dots N$ ). If each pixel enhancement includes a contribution  $s_j$  from signal (actual plume enhancement) and  $\varepsilon_j$  from random noise, then as per Equation 1.7,

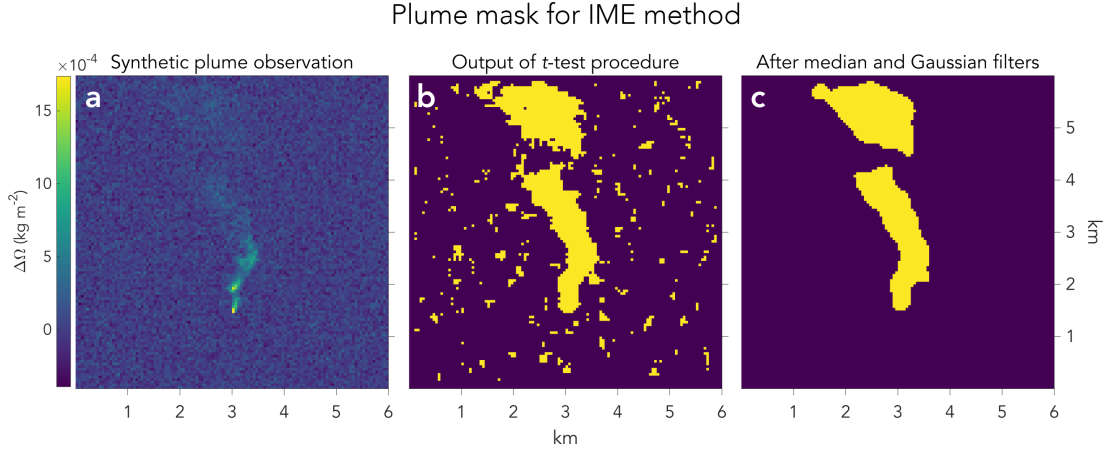


**Figure 1.3:** Illustration of the procedure for constructing plume masks in the IME method. (a) Satellite pseudo-observation generated by LES for a point source  $Q = 1 \text{ t h}^{-1}$ , with instrument precision  $\sigma = 1\%$  (same as in figure 1.1). (b) The output of the  $t$ -test procedure for significant signal. (c) The final plume mask after application of median and Gaussian filters.

$$\frac{\text{IME}}{A} = \sum_{j=1}^N \Delta\Omega_j = \sum_{j=1}^N (s_j + \varepsilon_j) = \varepsilon_a + \sum_{j=1}^N s_j, \quad (1.9)$$

where  $\varepsilon_a$  is the total (absolute) measurement error. The relative error  $\varepsilon_r$  is then  $\varepsilon_r = \varepsilon_a / \sum_j^N s_j$ . If the noise is normally distributed and uncorrelated, then the error standard deviation is proportional to  $\sqrt{N}$ , so that the standard deviation  $\sigma_r$  of the relative error scales as

$$\sigma_r \propto \frac{\sqrt{N}}{\sum_j^N s_j}. \quad (1.10)$$

Now consider two extreme cases: (1) all pixels contain the same signal  $s_0$ , and (2) only one pixel contains signal  $s_0$  and the other pixels contain only noise. In case (1), the total signal  $\sum_j^N s_j$  is proportional to  $N$ , meaning  $\sigma_r \propto 1/\sqrt{N}$ . By contrast, in case (2), the total signal is equal to  $s_0$ , so  $\sigma_r \propto \sqrt{N}$ . Thus, we see that aggregating plume pixels can either decrease or increase the error on the IME depending on whether these pixels have significant signal or not.

Figure 1.3 illustrates how we construct a plume mask to select plume pixels with significant signal-to-noise ratios. The background distribution (mean  $\pm$  standard deviation) is first characterized by an upwind sample of the measured columns, mimicking what one would do with actual observations. Next, we sample the  $5 \times 5$  pixels neighbourhood centred on each pixel in the viewing domain and compare the sample distributions to the background distribution by means of a Student's  $t$  test. Pixels with  $5 \times 5$  neighbourhoods that follow a distribution significantly different than the background at a confidence level of 95% or higher are assigned to the plume and others to the background. The resulting Boolean plume mask contains some random classification errors, so we smooth it with a median filter followed by a Gaussian filter and thresholding. The median filter replaces each pixel in the mask by the median value of its  $3 \times 3$  neighbourhood. The Gaussian filter convolves the mask with a two-dimensional Gaussian of standard deviation 2–5 pixels, with larger values for higher noise levels.

We compute the IME by summing pixel enhancements within the plume mask following Equation 1.7. A simple measure of the plume size  $L$  can be taken as

$$L = \sqrt{A_M} \quad (1.11)$$

where  $A_M$  [ $\text{m}^2$ ] is the area of the plume mask. Another possible estimate of  $L$  would be the mask's perimeter, which can be obtained by contour tracing. The definition of  $L$  is not critical as long as it has some physical basis relating it to the observed plume geometry. A different definition would imply a different calculation of  $U_{\text{eff}}$ .

### 1.5.2 INFERRING $U_{\text{eff}}$ FROM THE 10-M WIND SPEED $U_{10}$

The effective wind speed  $U_{\text{eff}}$  is a parameter of the IME method that should be related to the measurable 10-m wind speed at the location of the point source, and here we use the LES to derive the

$U_{\text{eff}} = f(U_{10})$  relationship. If  $U_{10}$  is not actually measured at the site, it can be estimated from an operational meteorological database at the cost of some representation error. We discuss that error in Section 1.7.

We derive the  $U_{\text{eff}} = f(U_{10})$  relationship from a training set of column plumes comprising two-thirds of the LES ensemble selected at random (i.e., 2400 plume instances). The remaining plumes serve as a test set for evaluating the retrieval algorithm. For each plume in the training set,  $U_{\text{eff}}$  is computed from Equation 1.8 as  $U_{\text{eff}} = QL/\text{IME}$ , based on the known source rate  $Q$  and with  $L$  and IME determined from the plume masks. The corresponding  $U_{10}$  time series at the location of the source is obtained from the LES, averaged over the plume lifetime  $\tau = \text{IME}/Q$ . Values of  $\tau$  in our ensemble range from 1 to 60 min depending on instrument precision, source rate, and wind speed. In practice,  $\tau$  is unknown a priori and must be inferred from the plume observations and local wind speed information. We discuss this in Section 1.5.3.

Figure 1.4 shows the relationship between  $U_{\text{eff}}$  and  $U_{10}$  inferred from the LES ensemble. We find that we can fit the data to a logarithmic dependence:

$$U_{\text{eff}} = \alpha_1 \log U_{10} + \alpha_2, \quad (1.12)$$

where  $\alpha_1 = 0.9\text{--}1.1$ ,  $\alpha_2 = 0.6 \text{ m s}^{-1}$ , and the range on the first coefficient is for the 1–5% range of instrument precision. For 1% instrument precision, the logarithmic function plotted in Figure 1.4 captures 75% of the variance ( $R^2 = 0.75$ ). This decreases to 35% of the variance for 5% instrument precision. The convexity of the relationship is an important result, as it implies that error in  $U_{\text{eff}}$  is smaller than error in  $U_{10}$ . One might expect  $U_{\text{eff}}$  from the IME method to be proportional to  $U_{10}$ , such that  $\text{IME}L$  would be inversely proportional to  $U_{10}$  as per Equation 1.8. However, even though that inverse relationship holds for plume concentrations (see Equation 1.6), it is much weaker for the IME because the concentrated plume in the near-field of the source remains in the signal even

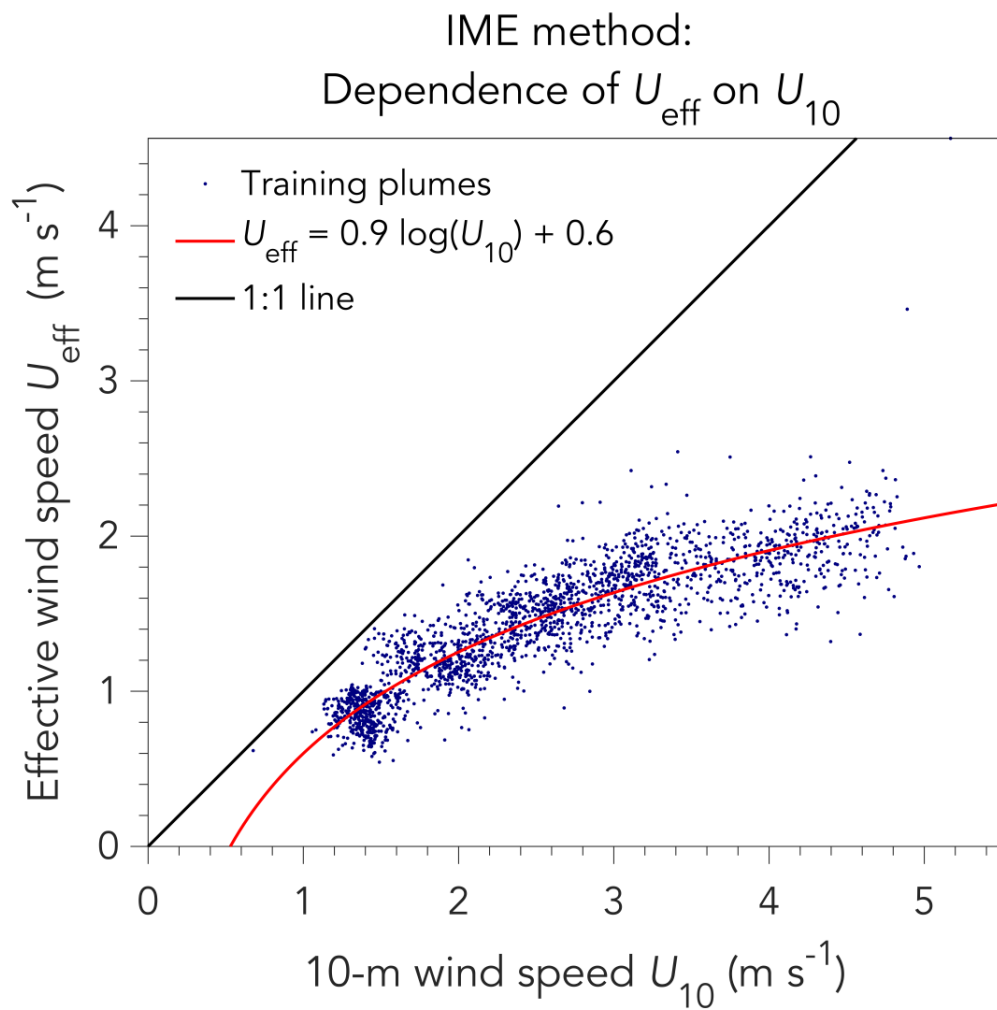


**Figure 1.4:** Relationship between the effective and local 10-m wind speeds in the IME method, characterized with LES training plumes assuming 1% instrument precision. Each point represents a different LES plume pseudo-observation from the training set. The red line fits the data to a logarithmic dependence. The 1:1 line is shown in black. See text for similar results with 3% or 5% instrument precision.

at high wind speeds. Thus, the plume observations themselves interpreted with the IME method contain some information on  $U_{10}$  that slackens the dependence of  $U_{\text{eff}}$  on  $U_{10}$ .

### 1.5.3 COMPUTING THE SOURCE RATE

Figure 1.5 summarizes the algorithm for retrieving source rates with the IME method. The algorithm accepts two inputs: (1) a map of plume enhancements  $\Delta\Omega(x, y)$  over the plume mask, and (2) the 10-m wind speed  $U_{10}$  from either local high-frequency measurements or an operational meteorological database. If local high-frequency measurements of  $U_{10}$  are available, then there is an opportunity to iteratively refine the plume lifetime  $\tau$  over which  $U_{10}$  should be averaged, and for this we make a first guess  $\tau_0 = 5$  min. If only coarse-resolution wind speed data are available, then we assume that these are representative of the local value averaged over the plume lifetime and add the associated error to the overall error budget (see Section 1.7).

Figure 1.6 shows the instantaneous source rates retrieved from our IME algorithm when applied to the test set of LES plumes in different instrument precision scenarios, compared to the true source rates. There is good agreement with the 1:1 line in all cases ( $R^2 \geq 0.86$ ). Retrieval uncertainty (expressed as absolute and relative contributions and defined by the standard deviation of departure from the 1:1 line) increases from  $0.07 \text{ t h}^{-1} + 5\%$  for  $\sigma = 1\%$ , to  $0.13 \text{ t h}^{-1} + 7\%$  for  $\sigma = 3\%$ , and  $0.17 \text{ t h}^{-1} + 12\%$  for  $\sigma = 5\%$  (Table 1.1). For sources  $1.5 \text{ t h}^{-1}$  or larger, retrieval error is less than 25% even with instrument precision up to 5%. For  $Q = 1 \text{ t h}^{-1}$ , instrument precision up to  $\sigma = 3\%$  yields uncertainty less than 20% of the true source rate. Source rates larger than  $0.3 \text{ t h}^{-1}$  contribute more than 75% of total methane emitted from point sources reporting to the US Greenhouse Gas Reporting Program (Jacob et al., 2016). An instrument with  $\sigma = 1\%$  measurement uncertainty can quantify these emissions to within 30% of the true source rate.

# Source rate retrieval by the IME method

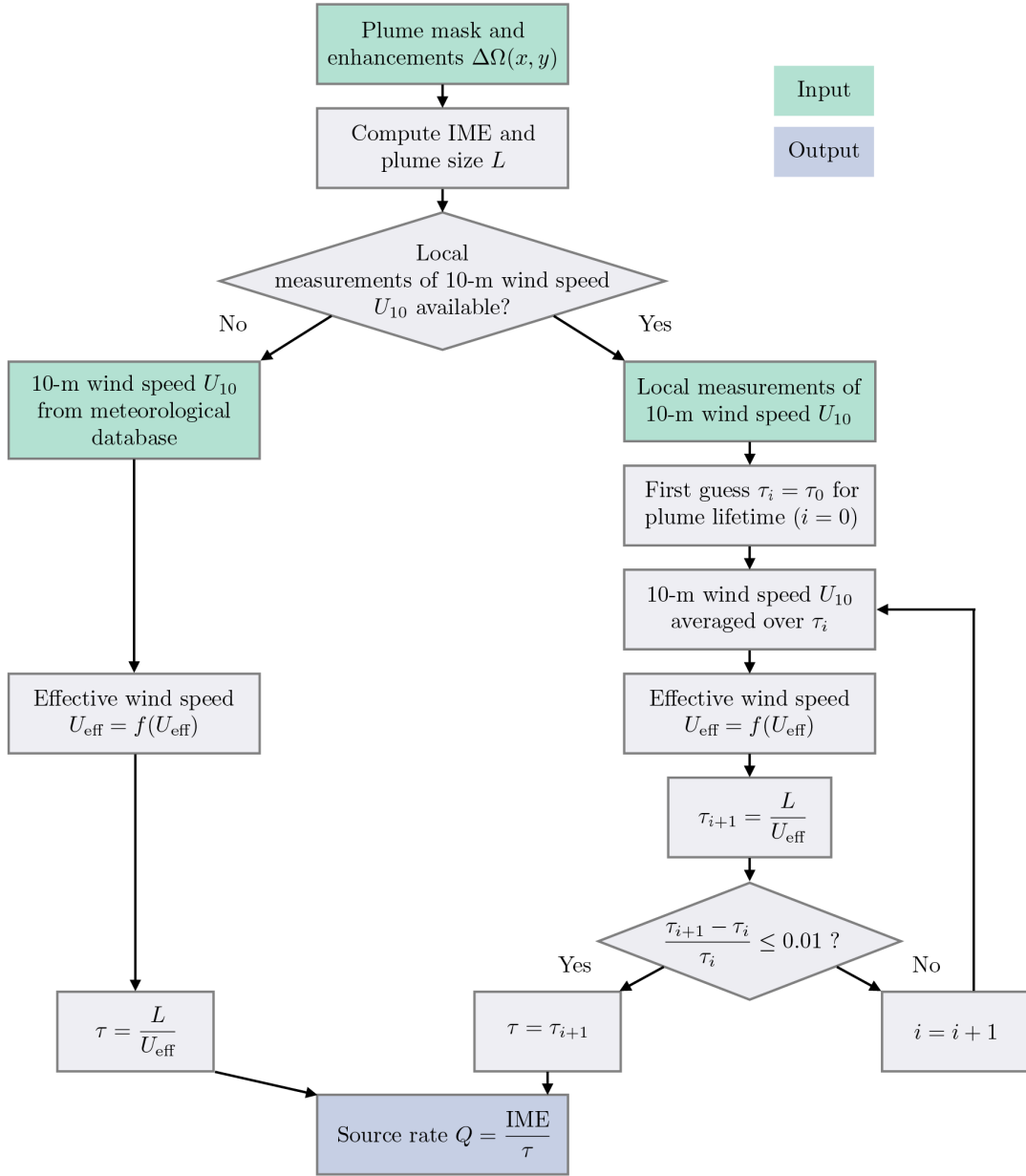


**Figure 1.5:** Flow chart describing the IME retrieval algorithm. Algorithm inputs are shown in green, operations in grey, and output in blue. There are two possible paths depending on the availability of 10-m wind speed data: (a) local high-frequency wind speed measurements at the location of the source (right branch), and (b) a temporally averaged meteorological database (left branch).

## Testing the IME method

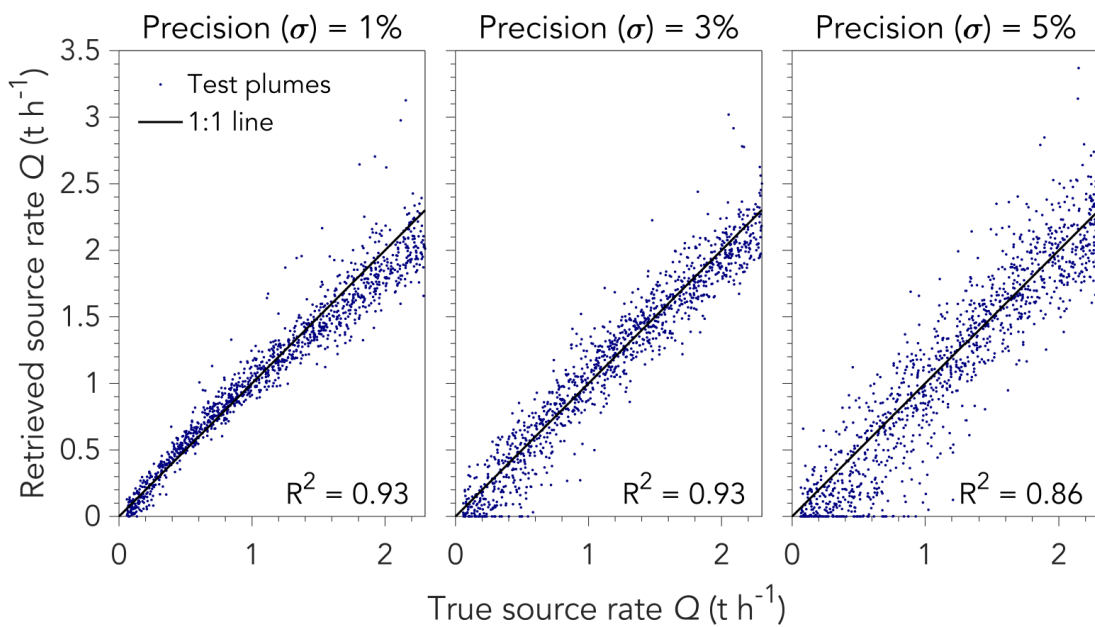


**Figure 1.6:** Evaluation of the IME method for retrieving source rates  $Q$  using the LES test set with three different instrument precisions (1%, 3%, 5%). The inset gives the coefficient of determination,  $R^2$ .

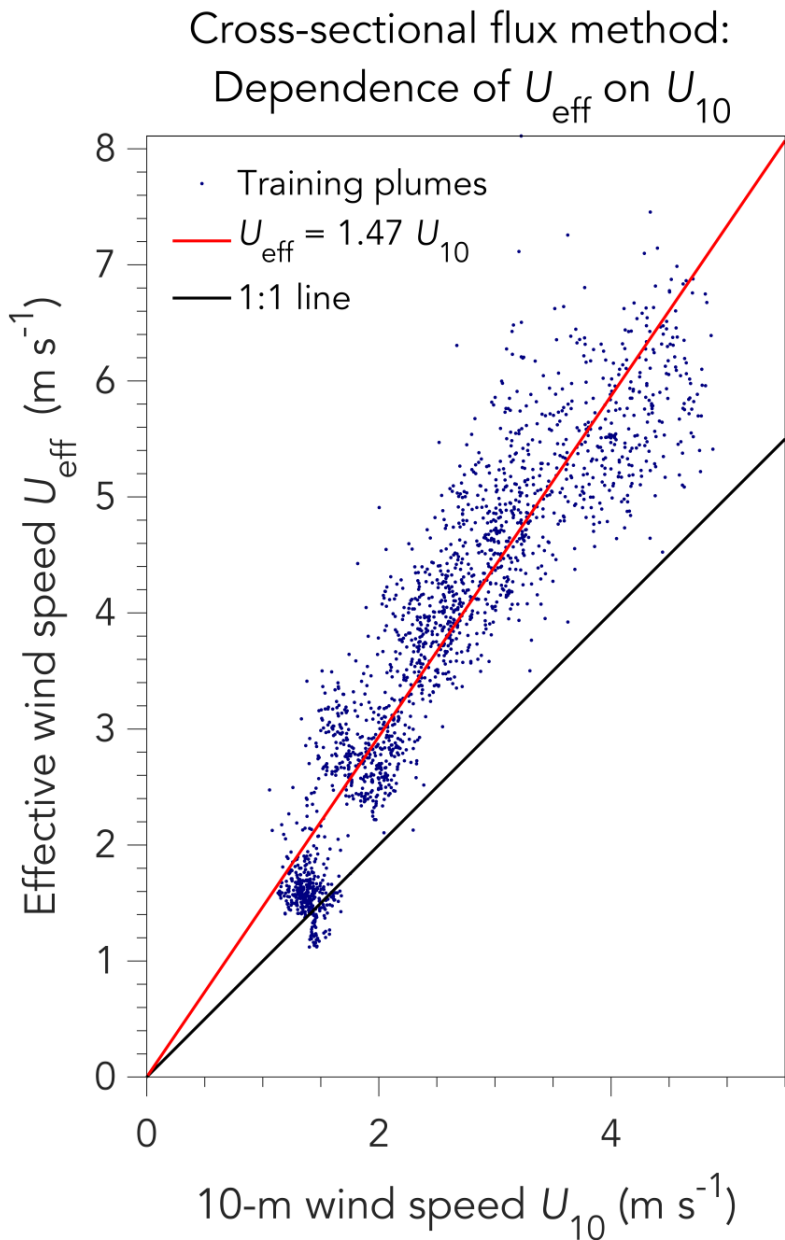
## 1.6 COMPUTING THE SOURCE RATE BY THE CSF METHOD

Much of our analysis of the IME method in Section 1.5 can be applied to the CSF method commonly used for in situ aircraft observations and extended by Krings et al. (2011, 2013) and Tratt et al. (2011, 2014) for remote sensing observations. We compute the plume mask as described in Section 1.5.1, and infer the wind direction from the axis of the plume, based on a weighted average of plume pixel coordinates using the column enhancements as weights. From there, we obtain the mean cross-plume integral  $C$  of the column enhancements at different distances downwind of the source (see Equation 1.6).

We again use the LES training set to characterize the relationship between the effective wind speed  $U_{\text{eff}}$  in Equation 1.6 and the local 10-m wind speed  $U_{10}$ .  $U_{\text{eff}}$  in the CSF method is different than  $U_{\text{eff}}$  in the IME method. For each plume in the training set,  $U_{\text{eff}}$  is computed from Equation 1.6 based on  $C$  and the known source rate  $Q$ . The plume lifetime over which to average local high-frequency  $U_{10}$  measurements for comparison with  $U_{\text{eff}}$  is computed as  $\tau = L/U_{\text{eff}}$ , where the plume size parameter  $L$  now has a specific physical meaning as the maximum along-wind distance from the source over which transects can be computed (as defined by the plume mask).

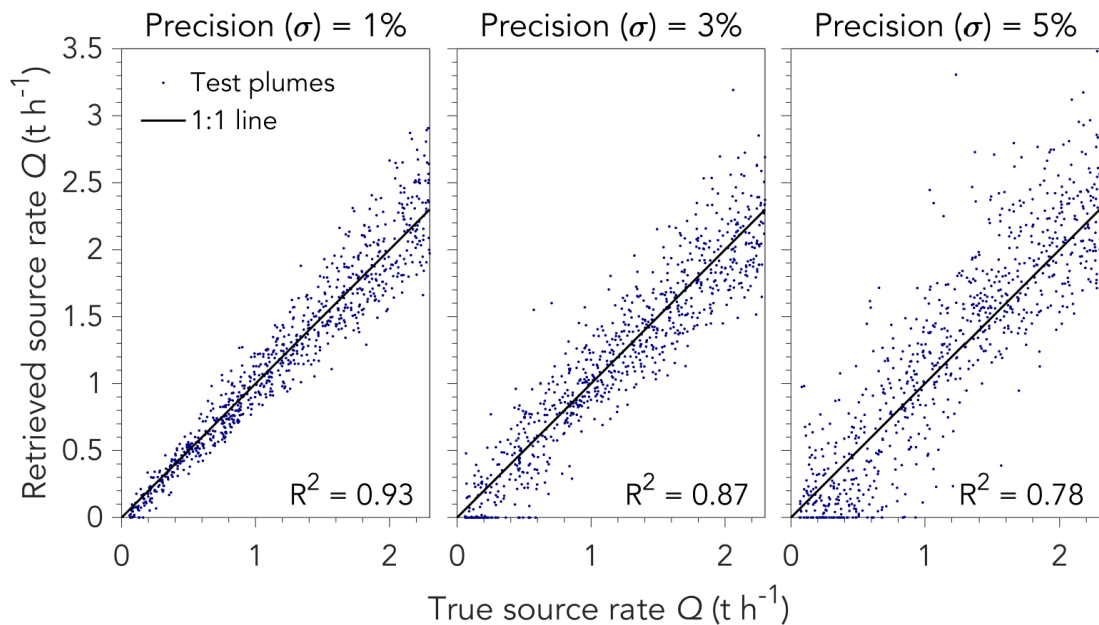
Figure 1.7 shows the resulting relationship between  $U_{\text{eff}}$  and  $U_{10}$ . The relationship is near-linear, as would be expected, and the fit  $U_{\text{eff}} = \beta U_{10}$  with  $\beta = 1.3\text{--}1.5$  (where the range is for the 1–5% range of instrument precisions) captures 25%–75% of the variance ( $0.25 \leq R^2 \leq 0.75$ ) for  $U_{10} \geq 2 \text{ m s}^{-1}$ , depending on instrument precision. The 30%–50% increase relative to  $U_{10}$  reflects the increase in wind speed with the altitude at which the plume is transported. The departure from the linear relationship for  $U_{10} < 2 \text{ m s}^{-1}$  is because low winds are more variable in direction. The CSF method should not be used under calm-wind conditions.

Figure 1.8 shows the results of the CSF retrieval algorithm applied to the LES test plumes, excluding those from the plume population with  $U_{10} < 2 \text{ m s}^{-1}$  and  $U_{\text{eff}} < 2 \text{ m s}^{-1}$ . In all in-



**Figure 1.7:** Relationship between the effective and local 10-m wind speeds in the CSF method, characterized with LES training plumes assuming 1% instrument precision. Each point represents a different LES plume pseudo-observation from the training set. The red line fits the data to a linear function, excluding the lowest wind speed population ( $U_{10} < 2 \text{ m s}^{-1}$  and  $U_{\text{eff}} < 2 \text{ m s}^{-1}$ ). See text for corresponding results with 3% and 5% instrument precision.  $U_{\text{eff}}$  for the CSF method is different than for the IME method (Figure 1.4).

## Testing the cross-sectional flux method



**Figure 1.8:** Evaluation of the CSF method for retrieving source rates  $Q$  using the LES test set with three different instrument precisions (1%, 3%, 5%). The inset gives the coefficient of determination,  $R^2$ .

**Table 1.1:** Error standard deviations for retrieving point source rates from column plume observations.

Method	Instrument precision <sup>a</sup>			Wind speed estimation error <sup>b</sup>
	1%	3%	5%	
IME	$0.07 \text{ t h}^{-1} + 5\%$	$0.13 \text{ t h}^{-1} + 7\%$	$0.17 \text{ t h}^{-1} + 12\%$	15–50%
CSF	$0.07 \text{ t h}^{-1} + 8\%$	$0.18 \text{ t h}^{-1} + 8\%$	$0.26 \text{ t h}^{-1} + 12\%$	30–65%

<sup>a</sup> Sum of absolute and relative errors when local measurements of 10-m wind speed  $U_{10}$  are available (see text). <sup>b</sup> Additional relative error when local wind speed data are not available. The values given here are inferred from a sample of the GEOS-FP global database over the US and should only be viewed as illustrative. The range is for GEOS-FP wind speeds of 2–7  $\text{m s}^{-1}$ , with the larger errors for the smaller wind speeds.

strument precision scenarios, the retrieved source rates are consistent with the 1:1 line. However, residuals are slightly larger than in the IME method (see Figure 1.6), as indicated by the smaller coefficients of determination. This results primarily from greater uncertainty in the effective wind speed compared to the IME method. Moreover, analyzing orthogonal plume cross sections requires estimation of the wind direction, which introduces an additional source of error. Absolute and relative retrieval errors estimated in the same way as for the IME method are listed in Table 1.1. While retrieval uncertainty is slightly higher ( $0.07\text{--}0.26 \text{ t h}^{-1} + 8\text{--}12\%$ , depending on instrument precision), an advantage of the CSF method is that there is a simpler physical basis for relating  $U_{10}$ ,  $C$ , and  $Q$ .

### 1.7 INFERRING THE EFFECTIVE WIND SPEED FROM METEOROLOGICAL DATABASES

Both the IME and CSF methods require knowledge of the local wind speed. In the absence of local wind speed measurements, the 10-m wind speed  $U_{10}$  at the time of observation must be estimated from some meteorological database. Here we examine the option of using the GEOS-FP operational reanalysis produced by the NASA Global Modelling and Assimilation Office, available globally as 3 h averages with  $0.25^\circ \times 0.3125^\circ$  resolution ( $\approx 25 \times 25 \text{ km}^2$ ) at a lowest grid point level of 60 m

above the surface (Molod et al., 2012; [https://gmao.gsfc.nasa.gov/GMAO\\_products/](https://gmao.gsfc.nasa.gov/GMAO_products/), last access: 24 October 2017). The 10-m wind speed can be obtained from the 60 m wind speed by

$$U_{10} = \left[ \frac{\ln \left( \frac{z_{10}}{z_{0,m}} - \Psi_m \right)}{\ln \left( \frac{z_{60}}{z_{0,m}} - \Psi_m \right)} \right] U_{60} \quad (1.13)$$

where  $z_{0,m}$  [m] is the surface roughness length for momentum,  $z_{10} = 10$  m,  $z_{60} = 60$  m, and  $\Psi_m = f(z/l)$  is a stability correction parameter dependent on the Monin–Obukhov length  $l$  (Brasseur and Jacob, 2017). The GEOS-FP data include values for  $z_{0,m}$  and  $l$ , but one can use local estimates of these variables if better information is available. Better databases than GEOS-FP may be available to the user depending on region, but an advantage of GEOS-FP is that it can be used as a global default.

Figure 1.9 evaluates the GEOS-FP  $U_{10}$  data by comparison to 3 h average daytime measurements in June 2017 at 10 US airports obtained from the University of Utah MesoWest database (Horel et al., 2002; MesoWest database, 2018). Here we use  $z_{0,m} = 0.025$  m as input to Equation 1.13 to account for the relatively smooth airport terrain. There is no bias in the GEOS-FP data relative to MesoWest. The error standard deviation derived from the difference between the 3 h GEOS-FP and MesoWest 10-m wind speeds is  $1.6 \text{ m s}^{-1}$ , largely independent of wind speed. Since wind speed is a positive variable, errors at low wind speeds ( $< 2 \text{ m s}^{-1}$ ) tend to be systematic. There is additional error from using 3 h wind data when the plume lifetime  $\tau$  is much shorter. From the 5 min resolution of the MesoWest data we find an additional error standard deviation of  $2.0 \text{ m s}^{-1}$  for  $\tau = 5 \text{ min}$  and  $1.3 \text{ m s}^{-1}$  for  $\tau = 1 \text{ h}$  when 3 h average wind speed data are used. Adding these errors in quadrature, we conclude that using GEOS-FP wind data incurs an error standard deviation on the 10-m wind speed of  $2.5 \text{ m s}^{-1}$  for small plumes ( $\tau = 5 \text{ min}$ ) and  $2.0 \text{ m s}^{-1}$  for large plumes ( $\tau = 1 \text{ h}$ ).

Substitution into the  $U_{\text{eff}} = f(U_{10})$  relations of the IME and CSF methods implies an additional

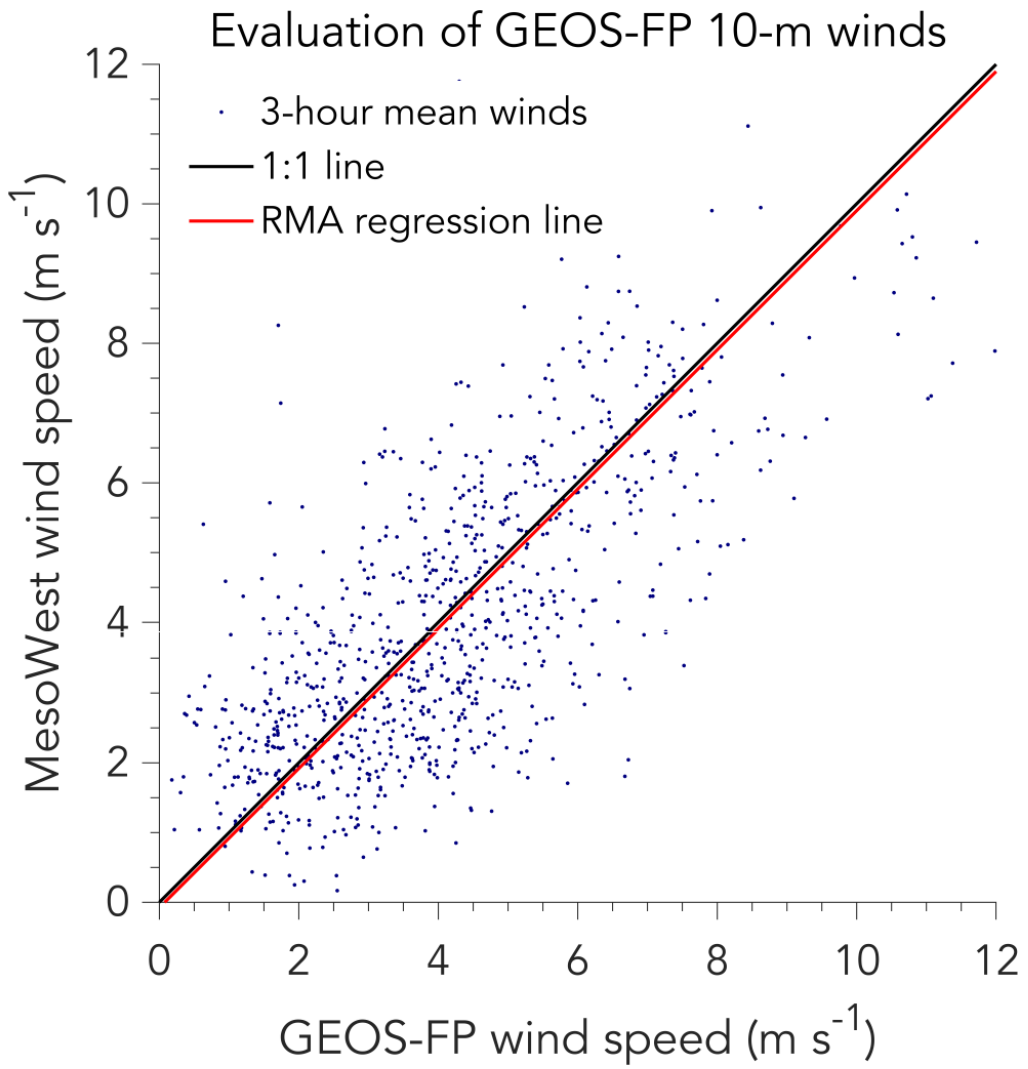


**Figure 1.9:** Evaluation of 10-m wind speeds from the 3 h GEOS-FP global database when used as estimate of local wind speed for source rate calculations in the IME and CSF methods. The figure compares 3 h average 10-m wind speeds from the MesoWest database measured at 10 US airports (ABQ, ATL, BOS, DFW, LAX, MCI, MSP, PDX, PHL, and PHX) to corresponding values from the GEOS-FP database. The GEOS-FP data have been corrected for a local roughness height  $z_{0,m} = 0.025 \text{ m}$  (see text). The data are for daytime June 2017 (15:00–21:00 UTC). The fit to a reduced major axis (RMA) regression line is also shown, which closely overlaps the 1:1 line.

error in inferring  $Q$  of 15–50% for the IME method and 30–65% for the CSF method over the 10-m wind speed range  $2\text{--}7 \text{ m s}^{-1}$ , with largest errors at low wind speeds. The error is larger for the CSF method where the dependence of  $U_{\text{eff}}$  on  $U_{10}$  is linear rather than logarithmic. Comparison to the other retrieval errors for each method is given in Table 1.1. At low wind speeds, the error from using GEOS-FP wind data may dominate the overall error budget for inferring source rates. However, our estimate of the error from using operational meteorological databases is intended only to be illustrative. Different errors may apply for other regions or seasons, or when using other meteorological databases than GEOS-FP.

## 1.8 CONCLUSIONS

We have developed new algorithms for quantifying methane point sources from fine-scale satellite observations of atmospheric column plumes, motivated by the planned fleet of GHGSat instruments ( $\leq 50 \times 50 \text{ m}^2$  pixel resolution, 1–5% precision). A challenge is that individual point sources of methane are relatively weak, so that the detectable instantaneous plumes are relatively small ( $\sim 1 \text{ km}$ ) and short lived ( $\leq 1 \text{ h}$ ). Using a large ensemble of WRF large eddy simulations (LES) of methane plumes from point sources, we showed that Gaussian plume inversions are unsuccessful because the instantaneous plumes are too small to follow Gaussian behaviour. We also showed how a simple source pixel mass balance method is inappropriate because of wind variability and horizontal turbulent diffusion on the scales of relevance.

Two more promising methods for quantifying source rates from methane column plume observations are the integrated mass enhancement (IME) method and the cross-sectional flux (CSF) method. Both methods require construction of a plume mask to isolate the plume enhancements from the background noise. The IME method requires estimation of the plume lifetime  $\tau$ , which in turn depends on an effective wind speed  $U_{\text{eff}}$  for the plume and a characteristic plume size  $L$ . We

showed how these quantities can be estimated from knowledge of the plume mask and of the 10-m wind speed  $U_{10}$  at the location of the source. The source rates are then inferred from the plume observations with expected errors of  $0.07\text{--}0.17 \text{ t h}^{-1} + 5\text{--}12\%$  depending on instrument precision (1–5%). For reference, source rates larger than  $0.3 \text{ t h}^{-1}$  contribute more than 75% of total point source emissions in the US Greenhouse Gas Reporting Program (GHGRP) database.

The CSF method requires an estimate of the wind direction and of an effective wind speed  $U_{\text{eff}}$  reflecting the vertical and horizontal spread of the plume. Again, the LES simulations show how these can be reliably estimated from the plume mask and local  $U_{10}$ . We find that for  $U_{10} \geq 2 \text{ m s}^{-1}$ ,  $U_{\text{eff}} = \beta U_{10}$  with  $\beta = 1.3\text{--}1.5$  is a good approximation that accounts for vertical plume spreading. The CSF method should not be used for  $U_{10} < 2 \text{ m s}^{-1}$ . The errors on the source rates are  $0.07\text{--}0.26 \text{ t h}^{-1} + 8\text{--}12\%$ , slightly worse than in the IME method. An advantage of the CSF method is its simpler physical basis.

Both the IME and the CSF methods parameterize their effective wind speeds  $U_{\text{eff}}$  as a function of the local wind speed  $U_{10}$ . If local measurements of  $U_{10}$  are not available, then  $U_{10}$  must be estimated from an operational meteorological database or from measurements some distance away. Using the global NASA GEOS-FP archive of wind speeds in June 2017 as an illustrative example compared to US airport data, we find that using this archive would incur source rate errors of 15–50% in the IME method and 30–65% in the CSF method over the  $2\text{--}7 \text{ m s}^{-1}$  range of wind speeds. The largest errors are at low wind speeds where they dominate the overall error budget. Low wind speeds facilitate source detection by improving signal to noise, but worsen source quantification by increasing the uncertainty in the inference of  $U_{\text{eff}}$ .

Our source rate retrieval algorithms were motivated by the need to interpret GHGSat plume observations but can readily be applied to any fine-pixel remote sensing measurements of methane column plumes from satellite or aircraft. The precision in retrieving point source rates is much better than can be achieved by current or planned imaging satellites from governmental space agencies,

which have higher instrument precision but coarser pixel resolution (Jacob et al., 2016).

Several questions remain to be explored. (1) How will correlated errors in the retrieved methane columns, as observed in GHGSat-D columns (Germain et al., 2017; McKeever et al., 2017), affect source quantification by the IME and CSF methods? Such errors would complicate plume definition and plume enhancement calculations. More advanced image segmentation techniques based on machine learning experiments may be useful to differentiate plumes from correlated background errors. (2) How reliably can we parameterize the relationship between effective and 10-m wind speeds given the range of topographies, source elevations, and meteorological environments observed in the real world? Targeted LES experiments may be needed to better constrain the  $U_{\text{eff}} = f(U_{10})$  relationship for sources in complex topography. (3) How will scattering uncertainties in the photon light paths influence mass enhancement estimates? Clouds in the scene can introduce scattering errors while also masking out portions of the plume. The masked pixels could be estimated by interpolation but scattering errors may be too severe.

#### ACKNOWLEDGEMENTS

Daniel J. Jacob's contribution was supported by the NASA Earth Science Division. Yan Xia and Yi Huang acknowledge grants from the Natural Sciences and Engineering Council of Canada (RGPIN 418305-13 and EGP 492771-15). We thank reviewers Ray Nassar (Environment and Climate Change Canada) and Peter Rayner (University of Melbourne) for their insightful comments, and Richard Lachance (Bluefield, Inc.) for pointing out an error in the original manuscript.

2

# Satellite Discovery of Anomalously Large Methane Point Sources from Oil/Gas Production

RAPID IDENTIFICATION OF ANOMALOUS METHANE SOURCES in oil/gas fields could enable corrective action to fight climate change. The GHGSat-D satellite instrument measuring atmospheric methane with 50-meter spatial resolution was launched in 2016 to demonstrate space-based monitoring of methane point sources. Here we report the GHGSat-D discovery of an anomalously large, persistent methane source (10–43 metric tons per hour, detected in over 50% of observations) at a gas compressor station in Central Asia, together with additional sources (4–32 metric tons per hour) nearby. The TROPOMI satellite instrument confirms the magnitude of these large emissions going back to at least November 2017. We estimate that these sources released  $142 \pm 34$  metric kilotonnes of methane to the atmosphere from February 2018 through January 2019, comparable to the 4-month total emission from the well-documented Aliso Canyon blowout.

## 2.1 INTRODUCTION

Anthropogenic methane emissions originate from a large number of point sources, including coal mines, landfills, wastewater plants, livestock operations, and oil/gas facilities (Kirschke et al., 2013;

Saunois et al., 2016). Methane generates 84 times more greenhouse gas warming per unit mass than carbon dioxide on a 20-year time horizon (International Panel on Climate Change, 2013). Over that time horizon, the radiative forcing of methane emitted from oil/gas operations is comparable to the radiative forcing of carbon dioxide emitted from natural gas usage (Alvarez et al., 2018). Much of the methane emitted from the oil/gas industry can be reduced or eliminated at no net cost, suggesting that reducing methane emissions from oil/gas operations is one of the most actionable steps to abate climate change (International Energy Agency, 2017).

There has been considerable interest in using satellite observations of atmospheric methane to detect and quantify methane sources, but observations available so far have only been able to resolve regional scales ( $\sim 50$  km), over which hundreds of individual point sources may be aggregated (Buchwitz et al., 2017; Frankenberg et al., 2005; Kort et al., 2014; Lyon et al., 2015; Turner et al., 2015). Rapid satellite-based identification of anomalously large methane sources in oil/gas fields could enable corrective action, but subkilometer pixel resolution is needed to pinpoint individual methane-emitting facilities (Cusworth et al., 2018; Jacob et al., 2016).

Here we present single-pass satellite observations of massive methane plumes from oil/gas production and transmission infrastructure. The observations were made with the GHGSat-D and TROPOMI satellite instruments over the Korpezhe oil/gas field in western Turkmenistan. Both instruments detected large point sources in the area on multiple overpasses between November 2017 and January 2019. We use two source rate retrieval techniques to quantify emissions from the individual plume observations and estimate total emissions over the observation period from the resulting time series of emissions. Our estimates are comparable to the 4-month total emission from the 2015 blowout at the Aliso Canyon natural gas storage facility in California, which was the largest methane leak in U.S. history (Conley et al., 2016; Thompson et al., 2016). These results suggest that extreme point source methane emissions from global oil/gas operations may be much larger than previously inferred for the United States (Lyon et al., 2015; Zavala-Araiza et al., 2015) and demon-

strate the potential for satellite instruments to guide efforts to reduce methane emissions from the oil/gas sector.

## 2.2 GHGSAT-D OBSERVATIONS

GHGSat-D is a lightweight satellite instrument ( $\sim$  15-kg spacecraft) that was launched into polar sun-synchronous orbit in June 2016 by the Indian Space Research Organization. The satellite is operated by the Canadian company GHGSat Inc., which seeks to demonstrate a global capability for detecting methane emissions at the facility scale from space. GHGSat-D measures atmospheric methane columns by solar backscatter in the shortwave infrared (SWIR) over the spectral range 1,630–1,675 nm, with an effective pixel resolution of  $50 \times 50 \text{ m}^2$  over targeted  $12 \times 12 \text{ km}^2$  scenes (McKeever et al., 2017; Sloan et al., 2016; see supporting information Section A.1). The measurements are made at about 10:00 local solar time, and the average return time is 2 weeks.

While targeting a mud volcano in the Balkan province of western Turkmenistan, GHGSat-D discovered on 13 January 2019 an anomalously large methane plume near the edge of its measurement domain, seemingly from a gas pipeline between the nearby Korpezhe gas production unit and compressor station, about 2 km from each facility. Another large plume originating from a piece of equipment near the compressor station was also seen on this day. Reviewing the GHGSat-D record for the scene going back to the first observation in February 2018, we found evidence of anomalously large methane plumes from three point sources corresponding to the compressor station, the connecting pipeline, and a smaller production facility about 7 km to the north. The plumes were observed in seven out of 13 clear-sky GHGSat-D observations made through the end of January 2019. The plume from the compressor station was repeatedly detected, while the plumes from the pipeline and the northern production facility were detected only once.

Figure 2.1 shows GHGSat-D detections of the three point sources overlaid on 2017 DigitalGlobe

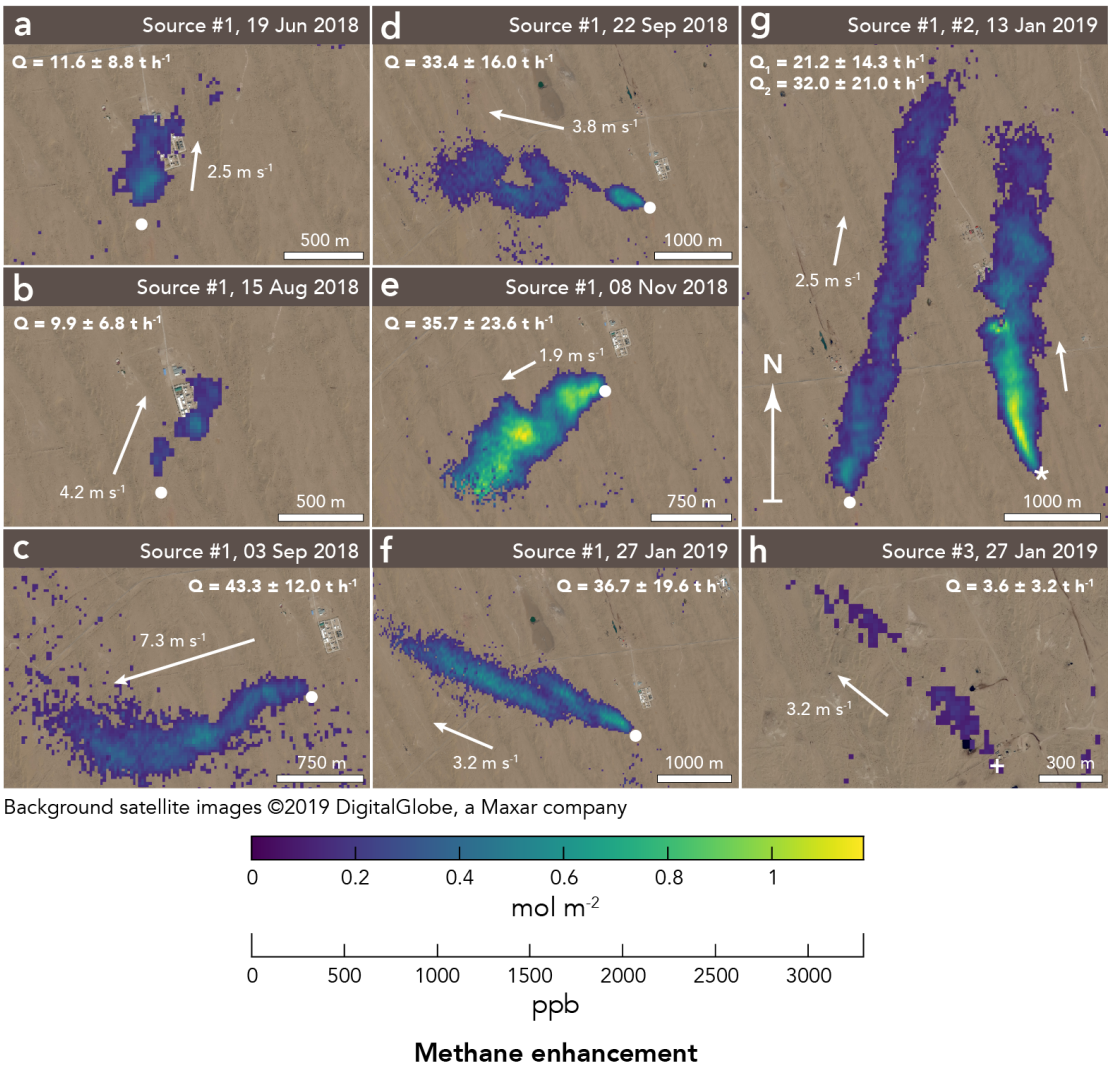
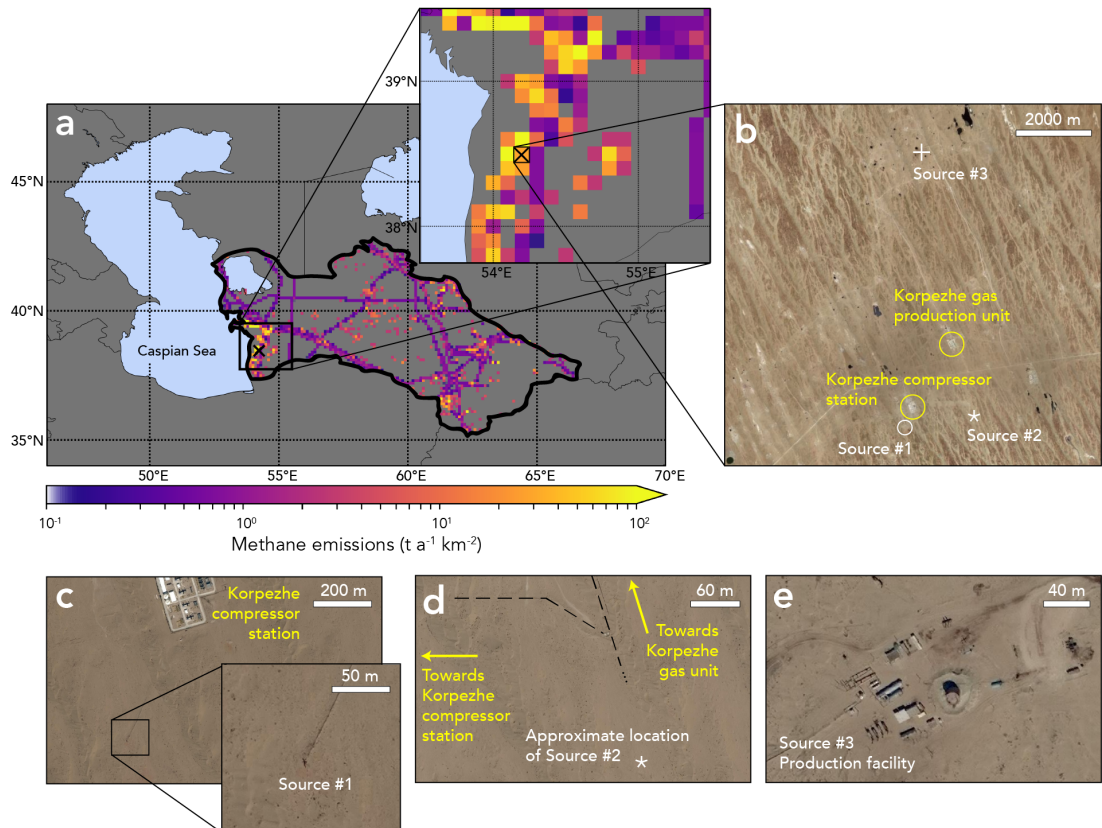


**Figure 2.1:** GHGSat-D observations of methane plumes in the Korpezhe oil/gas field of western Turkmenistan. (a–h) Plumes observed near the Korpezhe gas compressor station ( $38.499^{\circ}\text{N}$ ,  $54.199^{\circ}\text{E}$ , at sea level) between 24 February 2018 and 27 January 2019, with first detection on 19 June 2018. Methane enhancements relative to background for the scene are plotted as retrieved column enhancements ( $\text{mol m}^{-2}$ ) and converted (for illustrative purposes only) to column-averaged mixing ratios (ppb) based on sea level pressure. The plumes shown here have been segmented by thresholding at the 95th percentile, as discussed in Section A.3. DigitalGlobe background imagery showing the compressor station and its surroundings is from 2017. The white disk, star, and cross symbols mark the locations of (a–g) source #1, (g) source #2, and (h) source #3, respectively (also see Figure 2.2). The wind vectors show the GEOS-FP 10-m wind speeds for the observations paired with the wind directions estimated from the plume enhancements and used in the cross-sectional flux (CSF) method to retrieve source rates. The large plume shown in panel (e) is truncated by the edge of the GHGSat domain.

surface imagery of the Korpezhe oil/gas field. The most persistent source (source #1), located about 400 m southwest of the Korpezhe compressor station, appears in all seven GHGSat-D observations with detected plumes. The pipeline plume discovered on 13 January 2019 (source #2) extended more than 3 km downwind of the source location, as did the plume from source #1 on that day. The weakest source (source #3), at the northern production facility, was detected on 27 January 2019. The column density precision in these GHGSat-D observations is estimated from the variability of background columns to be 16% (see Section A.1). The plumes have peak enhancements of 25–175% above background. Plume enhancement magnitudes differ from scene to scene, which may reflect variations in source magnitude as well as in atmospheric transport (Varon et al., 2018). Large temporal fluctuations in methane emissions from oil/gas point sources have previously been observed with in situ measurements in the Barnett Shale region of northeast Texas (Lyon et al., 2015) and by airborne remote sensing in the Four Corners region of New Mexico (Frankenberg et al., 2016).

It is unclear what specific activities are responsible for these large plumes. Figure 2.2 shows 2011–2017 DigitalGlobe imagery of the three source locations. Source #1 may be the result of venting from the compressor station. Active fire data from the Visible Infrared Imaging Radiometer Suite (Schroeder et al., 2014) available since 2012 show no burning at the source location, suggesting that it is not a flare. Source #2 appears near a pipeline connection between the Korpezhe compressor station and gas production unit. DigitalGlobe imagery from 2004 (Figure A.1) shows the pipeline connection near source #2 under construction. A pipeline rupture would produce persistent emissions, but this is not the case here. Instead, blowdown or malfunction of an isolation valve on the pipeline branch may have produced the large emissions seen on 13 January 2019. Source #3 is a production facility. Numerous pieces of equipment could be responsible for the emissions detected from this facility on 27 January 2019.



Background satellite images ©2019 DigitalGlobe, a Maxar company

**Figure 2.2:** Methane emissions inventory data and surface imagery for the GHGSat scene. (a) Methane emissions from oil/gas production, refining, processing, transport, and storage across Turkmenistan, as estimated from a global inventory with  $0.1^\circ \times 0.1^\circ$  grid resolution by Scarpelli et al. (2020). The thick line shows the boundaries of Turkmenistan. The panel inset shows a closer view of the area around Korpezhe, with the inventory grid cell containing the compressor station marked by a black “x.” (b) DigitalGlobe imagery from 2011 to 2013 showing part of the GHGSat-D scene containing sources #1–#3. Also shown are close-up views of (c) source #1, which may be a vent at the end of an above-ground pipe extending about 400 m southwest of the Korpezhe compressor station ( $38.499^\circ\text{N}$ ,  $54.199^\circ\text{E}$ ); (d) source #2, between the Korpezhe compressor station and gas production unit ( $38.514^\circ\text{N}$ ,  $54.212^\circ\text{E}$ ), with dashed lines indicating the connecting pipeline based on DigitalGlobe imagery of the pipeline under construction in 2004 (Figure A.1); and (e) source #3 at the northern production facility ( $38.560^\circ\text{N}$ ,  $54.203^\circ\text{E}$ ). DigitalGlobe surface imagery in panels (c)–(e) is from 2017.

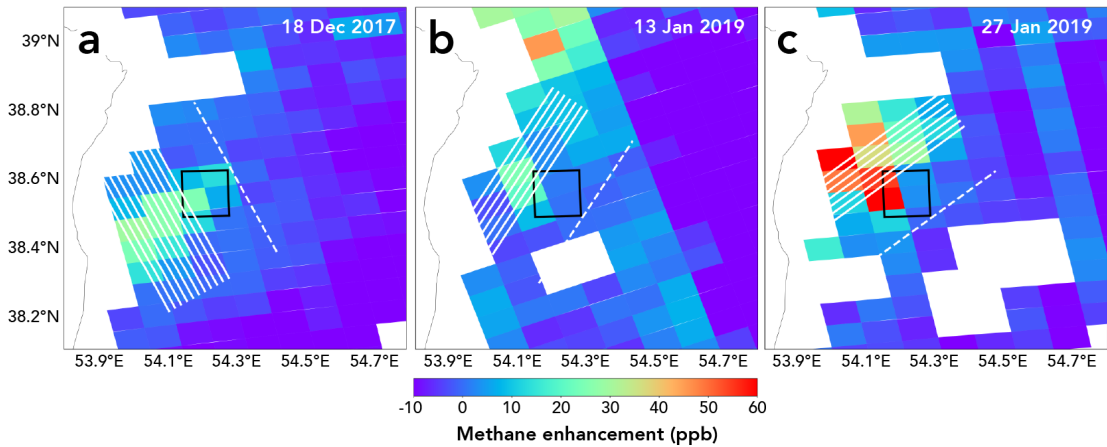


**Figure 2.3:** Sample TROPOMI observations of methane plumes in the Korpezhe oil/gas field. (a–c) TROPOMI methane measurements (level 2 product version 1.3.2) over the Korpezhe region on 18 December 2017, 13 January 2019, and 27 January 2019. The scenes from 13 and 27 January were selected for their concurrence with GHGSat-D observations (Figure 2.1). The GHGSat-D  $12 \times 12 \text{ km}^2$  domain is marked in each panel by a black square. The data represent the enhancement of methane column-averaged mixing ratio above background, where the background value is determined upwind of the GHGSat-D domain, along the dashed white line. Source strength is calculated from column concentrations along the white downwind transects, resulting in source rates of 33 (range 11–55)  $\text{t hr}^{-1}$ , 33 (6–60)  $\text{t hr}^{-1}$ , and 96 (73–124)  $\text{t hr}^{-1}$  for panels (a)–(c), respectively.

### 2.3 TROPOMI OBSERVATIONS

Previous methane observations made in 2004 by the SCIAMACHY satellite instrument with  $60 \times 30 \text{ km}^2$  nadir pixel resolution showed a general enhancement of methane across Turkmenistan (Buchwitz et al., 2017). Here we use methane observations from the TROPOMI satellite instrument launched in October 2017 to place the GHGSat-D plume observations in context. TROPOMI is in polar sun-synchronous orbit and provides global mapping of atmospheric methane columns on daily overpasses at about 13:00 local solar time with  $7 \times 7 \text{ km}^2$  nadir pixel resolution (Hu et al., 2018; Veefkind et al., 2012). Its average  $X_{\text{CH}_4}$  bias relative to reference ground-based column measurements from Total Carbon Column Observing Network (Wunch et al., 2011) stations is  $-4.3$  ppb, with a station-to-station variability of 7.4 ppb (Hasekamp et al., 2019).

Inspection of TROPOMI data for the GHGSat-D scene over Korpezhe confirms the presence

of anomalously large and persistent methane sources (Figure 2.3). TROPOMI first detected the sources on 16 November 2017, a few days after the instrument was switched on. Between 17 December 2017 and 31 January 2019, TROPOMI retrieved 128 successful cloud-free methane images over the Korpezhe region in which more than one pixel coincides with the GHGSat-D scene. Of these scenes, 24 were deemed suitable for emission quantification, based on the regularity of wind fields over the region (see Section A.2). Plumes could often be detected up to 30 km downwind and with peak enhancements of up to 9% above background. The longer extent of the TROPOMI plumes as compared to GHGSat-D plumes reflects TROPOMI’s higher instrument precision, and the weaker enhancements reflect dilution over its larger pixels. In total, GHGSat-D and TROPOMI detected anomalously large methane emissions near the Korpezhe gas facilities respectively in 54% and over 90% of observations made between 17 December 2017 and 31 January 2019.

## 2.4 SOURCE RATE QUANTIFICATION METHODS

We estimate the source rate for individual plumes using two alternative methods: the integrated mass enhancement or IME (Frankenberg et al., 2016; Jongaramrungruang et al., 2019; Varon et al., 2018) and the cross-sectional flux or CSF (White et al., 1976). These methods combine the observed plume column enhancements with wind speed data to infer source rate. Varon et al. (2018) give a detailed analysis of these methods as applied to satellite observations of atmospheric methane columns.

The IME method relates the source rate  $Q$  [mol s<sup>-1</sup>] to the total detected plume mass IME [mol]. It uses the plume enhancements  $\Delta\Omega_i$  [mol m<sup>-2</sup>] observed over  $i = 1, \dots, N$  plume pixels with area  $A_i$  [m<sup>2</sup>], an effective wind speed  $U_{\text{eff}}$  [m s<sup>-1</sup>], and a plume length scale  $L$  [m] to estimate  $Q$ :

$$Q = \frac{U_{\text{eff}}}{L} \text{IME} = \frac{U_{\text{eff}}}{L} \sum_{i=1}^N \Delta\Omega_i A_i. \quad (2.1)$$

Here  $N$  is obtained with a Boolean plume mask (see Section A.3) that distinguishes plume pixels from background pixels and  $L$  is defined as the square root of the total plume area  $\sum_{i=1}^N \Delta\Omega_i A_i$ . Varon et al. (2018) showed with an ensemble of large eddy simulations (LES) that  $U_{\text{eff}}$  can be related to the local 10-m wind speed  $U_{10}$  in a manner that depends on the instrument precision and on the procedure used to construct the plume mask, and we apply the same methodology here. The LES ensemble comprises 15 dry air plume simulations over flat terrain, with a range of initial wind speeds and boundary layer depths. We sample the simulations at different points in time to generate a data set of GHGSat pseudo-observations, which can be used to calibrate source rate retrieval equations customized to specific measurement conditions. Applying the LES ensemble to our GHGSat-D conditions (column density precision of 16%, plume mask constructed as described in Section A.3), we find  $U_{\text{eff}} = \log(U_{10}) + 0.5 \text{ m s}^{-1}$  (Figure A.2).

The CSF method infers source rate  $Q$  from column plume transects computed at different distances downwind of the source and perpendicular to the wind direction. Rotating the methane enhancements  $\Delta\Omega(x, y)$  [ $\text{mol m}^{-2}$ ] to align the plume with the  $x$  axis, we estimate  $Q$  from the mean plume transect  $\bar{C}$  [ $\text{mol m}^{-1}$ ] computed along the  $y$  axis at downwind distances  $x_j, j = 1, \dots, M$ :

$$Q = \bar{C} U_{\text{eff}} = \frac{U_{\text{eff}}}{M} \sum_{i=1}^M \int \Delta\Omega(x_j, y) dy. \quad (2.2)$$

For GHGSat-D plumes, we estimate wind direction from the shape of the plume (Figure 2.1), using a weighted mean of pixel coordinates with the column enhancements as weights. For TROPOMI plumes, we use wind direction information from the NASA Goddard Earth Observing System-Fast Processing (GEOS-FP) meteorological reanalysis product at  $0.25^\circ \times 0.3125^\circ$  resolution (Molod et al., 2012). The limits of the cross-plume integral in Equation 2.2 are defined by transects of fixed length for TROPOMI plumes (Figure 2.3) and by the Boolean plume mask constructed in the IME method for GHGSat-D plumes. The effective wind speed  $U_{\text{eff}}$  in Equation 2.2 is different than for

the IME method but can again be related to the local 10-m wind speed  $U_{10}$  using our LES ensemble. We obtain  $U_{\text{eff}} = 1.5 U_{10}$  (Figure A.2).

For GHGSat-D plumes, we apply both the CSF and IME methods as independent inferences of source rate, using hourly  $U_{10}$  data from GEOS-FP to estimate  $U_{\text{eff}}$ . Source rates obtained with the IME and CSF methods agree to within 50% for single-pass observations (Figure A.3), so we report the average of the two estimates for each plume (Figure 2.1 and Table A.1). Since the CSF method can be unreliable for  $U_{10} < 2 \text{ m s}^{-1}$  (Varon et al., 2018), we use only the IME method for the plume observed under low wind conditions on 8 November 2018 (Figure 2.1e). The source rate on this day may be underestimated due to the plume's truncation at the edge of the measurement domain. Errors on the source rates (Table A.1) are estimated following Varon et al. (2018) and are dominated by uncertainty in  $U_{10}$ . By comparing GEOS-FP  $U_{10}$  data with 5-min observations from U.S. airports (Horel et al., 2002), Varon et al. (2018) estimated an error of ( $1\sigma$ ) 2–2.5  $\text{m s}^{-1}$  when using GEOS-FP to estimate  $U_{10}$ , and we assume that the same error applies here. GEOS-FP 10-m wind speeds for our GHGSat-D scenes range from 1.9 to 7.3  $\text{m s}^{-1}$  (Figure 2.1), and the total errors in source rate range from 30% to 90% (larger error for low winds; see Table A.1 and Text S4). Relative source rate errors under low wind speed conditions are smaller than would be expected from  $U_{10}$  uncertainty of 2–2.5  $\text{m s}^{-1}$ , because relative errors in  $U_{\text{eff}}$  are generally smaller than those in  $U_{10}$ . This is due to the convexity of the effective wind speed function used in the IME method (see Figure A.2), which reduces variance in effective wind speed, and also more generally to wind speed being strictly positive, which reduces absolute error variance for slow compared to fast winds.

For plumes detected by TROPOMI, we use the CSF method with pressure-weighted average planetary boundary layer winds  $U_{\text{BL}}$  from GEOS-FP instead of  $U_{10}$ , and estimate errors on source rate from an ensemble of retrievals using different meteorological information, plume sampling, and background estimation schemes (see Section A.5). The quantification assumes a source confined to the GHGSat-D spatial domain and is performed with transects of length  $0.5^\circ$ , separated

by  $0.02^\circ$  along the plume axis (Figure 2.3). We characterize the relationship between  $U_{\text{eff}}$  and  $U_{\text{BL}}$  using the Weather Research and Forecasting model coupled with chemistry (WRF-Chem version 3.8.1; Grell & Freitas, 2014; Skamarock et al., 2008). WRF-Chem simulations of methane concentrations were performed at 1-km horizontal resolution over Korpezhe for all quantifiable plumes in January 2019 (13, 16, 24, and 27 January 2019), using analysis meteorological fields from National Centers for Environmental Prediction (2000). We modeled emissions for sources #1 – #3 using mean source rates inferred from the GHGSat-D observations and virtually sampled the resulting simulated methane fields with TROPOMI at 9:00 UTC (about 13:00 local solar time). Applying the CSF method to these simulated observations, we estimate the relationship between  $U_{\text{eff}}$  and  $U_{\text{BL}}$  by comparing the resulting source rates to the simulation ground truths. We find on average that  $U_{\text{eff}} = (1.05 \pm 0.17)U_{\text{BL}}$ . We then use this relationship to infer source rates from all of our TROPOMI observations (except those from January 2019, for which we use the specific  $U_{\text{eff}}-U_{\text{BL}}$  relationships derived from the corresponding simulations). Figure 2.4 shows the results, with vertical bars giving the ranges for the ensemble of retrievals. We take the half-length of these vertical bars to represent the uncertainty, amounting on average to 60% of the best estimate of the source rate. Source rates for the 24 quantified scenes are converted to a time-averaged source rate after correcting for representativeness by comparing the mean peak enhancement for these 24 scenes with the mean peak enhancement for the 128 scenes over the full observation record (see Section A.2).

## 2.5 SOURCE RATE ESTIMATES

From retrieval of source rates for the individual GHGSat-D plumes, we infer instantaneous values of  $9.9 \pm 6.8$  to  $43.3 \pm 12.0 \text{ t hr}^{-1}$  for the compressor station source (source #1),  $32.0 \pm 21.0 \text{ t hr}^{-1}$  for the pipeline source (source #2), and  $3.6 \pm 3.2 \text{ t hr}^{-1}$  for the northern facility (source #3). These rates are considerably larger than the  $0.3\text{--}2.0 \text{ t hr}^{-1}$  previously reported for anomalous (heavy-tail)

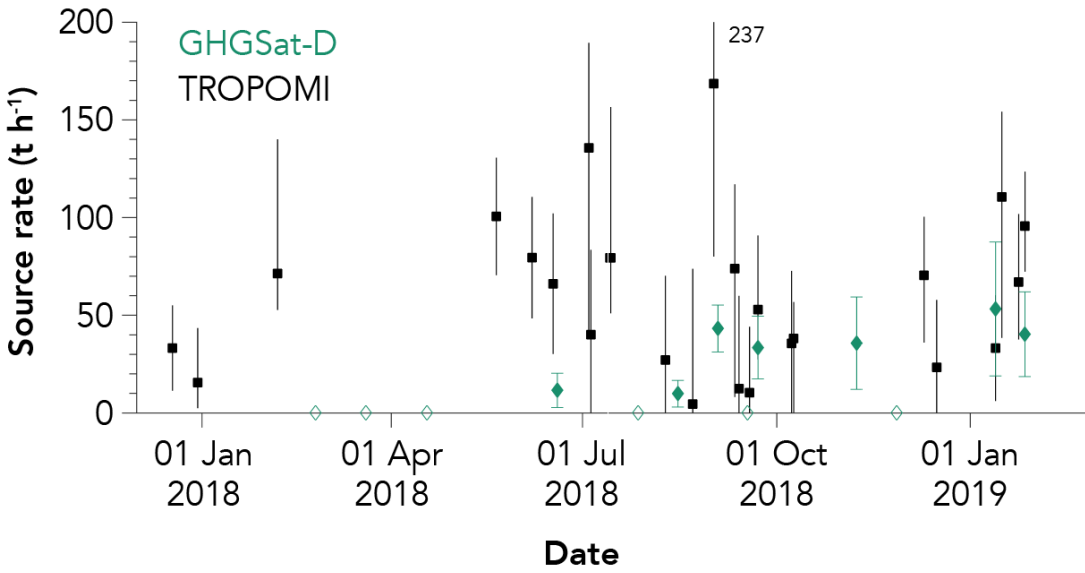


**Figure 2.4:** Time series of emissions from the Korpezhe  $12 \times 12 \text{ km}^2$  scene. Source rates inferred from GHGSat-D observations (green diamonds) include emissions from all plumes detected across the scene. Source rates inferred from TROPOMI observations (black squares) may include additional plumes within the scene and downwind. The GHGSat-D observation record is from 24 February 2018 to 27 January 2019, and the TROPOMI observation record is from 17 December 2017 to 31 January 2019. The green error bars represent error standard deviations ( $1\sigma$ ) on the source rates inferred from GHGSat-D observations. The black vertical bars represent the range of emissions inferred from the TROPOMI source rate retrieval ensemble for each quantified plume. Green open markers denote GHGSat-D scenes where no plumes were detected. TROPOMI source rates are from observations with quantifiable plumes; many TROPOMI detection events are not shown here due to ambiguity in inferring source rates.

point sources from oil/gas production in the United States (Lyon et al., 2015), including typical compressor station blowdown emissions of  $\sim 0.25 \text{ t hr}^{-1}$  (United States Environmental Protection Agency, 2006). They are comparable to emissions from major oil/gas accidents like the well-publicized 2015 Aliso Canyon (peak rate of  $60 \text{ t hr}^{-1}$ ; Conley et al., 2016; Thompson et al., 2016) and 2018 Ohio well pad (peak rate  $> 75 \text{ t hr}^{-1}$ ; Pandey et al., 2018; United States Environmental Protection Agency, 2018) blowouts.

Figure 2.4 shows the December 2017 to January 2019 time series of source rates estimated by GHGSat-D and TROPOMI for the  $12 \times 12 \text{ km}^2$  GHGSat-D scene. Source rates for GHGSat-D observations with multiple plumes are given as the total emissions for all plumes in the scene. This results in scene-wide emissions of  $9.9 \pm 6.8$  to  $53.2 \pm 34.3 \text{ t hr}^{-1}$  for observations with detected plumes, for a mean of  $32.5 \pm 7.7 \text{ t hr}^{-1}$  when plumes are present and  $17.5 \pm 4.2 \text{ t hr}^{-1}$  when including plume-free observations in the average. The uncertainties on these mean hourly rates are derived by propagating source rate error standard deviations from individual days (Figure 2.1 and Table A.1) through the calculation of the mean (see Section A.4). The range of source rates across all quantified TROPOMI observations is  $5\text{--}169 \text{ t hr}^{-1}$ , with a mean of  $60 \text{ t hr}^{-1}$  for quantifiable plumes and  $45 \text{ t hr}^{-1}$  over the full observation record. TROPOMI source rate estimates tend to be larger than those from GHGSat-D, possibly due to additional sources downwind of the GHGSat-D scene that would be incorporated into the broader TROPOMI plumes. In addition, GHGSat-D would miss point sources emitting below its detection threshold. Discrepancies in the source rate estimated with GHGSat-D and TROPOMI on days with concurrent measurements (e.g., 13 and 27 January 2019) may be partly attributable to these signal differences, but also to source rate retrieval error and temporal variability of emissions during the roughly 3-hr window between instrument overpasses.

If our ensemble of GHGSat-D and TROPOMI observations is representative of emissions from the Korpezhe  $12 \times 12 \text{ km}^2$  scene over the instruments' observation periods, we estimate to-

tal methane emissions of  $142 \pm 34$  kt from the three sources detected by GHGSat-D between 24 February 2018 and 27 January 2019 ( $\approx 153 \pm 37$  kt  $a^{-1}$ ) and 446 (189–750) kt for the ensemble of sources detected by TROPOMI between 17 December 2017 and 31 January 2019 ( $\approx 396$  [168–666] kt  $a^{-1}$ ). Estimated emissions from the Korpezhe compressor station source alone are  $120 \pm 27$  kt for the February 2018 to January 2019 period ( $\approx 129 \pm 29$  kt  $a^{-1}$ ) according to GHGSat-D. For comparison, the 2015 Aliso Canyon blowout emitted 97 kt of methane to the atmosphere over a 4-month period (Conley et al., 2016), and the largest reported methane point sources in the United States (coal mines and landfills) emit 10–100 kt  $a^{-1}$  (Jacob et al., 2016). Our estimates of total and annual emissions from the Korpezhe sources are calculated by multiplying average retrieved source rates by duration (e.g., 1 year), with all observations counted in the average (including nondetections, for which we assume zero emissions). The assumption of representative sampling is more reliable for TROPOMI than for GHGSat-D, both because the TROPOMI data set has larger sample size and because with its coarser pixels TROPOMI sees emissions integrated over longer periods of time (several hours).

## 2.6 CONCLUSION

Our discovery of anomalously large methane emissions associated with the Korpezhe gas compressor station in western Turkmenistan demonstrates the value of satellites for identifying and monitoring methane emissions at the facility scale worldwide. Anomalous point sources are known to make a disproportionately large contribution to the total methane emission from oil/gas production (Alvarez et al., 2018; Zavala-Araiza et al., 2015), and our results indicate that this contribution could be even larger than has been previously recognized. Detection of these point sources using satellite observations could enable corrective action to significantly reduce methane emissions from the oil/gas sector. GHGSat-D serves as demonstration for a future constellation of GHGSat satellite

instruments to be launched starting in 2020 with improved column density precision (McKeever et al., 2017). The synergy with TROPOMI observations demonstrated here points to a promising observation strategy in which coarse identification of methane hot spots by TROPOMI can guide fine-resolution satellites like GHGSat-D to identify the specific facilities responsible for the hot spots and direct intervention accordingly.

#### ACKNOWLEDGEMENTS

We thank O. B. A. Durak and J. J. Sloan for their roles in developing the GHGSat retrievals algorithm and measurement concept. We thank C. Herzog, M. Arias, and K. Wisniewski for technical assistance and preparation of the GHGSat-D methane data. We thank the team that realized the TROPOMI instrument and its data products, consisting of the partnership between Airbus Defense and Space, KNMI, SRON, and TNO, commissioned by NSO and ESA. Sentinel-5 Precursor is part of the EU Copernicus program, and Copernicus (modified) Sentinel data 2017–2019 have been used. D. J. J. was supported by the Carbon Monitoring System of the NASA Earth Science Division. S. P. is funded through the GALES project (15597) by the Dutch Technology Foundation STW, which is part of the Netherlands Organization for Scientific Research (NWO), and is partly funded by Ministry of Economic Affairs. Part of this work was carried out on the Dutch national e-infrastructure with the support of SURF Cooperative.

3

# Quantifying Time-Averaged Methane Emissions from Individual Coal Mine Vents with GHGSat-D Satellite Observations

SATELLITE OBSERVATIONS OF ATMOSPHERIC METHANE PLUMES offer a means for global mapping of methane point sources. This capability has so far been demonstrated only for anomalously large or regionally aggregated point sources. Here we use the GHGSat-D satellite instrument with 50-m spatial resolution and 9–19% single-pass column precision to quantify mean source rates for three coal mine vents (San Juan, United States; Appin, Australia; Bulianta, China) under apparently normal operating conditions and over a 2-year period (2016–2018). This involves averaging wind-rotated observations from 13–24 overpasses to achieve satisfactory signal-to-noise. Our wind rotation method optimizes the wind direction information for individual plumes to account for error in meteorological databases. We derive source rates from the time-averaged plumes using integrated mass enhancement (IME) and cross-sectional flux (CSF) methods calibrated with large eddy simulations (LES). We find time-averaged source rates ranging from 2150 to 5690 kg h<sup>-1</sup> for the three coal mine vents, with about 40% precision, and generally consistent with previous estimates,

which are however highly variable. The IME and CSF methods agree within 15%. Our  $2300 \pm 1020$   $\text{kg h}^{-1}$  estimate for the San Juan mine is consistent with the annual mean value of  $2585 \text{ kg h}^{-1}$  for 2017 reported to the United States Greenhouse Gas Reporting Program (GHGRP). Our results demonstrate the potential of space-based monitoring for annual reporting of methane emissions from point sources, and suggest that future satellite instruments with similar pixel resolution but better precision should be able to constrain a wide range of point sources.

### 3.1 INTRODUCTION

Methane is a powerful greenhouse gas with large anthropogenic sources. It has contributed  $1.0 \text{ W m}^{-2}$  to radiative forcing since pre-industrial times on an emission basis (IPCC, 2013). Underground coal mine vents are among the largest individual point sources of methane (Maasakkers et al., 2016) and are estimated to account for  $\sim 10\%$  of global anthropogenic methane emissions (Saunois et al., 2016), but source reporting is highly uncertain. Remote sensing of atmospheric methane by solar backscatter in the shortwave infrared (SWIR) can be effective for quantifying point sources (Jacob et al., 2016; Duren et al., 2019). Krings et al. (2013) used aircraft remote sensing data to quantify methane emissions from coal mine vents in Germany. Frankenberg et al. (2016) conducted an aircraft remote sensing study of coal mine plumes in the Four Corners region of the Southwest United States and found the emissions to be highly variable and intermittent. Global-observing satellite instruments have demonstrated the capability to characterize methane emissions on regional scales (Turner et al., 2015; Maasakkers et al., 2019; Miller et al., 2019) and from anomalously large sources (Pandey et al., 2019), but are limited by relatively coarse imaging resolution ( $\sim 10 \text{ km}$ ). The GHGSat-D satellite instrument overcomes this limitation by conducting high-resolution observations of point sources over targeted domains (Varon et al., 2019). Here we demonstrate the capability of GHGSat-D to observe methane plumes from individual coal mine

vents and infer time-averaged source rates.

GHGSat-D was launched in June 2016 as demonstration for a future constellation of small satellites to monitor individual methane point sources from space (Brakeboer, 2015; Sloan et al., 2016). Since then, single-pass GHGSat-D observations have revealed anomalously high-emitting facilities in oil/gas fields with source rates exceeding  $10,000 \text{ kg h}^{-1}$  (Varon et al., 2019). The largest methane point sources under normal operating conditions are the vents of large underground coal mines, typically in the range  $1000\text{--}10,000 \text{ kg h}^{-1}$  (Krings et al., 2013; Frankenberg et al., 2016; Smith et al., 2017; Jacob et al., 2016). Here we show that time-averaging of wind-rotated GHGSat-D observations can enable detection and quantification of methane emissions from individual coal mine vents, adapting an approach previously applied to satellite observations of point sources for CO (Pommier et al., 2013), SO<sub>2</sub> (Fioletov et al., 2015; McLinden et al., 2016), NO<sub>2</sub> (Valin et al., 2013; de Foy et al., 2015; Zhang et al., 2019), and NH<sub>3</sub> (Clarisso et al., 2019; Dammers et al., 2019), but including significant innovation to account for large errors and limited number of observations. Time-averaging is necessary here to achieve satisfactory signal-to-noise, but it also has the advantage of smoothing over intermittent sources and providing the annual emission estimates most relevant for national emission reporting and global methane budget analyses.

## 3.2 MATERIALS AND METHODS

### 3.2.1 GHGSAT-D OBSERVATIONS

GHGSat-D uses a miniature Fabry-Perot interferometer with spectral bandpass 1630–1675 nm (McKeever et al., 2017; Varon et al., 2019). The measurements are made at 50-m effective pixel resolution over  $\sim 12 \times 12 \text{ km}^2$  targeted domains. Methane column concentrations are retrieved from the resulting spectra using a 100-layer, clear-sky radiative transfer model in an inverse modelling framework, following Rodgers (2000) and as described by Varon et al. (2019). The inversion re-

trieves the total column concentrations  $\Omega(x, y)$  [mol m<sup>-2</sup>] of methane across the scene, based on HITRAN absorption line spectra (Gordon et al., 2017) and U.S. Standard Atmosphere vertical profiles (NASA 1976). The column mass enhancements  $\Delta\Omega(x, y) = \Omega(x, y) - \Omega_b$  then characterizes the plume relative to the local background column concentration  $\Omega_b$  [mol m<sup>-2</sup>] inferred from the scene. The inversion also retrieves albedo, CO<sub>2</sub>, and water vapor. The work presented here includes a correction of retrieval errors from aliased surface properties and other measurement parameters (McKeever et al., 2017).

GHGSat-D has an average revisit time of about two weeks, depending on latitude, and requires clear skies for successful observation. Since its launch in June 2016, it has repeatedly targeted the vents of three underground coal mines: the San Juan mine in New Mexico, USA; the Appin mine in New South Wales, Australia; and the Bulianta mine in Inner Mongolia, China. These coal mines were selected for their large coal production rates and/or previous reports of large methane emissions (SACMS 2011; Frankenberg et al., 2016; Ong et al., 2017; Smith et al. 2017). Here we examine GHGSat-D observations of the coal mine vents taken between August 2016 and December 2018, totalling 13–24 cloud-free observations per mine (see Table 3.1). The Appin mine was closed beginning on 28 June 2017 due to safety concerns and partially re-opened on 13 October 2017. We discard the four cloud-free observations made during this extended closure, leaving a total of 13 observations for analysis. Several other shorter closures occurred at Appin during the observation period, but these did not overlap with our measurements.

Figure 3.1 shows methane column enhancements from individual GHGSat-D scenes centred on the San Juan coal mine vent. These scenes were chosen for their detectable plumes, but also illustrate GHGSat-D retrieval artefacts resulting primarily from striping noise, surface reflectance variability, and stray light. Some artefacts are similar in magnitude to the plumes, which highlights the importance of prior knowledge of source location. Column precisions for our San Juan, Appin, and Bulianta observations are estimated at 9%, 19%, and 12% of background, respectively, based on

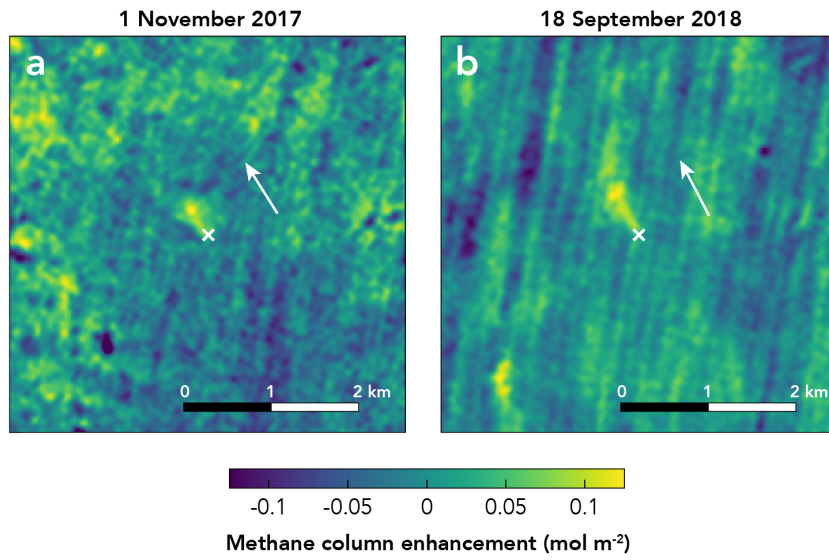


**Figure 3.1:** Instantaneous plumes observed by GHGSat-D over the San Juan mine in New Mexico on (a) 1 November 2017 and (b) 18 September 2018. The white 'x' symbols mark the location of the coal mine vent ( $36.792^{\circ}\text{N}$ ,  $108.389^{\circ}\text{W}$ ) and the white arrows show wind direction inferred from the orientation of the plumes (see text).

the standard deviations of non-plume column enhancements across the scenes. Most scenes do not feature readily detectable plumes, which motivates our time-averaging analysis.

### 3.2.2 WIND DATA FOR TIME-AVERAGING

Time-averaging of plume observations to improve signal-to-noise and infer emissions from point sources requires knowledge of wind speed and direction for the individual scenes (Pommier et al., 2013; Valin et al., 2013; de Foy et al., 2015; Fioletov et al., 2015; McLinden et al., 2016; Zhang et al., 2019; Clarisse et al., 2019; Dammers et al., 2019; Hill & Nassar, 2019). Wind information can come from local measurements, from assimilated meteorological databases, or directly from the plume observations themselves (Jongaramrungruang et al., 2019). The appropriate wind averaging time for an individual scene depends on the lifetime of the detectable plume before turbulent diffusion dilutes it to below detectable levels. It ranges from  $\sim 5$  minutes for a small plume to  $\sim 1\text{ h}$  for a large

plume several km in extent (Varon et al., 2018). Coal mine vent plumes as observed by GHGSat-D tend to be small (< 1 km in scale; Figure 3.1) and are therefore best interpreted with an averaging time of about 5 minutes.

Our algorithm to relate plume concentrations to emissions uses 10-m wind information (Varon et al., 2018). We take this information from two hourly meteorological databases: (1) the NASA Goddard Earth Observing System – Fast Processing (GEOS-FP) reanalysis product with full global coverage at  $0.25^\circ \times 0.3125^\circ$  resolution (Molod et al., 2012), and (2) the DarkSky online weather application programming interface (API) with partial coverage ([darksky.net/dev](https://darksky.net/dev)). Comparison with one month of daytime (15:00–21:00 UTC) wind measurements from 10 U.S. airports in the MesoWest database (Horel et al. 2002) suggests that GEOS-FP has more precise wind speed data than DarkSky, while DarkSky has more precise wind direction data. Error standard deviations on hourly average wind speed and direction from GEOS-FP are  $1.5 \text{ m s}^{-1}$  and 49 degrees relative to the airport measurements, compared to  $2.2 \text{ m s}^{-1}$  and 37 degrees for DarkSky. We therefore use GEOS-FP winds as default, but substitute DarkSky wind direction where available. DarkSky winds are available for nearly all our observations of the San Juan and Appin mines, but not for Bulianta.

Figure 3.2 shows the wind direction error statistics when using meteorological reanalysis data to infer local wind direction as referenced by the MesoWest database. The error depends strongly on wind speed, with larger errors at low wind speeds, as would be expected from turbulence. The error on the mean hourly wind in the meteorological databases (Figure 3.2, left panel) is compounded for small plumes by the error in inferring the more appropriate 5-minute average wind (Figure 3.2, right panel), in which case the two errors are added in quadrature. For observations with strong instantaneous plumes (Figure 3.1), we estimate wind direction directly from the plume axis, which we define from a weighted mean of pixel coordinates with the plume column concentrations as weights. The wind direction error in that case is estimated to be 5 degrees.

For a given point source, a time-averaged plume over the GHGSat-D record can be constructed

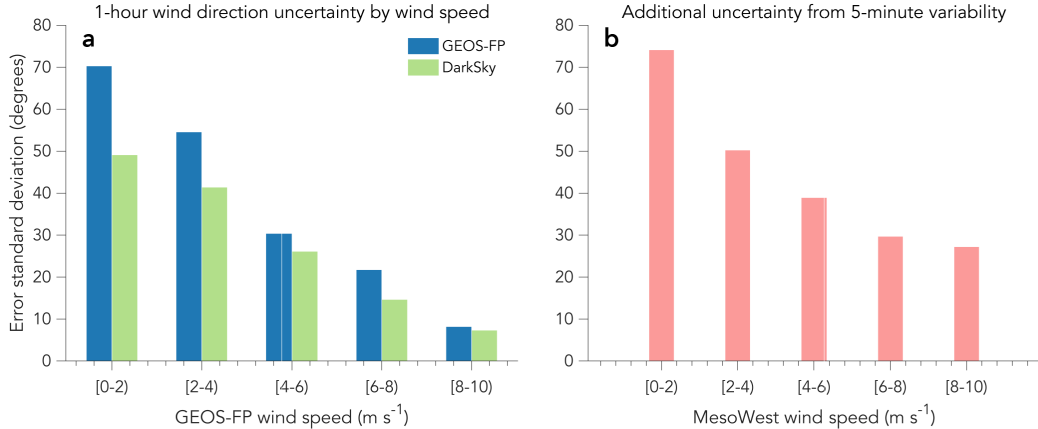


**Figure 3.2:** Error in estimating 10-m wind direction from the GEOS-FP and DarkSky datasets. (a) Error standard deviations for GEOS-FP and DarkSky hourly average wind direction relative to one month of measurements from 10 U.S. airports (ABQ, ATL, BOS, DFW, LAX, MCI, MSP, PDX, PHL, and PHX) in the MesoWest database, binned by GEOS-FP wind speed. The airport measurements are for daytime June 2017 (15:00–21:00 UTC). (b) Additional uncertainty for estimating 5-minute wind direction from 1-hour averages, based on 5-minute wind direction variability in the MesoWest data.

from the methane column enhancements  $\Delta\Omega_i(x, y)$  [ $\text{mol m}^{-2}$ ] observed over the source domain  $(x, y)$  on individual days  $i = 1 \dots N$ . This is done by (1) georeferencing and aligning the observations on a common grid, (2) rotating each observation around the known source location by the local wind direction  $\theta_i$ , and (3) computing per-pixel means over the rotated observations. The alignment and rotation steps require precise knowledge of the source location at the scale of the observations. The rotation step may introduce negative bias from wind direction uncertainty, as a misrotated plume may be lost in the noisy background of the time-averaged observation. We account for this bias through our source rate retrieval method, as described in Section 3.2.5 below.

### 3.2.3 OPTIMIZING WIND DIRECTIONS

Wind direction errors in the meteorological databases are relatively large, particularly for small plumes under low wind conditions (Figure 3.2). Here we correct the wind directions used for plume rotation in order to maximize concentrations in the time-averaged plume while minimizing devia-

tion from prior wind estimates. Specifically, we maximize the joint Gaussian probability distribution  $P(\theta)$  given by

$$\log P(\theta) = -\frac{(M(\theta) - M_{\max})^2}{\delta^2} - (\theta - \theta_a)^T S_a^{-1}(\theta - \theta_a) \quad (3.1)$$

by minimizing  $-\log P(\theta)$ . Here,  $\theta$  is a wind direction vector whose elements  $\theta_i, i = 1\dots N$ , are the wind directions used to rotate  $N$  GHGSat-D observations;  $\theta_a$  is a vector of prior wind direction estimates for the observations, from GEOS-FP and DarkSky;  $S_a$  is the (diagonal) prior error covariance matrix describing uncertainty in the prior wind direction, which depends on wind speed, plume lifetime (here 5 minutes), and whether the prior is drawn from GEOS-FP, DarkSky, or the plume itself;  $M(\theta)$  [mol] is the total methane mass (integrated mass enhancement, or IME) in a wedge-shaped mask placed downwind of the source after time-averaging with a set of wind directions  $\theta$  (see below);  $M_{\max}$  [mol] is the maximum possible value of  $M(\theta)$  for the set of observations when no constraints are placed on  $\theta$ ; and  $\delta^2$  [mol<sup>2</sup>] is the error variance in  $M(\theta)$  due to GHGSat-D measurement noise. We minimize  $-\log P(\theta)$  numerically using the Nelder-Mead simplex algorithm (Nelder & Mead, 1965; Lagarias et al., 1998).

We rotate individual observations by their wind direction such that the rotated wind is by convention from the north.  $M(\theta)$  is computed at each iteration of the optimization procedure as the IME over a simple wedge-shaped mask extending 500 m south and  $\pm 15$  degrees of south. The IME is the sum of column enhancements  $\Delta\Omega(x, y)$  over the mask, multiplied by the pixel area. We then compute  $M_{\max}$  by rotating the mask around the source location by 360 degrees in each observation, recording for each the maximum IME, and averaging over all observations. To calculate  $\delta$ , we perform time averaging using our prior wind directions, and then compute the IME within the wedge-shaped mask when placed at 100 random non-plume locations across the time-averaged domain; the standard deviation of these results gives  $\delta$ .

### 3.2.4 DEFINING PLUME BOUNDARIES

Inferring source rates from plume observations requires a mask that distinguishes plume pixels from the image background. Varon et al. (2018) suggested a *t*-test procedure for isolating plumes from normally distributed measurement noise, but that procedure's performance is limited here by systematic errors in the time-averaged observations. Instead, we isolate the plumes by applying an enhancement threshold at the 98th percentile of  $\Delta\Omega(x, y)$  over the time-averaged domain. This defines a threshold mask for the scene. To delete random classification errors and reduce loss of plume enhancements at mask edges due to thresholding, we smooth the masks with a  $150 \times 150 \text{ m}^2$  median filter, which replaces each pixel's value with the median of its  $150 \times 150 \text{ m}^2$  neighbourhood, followed by a Gaussian filter with standard deviation 50 m. Wind rotation and time averaging smooth out most of the observation artefacts such as those seen in Figure 3.1, but some still remain in the mask. For the purpose of inferring point source rates, we only consider the continuous portion of the mask originating from the source location.

### 3.2.5 ESTIMATING SOURCE RATES

We estimate source rates for our time-averaged plumes using two different methods: the IME method and the cross-sectional flux (CSF) method (Varon et al., 2018). The IME method relates the source rate  $Q [\text{mol s}^{-1}]$  to the detectable plume mass IME [mol] in terms of an effective wind speed  $U_{\text{eff,IME}} [\text{m s}^{-1}]$  and plume size  $L [\text{m}]$ :

$$Q = \frac{U_{\text{eff,IME}}}{L} \text{IME} = \frac{U_{\text{eff,IME}}}{L} \sum_{j=1}^n \overline{\Delta\Omega}(x_j, y_j) A_j, \quad (3.2)$$

where  $\overline{\Delta\Omega}(x_j, y_j) A_j, j = 1 \dots n$ , is the time-averaged column concentration of the  $j$ th plume pixel with coordinates  $(x_j, y_j)$  and area  $A_j$ , and the summation is over the  $n$  pixels within the continuous

plume mask originating from the source location. The plume size  $L$  is defined following Varon et al. (2018) as the square root of the plume mask's area. The effective wind speed  $U_{\text{eff,IME}}$  is an operational parameter that is inferred from the local 10-m wind speed  $U_{10}$  in a manner that depends on the definitions of the plume mask and size. We discuss the  $U_{\text{eff}} = f(U_{10})$  relationship below. The CSF method originally introduced by White (1976) and adapted to column observations by Krings et al. (2011, 2013) and Varon et al. (2018) relates  $Q$  to a cross-plume concentration integral [mol m<sup>-1</sup>] and a different effective wind speed  $U_{\text{eff,CSF}}$  than in the IME method:

$$Q = U_{\text{eff,CSF}} \int_a^b \overline{\Delta\Omega}(x, y) dy. \quad (3.3)$$

Here the  $x$ -axis is defined by the wind direction (northerly by convention for our time-averaged plumes) and the  $y$ -axis is perpendicular to the wind direction. The integral is computed between the plume boundaries  $[a, b]$  defined by the plume mask, and this computation can be done at multiple downwind distances  $x$  to improve estimation of  $Q$  through averaging. Here we repeat the calculation at pixel-width intervals across the full extent of the detectable plume.

The effective wind speeds in the IME and CSF methods are operational parameters that can be related to the local 10-m wind speed  $U_{10}$ . Varon et al. (2018) calibrated  $U_{\text{eff}} = f(U_{10})$  relationships for instantaneous plumes generated by large eddy simulation (LES), but the relationships may be different here for two reasons. First, we use a different definition of the plume mask, as described in the previous section. This affects the dependence of IME and plume transects on  $Q$ . Second, the dependences of IME (or plume transects) on wind speed and source rate may be different for time-averaged compared to instantaneous plumes.

Here we calibrate new  $U_{\text{eff}} = f(U_{10})$  relationships for the IME and CSF methods, customized to our observing conditions and plume mask. To do this, we repeat the LES plume analysis of Varon et al. (2018) on the same ensemble of simulations, but with time-averaged rather than instantaneous

plumes. The LES ensemble comprises 15 five-hour simulations with a range of wind speeds and boundary layer depths. We calibrate  $U_{\text{eff}} = f(U_{10})$  relationships for each coal mine independently, since for each we have a different number of observations and level of background noise. We use the following procedure. First, a number of LES plume snapshots are randomly drawn from the ensemble (24 for San Juan, 13 for Appin, and 14 for Bulianta). The source rate for the plumes is set to  $2500 \text{ kg h}^{-1}$  as a typical value for large coal mine vent emissions (Jacob et al., 2016); this only affects the size of the detectable plumes and hence the plume mask. Each snapshot is rotated by a random wind direction, and the 5-minute average value of  $U_{10}$  at the source location is recorded. We corrupt the plume snapshots with normally distributed, spatially uncorrelated noise of mean zero and standard deviation dependent on the observation conditions of each mine (9%, 19%, or 12% of a 1850 ppb background). We then follow the wind direction optimization procedure outlined above (Equation 3.1) to recover the LES plume wind directions from the randomly corrupted prior estimates, and assemble in this manner a time-averaged plume pseudo-observation. After constructing the plume mask and calculating IME,  $L$ , and the mean transect for the time-averaged plume, we use Equations 3.2 and 3.3 to compute  $U_{\text{eff}}$  based on prior knowledge of  $Q$  ( $2500 \text{ kg h}^{-1}$ ). Meanwhile, we compute  $U_{10}$  for the time-averaged observation as the mean of the 5-minute averages across aggregated plumes. We repeat this procedure 100 times on a set of LES plumes comprising 80% of the ensemble ( $\sim 2900$  plume snapshots), simulating 100 time-averaged plumes. We then derive the  $U_{\text{eff}} = f(U_{10})$  relationships by least squares fitting. Finally, to quantify source rate retrieval error, we evaluate these relationships on time-averaged plumes constructed from the remaining 20% of the LES plume ensemble (see Appendix B).

Figure 3.3 shows our derived  $U_{\text{eff}} = f(U_{10})$  relationships for the three coal mines. We find that linear relationships without intercepts capture the behaviour well in all cases, but the slopes depend on the number of observations aggregated, level of measurement noise, and wind direction prior error variance. As detecting the source becomes more difficult (due to fewer observations being avail-

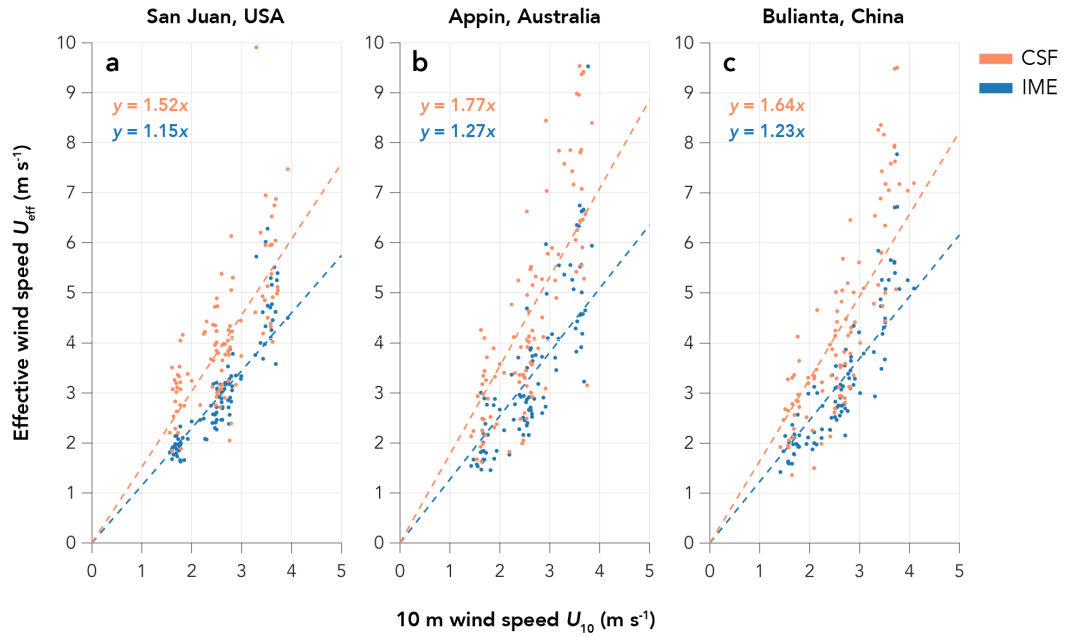


**Figure 3.3:** Effective wind speeds  $U_{\text{eff}}$  for retrieving time-averaged methane source rates by the integrated mass enhancement (IME) and cross-sectional flux (CSF) methods (Equation 3.2 and 3.3) as a function of the time-averaged 10-m wind speed  $U_{10}$ . The  $U_{\text{eff}} = f(U_{10})$  relationships are derived from large eddy simulations (LES) of instantaneous methane plumes, with time-averaging and wind rotation corresponding to our measurement conditions for (a) San Juan, (b) Appin, and (c) Bulianta. Each point represents a time-averaged plume assembled from LES instantaneous plumes, with the level of background noise and number of observations adapted to the mine of interest (see Table 3.1). The functions are fit by robust least squares (see text).

able, stronger measurement noise, and/or worse wind direction priors), the slopes steepen to make up for loss of mass at the plume boundaries. The winds are fit by robust linear regression, which assigns less weight to outlier points, to mitigate the considerable scatter in  $U_{\text{eff}}$  for larger values of  $U_{10}$ .  $U_{\text{eff}} = f(U_{10})$  slopes for the CSF method are similar to the results of Varon et al. (2018), but slopes for the IME method are significantly different.

### 3.3 RESULTS AND DISCUSSION

#### 3.3.1 TIME-AVERAGED PLUMES

Figure 3.4 shows our time-averaged rotated observations of the San Juan, Appin, and Bulianta coal mine vents, both before and after wind direction optimization. The plumes are oriented to the south of the source location by convention, and are separated from the noisy background by thresholding and smoothing as discussed in Section 3.2.4. Enhancements above the threshold but not directly downwind of the source location are ignored as retrieval artefacts.

Before optimizing wind direction to improve plume-to-noise contrast, the San Juan and Appin mine vents show strong time-averaged plumes with respective peak enhancements 7% and 20% above background. The Bulianta mine vent shows peak downwind enhancements 8% above background, but a less distinctive plume shape. One possible explanation for this is that the Bulianta vent is at the base of a hill, leading to large and potentially systematic wind direction error, in contrast to the San Juan and Appin vents, which are in flat terrain. Optimizing wind direction amplifies the plumes' mean enhancements by 11–13% and produces a more elongated plume shape for the Bulianta coal mine, with peak methane enhancements more than 10% above background. Peak plume enhancements do not generally appear at the source location, contrary to what one would expect. This could be because of systematic retrieval errors over the vent location (for example due to surface reflectance variability or aerosol particles in the plume). Missing large enhancements near the

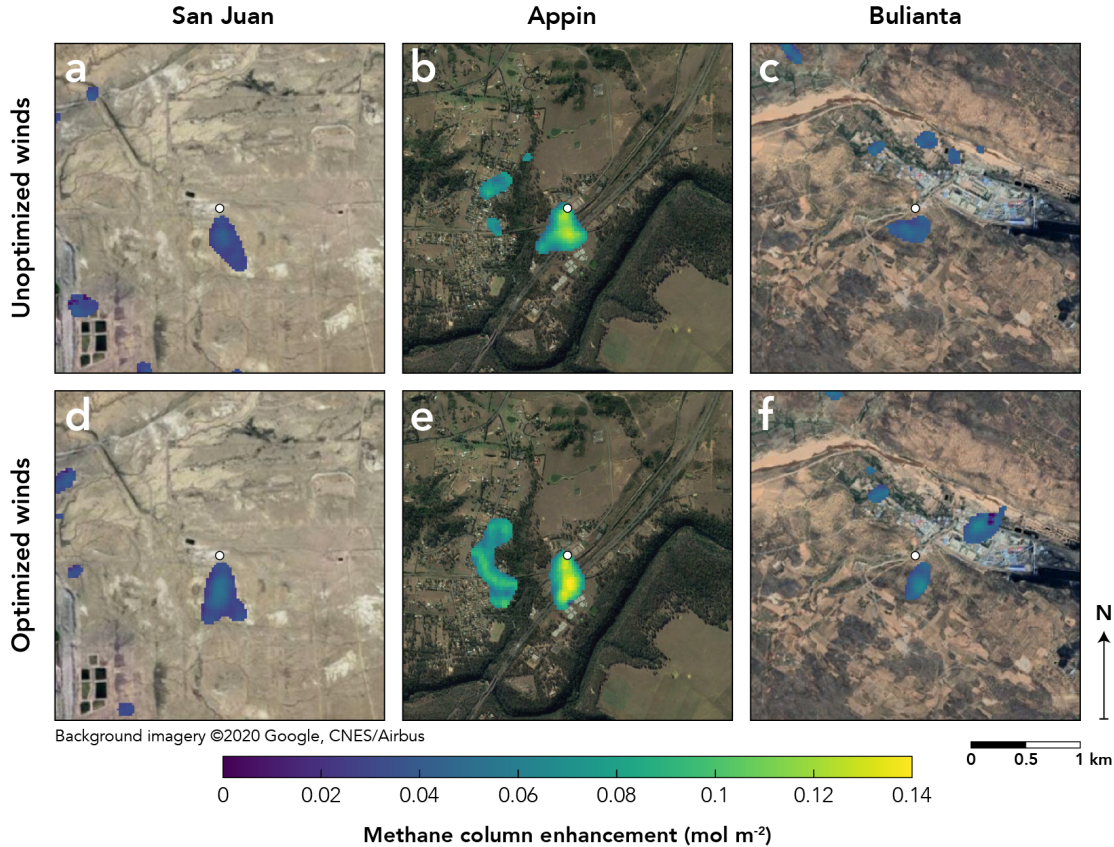


**Figure 3.4:** Time-averaged methane plumes from the San Juan, Appin, and Bulianta coal mine vents, as observed by GHGSat-D from August 2016 through December 2018. The single-pass observations have been rotated to a northerly wind direction using (a-c) local wind data from GEOS-FP and DarkSky and (d-f) optimized wind directions with GEOS-FP and DarkSky winds as prior estimates (see text). The methane column enhancements are overlaid on Google Earth Pro imagery after thresholding and smoothing with median and Gaussian filters (see text). The white markers show the locations of the coal mine vents in the centre of each scene.

vent could lead to a low bias in IME emission rate estimates, but would have a smaller effect on the CSF method, where each cross-plume integral downwind of the source independently approximates the emissions.

### 3.3.2 TIME-AVERAGED SOURCE RATES

Table 3.1 shows our time-averaged source rate estimates for the San Juan, Appin, and Bulianta mines determined from the wind-optimized plumes. Estimates from the IME and CSF methods agree within their error standard deviations, which is a first check that our effective wind speed functions are well-calibrated. We estimate mean emissions of  $2300 \pm 1020 \text{ kg h}^{-1}$  for the San Juan vent,  $5690 \pm 2540 \text{ kg h}^{-1}$  for the Appin vent, and  $2600 \pm 1010 \text{ kg h}^{-1}$  for the Bulianta vent using the IME method. The estimates are 7–13% lower using the CSF method, contradicting the possibility of low bias in the IME method. The uncertainties are about 40% and incorporate wind speed error, error in the IME and CSF models (including wind direction error and uncertainty in the effective wind speed fits of Figure 3.3), and correlated random noise in the retrieved columns. A detailed error analysis is presented in Appendix B.

Also shown in Table 3.1 are previous emission estimates for each of the mine vents, all from much smaller samples and/or durations. Frankenberg et al. (2016) estimated emissions of 360–2800  $\text{kg h}^{-1}$  for the San Juan vent based on several days of aircraft remote sensing measurements, and Smith et al. (2017) inferred mean emissions of  $1446 \text{ kg h}^{-1}$  from five days of aircraft mass balance measurements during the same period. Quarterly in-situ measurements of the vent flow rate and methane concentration reported to the United States Environmental Protection Agency (EPA) in 2017 put emissions from the San Juan vent at  $2585 \text{ kg h}^{-1}$  averaged over the year (EPA, 2017), in remarkable agreement with our estimate. Ong et al. (2017) approximated emissions of 10,800–12,600  $\text{kg h}^{-1}$  from the Appin mine, based on estimates of the vent flow rate and air stream methane concentration. Cardno (2009) used coal production activity data and Australian National

Greenhouse Accounts (NGA) emission factors to estimate ventilation shaft methane emissions of  $\sim 5200 \text{ kg h}^{-1}$  for the Appin mine in a two longwall mining formation. We are aware of only one emission estimate for the Bulianta mine:  $170 \text{ kg h}^{-1}$ , reported by the Chinese State Administration for Coal Mine Safety (SACMS). This estimate is based on ground measurements made during a 2–3 month safety evaluation performed in 2011 and is much lower than our result. Emissions from coal mine vents have large temporal variability, as shown by the Frankenberg et al. (2016) observations for San Juan, and satellite observations have unique value in providing long-term averages.

In summary, our results demonstrate the capability of space-based observations of methane plumes to quantify point source rates from high-emitting facilities under apparently normal operating conditions. The GHGSat-D demonstration satellite instrument used in our work has fine spatial resolution (50-m) but coarse single-pass column retrieval precision (9–19%) and large retrieval artefacts. Nevertheless, we were able to quantify time-averaged methane emissions from large coal mine vents ( $> 1000 \text{ kg h}^{-1}$ ) with  $\sim 40\%$  uncertainty. This involved averaging 13–24 observations per target over a 2-year period, using an optimized wind rotation procedure. Our time-averaged result for the San Juan coal mine vent was in close agreement with the annual emission reported to the U.S. EPA. Future methane-observing satellite instruments with similar spatial resolution but improved precision, including GHGSat-C1 to be launched in 2020 (Jervis et al., 2019) and the next generation of orbiting hyperspectral surface imagers (Cusworth et al., 2019), will likely improve our ability to detect methane plumes from individual facilities and infer source rates. Quantifying sources down to  $100 \text{ kg h}^{-1}$  would account for more than 90% of emissions from point sources in the U.S. GHGRP (Jacob et al., 2016). Such thresholds for detection and quantification will continue to shrink as revisit rates for time-averaging increase with the number of instruments in orbit. In view of the large temporal variability of emissions from individual facilities, repeated measurements from satellites may be particularly useful for estimating annual emissions for facility-level reporting purposes.

**Table 3.1:** Methane source rates from coal mine vents retrieved with GHGSat-D.

Coal mine	San Juan	Appin	Bulianta
<i>Location</i>			
Country	United States	Australia	China
State/Region	New Mexico	New South Wales	Inner Mongolia
Latitude	36.7928°N	34.1815°S	39.3835°N
Longitude	108.3890°W	150.7197°E	110.0951°E
<i>Source rate retrieval metadata</i>			
Averaging period	Aug 2016 – Nov 2018	Nov 2016 – Oct 2018	Aug 2016 – Dec 2018
Number of clear-sky observations	24	13	14
Single-pass error level	9%	19%	12%
10-m wind speed ( $\text{m s}^{-1}$ ) <sup>a</sup>	3.0 (0.5, 8.0)	2.2 (0.7, 3.8)	3.6 (0.9, 9)
<i>Source rate estimates (<math>\text{kg h}^{-1}</math>)<sup>b</sup></i>			
IME method	$2300 \pm 1020$	$5690 \pm 2540$	$2600 \pm 1010$
CSF method	$2150 \pm 980$	$5030 \pm 2100$	$2410 \pm 970$
Previous estimates	$360\text{--}2800^{\text{c}}$ , $2585^{\text{d}}$ , $1446^{\text{e}}$	$5200^{\text{f}}$ , $10800\text{--}12600^{\text{g}}$	$170^{\text{h}}$

<sup>a</sup> Mean (minimum, maximum) hourly wind speed for the ensemble of observations, obtained from the GEOS-FP database.

<sup>b</sup> The reported source rates are for time-averaged plumes after wind direction optimization (Figure 3.4), and using either the integrated mass enhancement (IME) or cross-sectional flux (CSF) method.

<sup>c</sup> Range from several days of aircraft remote sensing measurements in April 2015 (Frankenberg et al., 2016).

<sup>d</sup> Annual mean estimate for 2017 from quarterly in-situ measurements of flow rate and methane concentration (EPA, 2017).

<sup>e</sup> Mean estimate from five days of in-situ aircraft mass balance measurements (Smith et al., 2017).

<sup>f</sup> Estimate based on annual coal production activity data and emission factors (Cardno, 2009; converted from  $\text{kt CO}_2\text{e a}^{-1}$ ).

<sup>g</sup> Estimate based on ventilation flow rate and air stream methane concentration from vent design (Ong et al., 2017).

<sup>h</sup> Estimate from in-situ measurements during a weeks-long safety evaluation in 2011 (SACMS, 2011).

## ACKNOWLEDGEMENTS

We thank O. B. A. Durak and J. J. Sloan for their roles in developing the GHGSat retrievals algorithm and measurement concept. We thank C. Herzog, M. Arias, K. Wisniewski, M. Latulippe, N. Brown, and J. Thompson for technical assistance and preparation of the GHGSat-D methane data. We also thank J. D. Maasakers for helpful discussion. D. J. J. was supported by the Carbon Monitoring System of the NASA Earth Science Division.

# A

## Supplemental Information for Chapter 2

This appendix contains five supplemental figures, one supplemental table, and five supplemental text sections for Chapter 2. Figure A.1 shows the pipeline associated with source #2 under construction in 2004. Figure A.2 plots the effective wind speed functions inferred from large eddy simulations (LES) and used to estimate source rates from GHGSat-D plume observations. Figure A.3 shows source rates retrieved by the IME and CSF methods from GHGSat-D plume observations. Figure A.4 shows a full GHGSat-D methane retrieval field from January 2019 over Korpezhe. Fig-

ure A.5 supports our description of GHGSat-D column retrieval errors. Table A.1 contains detailed information on GHGSat-D retrieved source rates and errors for individual plumes, as well as the corresponding GEOS-FP 10-m wind speeds. The supplemental text sections provide additional information on our GHGSat-D measurements and retrievals, source rate quantification methods, and error analysis.

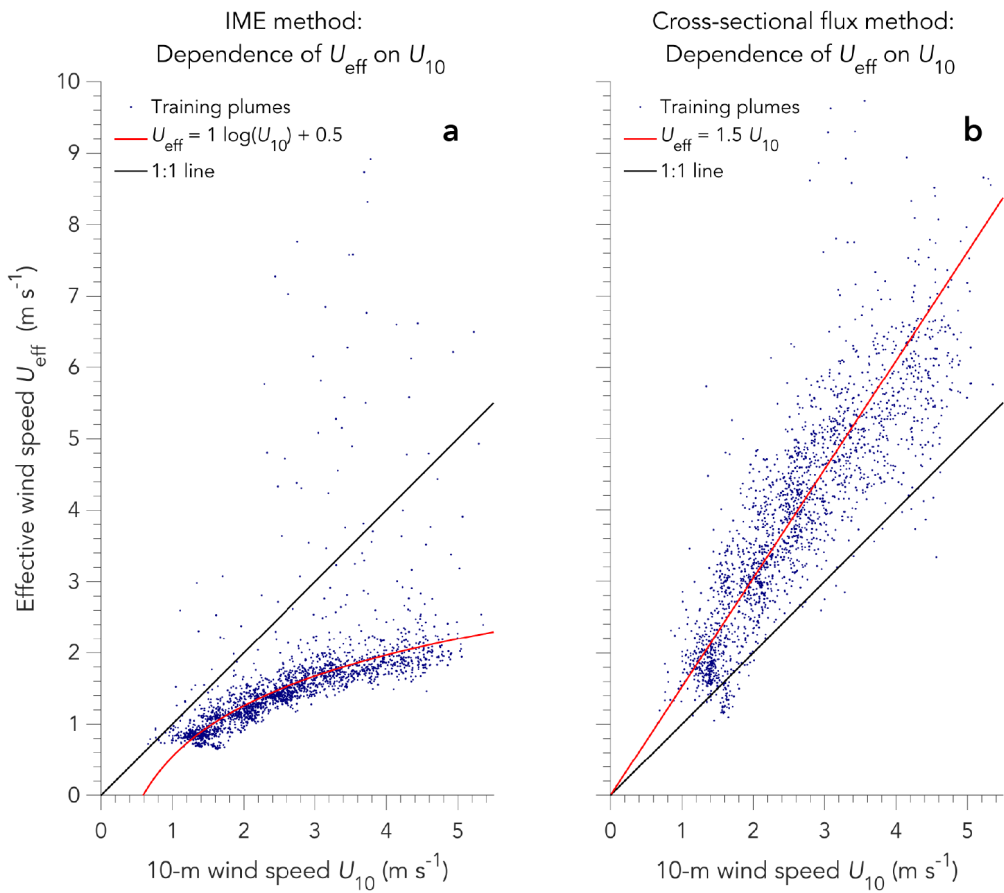
**Table A.1:** GHGSat-D source rate and wind speed summary data. Observation dates, source rates, and GEOS-FP 10-m wind speeds for individual plumes detected by GHGSat-D are listed. Source rates and error standard deviations are inferred as the mean result of the IME and CSF methods for each plume. Only the IME method was used for the 8 November 2018 plume, because the CSF method can be unreliable for 10-m winds below  $2 \text{ m s}^{-1}$  (Varon et al., 2018).

Figure 2.1 Panel	Source ID#	Date	Estimated source rate ( $\text{t h}^{-1}$ )	GEOS-FP $U_{10}$ ( $\text{m s}^{-1}$ )
a	1	19-Jun-2018	$11.6 \pm 8.8$	2.47
b	1	15-Aug-2018	$9.9 \pm 6.8$	4.24
c	1	03-Sep-2018	$43.3 \pm 12.0$	7.31
d	1	22-Sep-2018	$33.4 \pm 16.0$	3.82
e	1	08-Nov-2018	$35.7 \pm 23.6$	1.87
g	1	13-Jan-2019	$21.2 \pm 14.3$	2.49
g	2	13-Jan-2019	$32.0 \pm 21.0$	2.49
f	1	27-Jan-2019	$36.7 \pm 19.6$	3.22
h	3	27-Jan-2019	$3.6 \pm 3.2$	3.22



Background satellite image ©2019 DigitalGlobe, a Maxar company

**Figure A.1:** DigitalGlobe imagery of the pipeline connection near source #2 under construction in 2004. The white star marks the approximate location of source #2.



**Figure A.2:** Effective wind speed dependence on 10-m wind speed in the (a) IME and (b) CSF methods, assuming 16% measurement precision on retrieved methane columns. These models are trained on synthetic plume observations generated by large eddy simulation (LES).

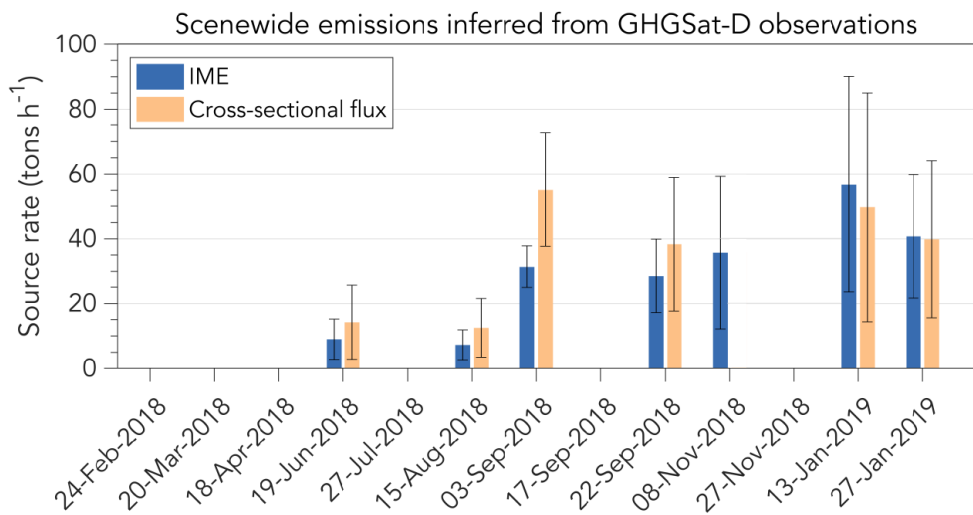


**Figure A.3:** Summary of GHGSat-D source rate retrievals by date and method showing source rates inferred from GHGSat-D plume observations using the IME and CSF methods. GHGSat-D source rates for observations with multiple detected plumes (13 and 27 January 2019) describe the total emissions for all detected plumes in the scene. The CSF method is not used for the plume observed on 8 November 2018, because that method is unreliable for 10-m winds below  $2 \text{ m s}^{-1}$  (Varon et al., 2018; see Figure 2.1 and Table A.1).

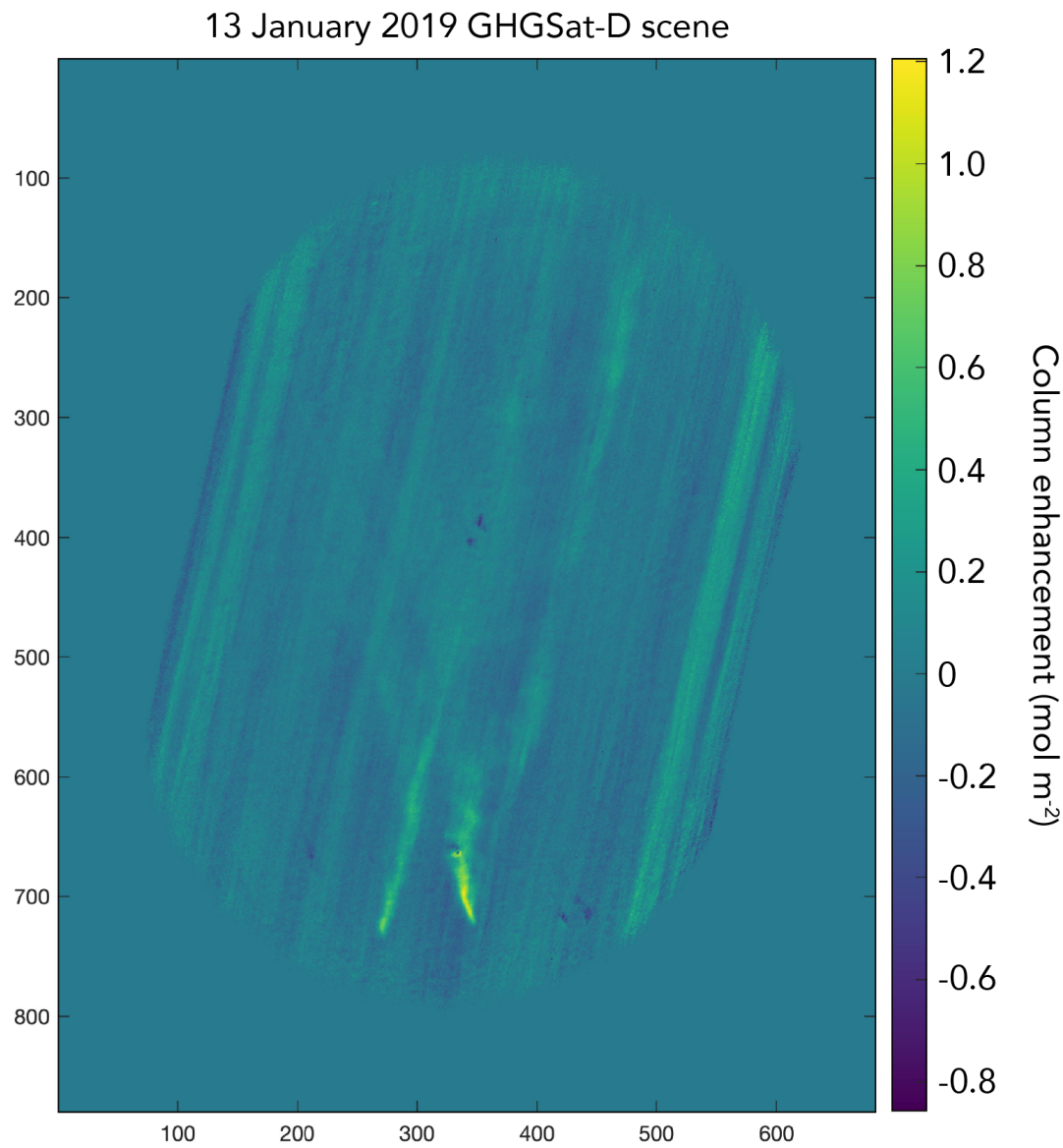


**Figure A.4:** Full methane column retrieval field for 13 January 2019 GHGSat-D observation of sources #1 and #2 in the Korpezhe oil/gas field.

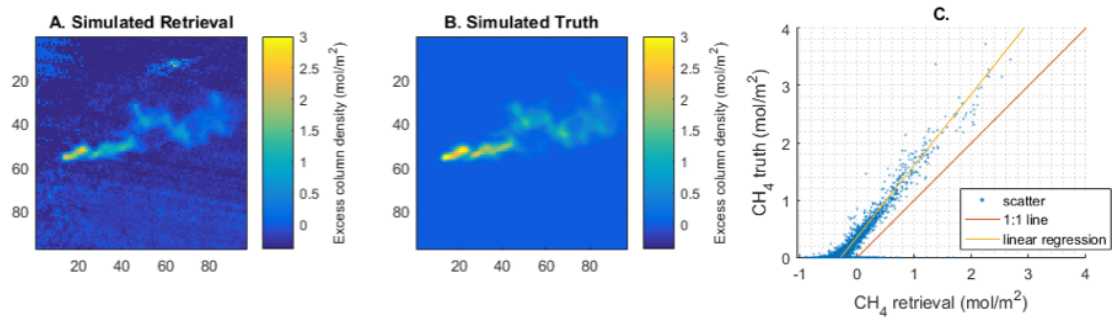


**Figure A.5:** Results from OSSEs where instrument imperfections are included in generating the simulated image sequence (see Section A.1). The retrieved values for one such simulation (panel A) are then compared to the input “truth” field (panel B) to obtain the correction factor 1.25 (slope of regression line in panel C).

## A.1 GHGSAT MEASUREMENTS AND RETRIEVALS

For the latitude of the Korpezhe gas field ( $38.5^\circ$ ), the GHGSat-D satellite has a revisit rate of 26 overpasses per year under normal operating conditions, and up to 52 overpasses per year when constraints on satellite observation angle are modestly relaxed. Since launch in June 2016, 58% of GHGSat-D observations have been successful, 26% have been unsuccessful due to clouds, and 16% have been unsuccessful due to operational constraints or errors. The high success rate is achieved by screening observations based on weather forecast (with respect to clouds).

The GHGSat measurement concept uses a wide-angle imaging Fabry-Perot spectrometer in which spectral information is superimposed onto a 2D image of the ground. The camera signal  $F_{(i,j)}$  at camera pixel  $(i,j)$  in units of electrical charge is given by:

$$F_{i,j}(\mathbf{x}) = \int L(\mathbf{x}, \lambda) \cdot C(\lambda) \cdot QE(\lambda) \cdot T_{\text{OSF}}(\lambda) \cdot T_{\text{FP}}(\theta_{i,j}, \lambda) d\lambda, \quad (\text{A.1})$$

where  $L(\mathbf{x}, \lambda)$  is the spectral radiance as a function of the state parameter vector  $\mathbf{x}$  and wavelength  $\lambda$ ,  $C(\lambda)$  is the radiometric conversion factor that converts spectral radiance to the number of photons on a camera pixel,  $QE(\lambda)$  is the quantum efficiency with which the camera converts photons to electric charge,  $T_{\text{OSF}}(\lambda)$  is the order-sorting filter that transmits light within our desired spectral bandpass, and the Fabry-Perot transmission function is given by:

$$T_{\text{FP}}(\theta_{i,j}, \lambda) = \frac{1}{1 + \left(\frac{2\mathcal{F}}{\pi}\right)^2 \left(\frac{2\pi n d \cos(\theta_{i,j})}{\lambda}\right)^2}, \quad (\text{A.2})$$

where  $\mathcal{F}$  is the total finesse,  $d$  is the distance between the inner surfaces of the F-P,  $n$  is the index of refraction of the medium between the inner F-P surfaces (taken to be equal to 1 on-orbit), and  $\theta_{(i,j)}$  is the incident angle of light with respect to the F-P surface normal vector.

The spectral radiance is calculated from the spectral irradiance  $I(\lambda)$ :

$$L(\mathbf{x}, \lambda) = \frac{\alpha(\lambda) \cos(\theta_{\text{sza}})}{\pi R_{E-S}^2} I(\mathbf{x}', \lambda), \quad (\text{A.3})$$

where  $\alpha(\lambda)$  is the spectrally-dependent surface albedo,  $\theta_{\text{sza}}$  is the solar zenith angle,  $R_{E-S}$  is the relative Earth-Sun distance,  $\mathbf{x}'$  is the state parameter vector (including methane, carbon dioxide, and water vapor) without the albedo, and the spectral irradiance is the solution to a simplified radiative transfer equation where thermal emission, aerosol and molecular scattering have been neglected:

$$\mu \frac{\partial I(\mathbf{x}', \lambda)}{\partial z} = -\alpha_{\text{abs}} I(\mathbf{x}', \lambda), \quad (\text{A.4})$$

where  $\mu = \cos(\theta)$  and  $\theta$  is the angle that the light travels through the atmosphere with respect to the Earth's surface normal,  $z$  is the altitude,  $\alpha_{\text{abs}}$  is the pressure, temperature, wavelength, and species dependent absorption coefficient calculated using the HITRAN API (Kochanov et al., 2016), and the solar spectrum is introduced through a boundary condition and generated from the AER solar irradiance model (AER, 2017). We integrate the radiative transfer equation discretely assuming 100 atmospheric layers that are evenly spaced in pressure.

The GHGSat instrument operates in “target” mode, in which the satellite attitude is controlled to keep the target in the field-of-view for much longer than it would be if the instrument were operated in nadir (downward pointing) mode, thereby increasing the signal-to-noise ratio (SNR)<sup>\*</sup>. Multiple 2D images are taken during each observation sequence such that the ground target traverses the field-of-view and samples the full extent of the spectroscopic information contained in the image. We use the term “ground pixel” (as opposed to camera pixel) to refer to a position in the ground-based coordinate system. The location of each ground pixel is tracked in every frame us-

---

<sup>\*</sup>SNR—where the noise is random, temporal, and uncorrelated across camera pixels—is a commonly-used metric in imaging spectrometry. It is less useful for GHGSat-D because (a) the instrument and retrievals concept differ greatly from typical grating-based systems and (b) GHGSat-D retrievals are limited by systematic errors from instrument imperfections, which are not included in the usual SNR.

ing a co-registration algorithm with a common coordinate system  $(i_r, j_r)$  taken from a reference frame  $r$ . Therefore, if we have  $k$  image frames, we can compare the observation data vector  $\mathbf{y}^{(i_r, j_r)} = \{\mathbf{y}_{i_1, j_1}^{(i_r, j_r)}, \mathbf{y}_{i_2, j_2}^{(i_r, j_r)}, \dots, \mathbf{y}_{i_k, j_k}^{(i_r, j_r)}\}$  to the forward model vector  $\mathbf{F}(\mathbf{x}_{i_r, j_r}) = \{F_{i_1, j_1}(\mathbf{x}_{i_r, j_r}), F_{i_2, j_2}(\mathbf{x}_{i_r, j_r}), \dots, F_{i_k, j_k}(\mathbf{x}_{i_r, j_r})\}$  in order to infer the state vector  $\mathbf{x}_{i_r, j_r}$  using a variant of standard inverse methods.

We use optimal estimation (Rodgers, 2000) to infer the posterior distribution of the state vector given the observation data, an error model, and a prior distribution for the state vector. Assuming a Gaussian form for the data and prior probability density functions, maximizing the joint probability density function amounts to minimizing the cost function

$$\chi^2(\mathbf{x}) = (\mathbf{y} - \mathbf{F}(\mathbf{x}))^T \mathbf{S}_o^{-1} (\mathbf{y} - \mathbf{F}(\mathbf{x})) + (\mathbf{x} - \mathbf{x}_a)^T \mathbf{S}_a^{-1} (\mathbf{x} - \mathbf{x}_a), \quad (\text{A.5})$$

where  $\mathbf{S}_o$  is the observation error covariance matrix,  $\mathbf{S}_a$  is the prior covariance matrix, and  $\mathbf{x}_a$  is the prior state vector that uses same-scene information from Landsat-8 for the albedo parameter (Roy et al., 2014), closest-in-time methane concentration values from TROPOMI (Hu et al., 2018), and carbon dioxide and water concentration values from AIRS (Razavi et al., 2009; Tobin et al., 2006). The Gauss-Newton procedure for minimizing the cost function requires that we update the state vector at each iteration by a step:

$$\Delta \mathbf{x}^{i+1} = (\mathbf{K}^T(\mathbf{x}^i) \mathbf{S}_o^{-1} \mathbf{K}(\mathbf{x}^i) + \mathbf{S}_a^{-1})^{-1} (\mathbf{K}^T(\mathbf{x}^i) \mathbf{S}_o^{-1} (\mathbf{y} - \mathbf{F}(\mathbf{x}^i)) + \mathbf{S}_a^{-1} (\mathbf{x} - \mathbf{x}_a)), \quad (\text{A.6})$$

where  $\mathbf{K}(\mathbf{x}^i) = \frac{d\mathbf{F}(\mathbf{x}^i)}{d\mathbf{x}^i}$  is the Jacobian of the forward model evaluated at  $\mathbf{x}^i$ .

At each iteration of the Gauss-Newton procedure, the forward model and Jacobians must be evaluated. This is computationally expensive and infeasible for the 200,000 ground pixel retrievals we perform in our field-of-view. Instead, we employ a strategy in which the retrievals are split into two steps: (1) a scene-wide average retrieval using the full forward model to estimate the scene-wide

average state vector  $\mathbf{x}$ , and (2) a per-pixel retrieval done using a linearized forward model (LFM) evaluated at the linearization point  $\mathbf{x}$ . The scene-wide average defines the background methane column for the scene, and the enhancement above background for each pixel is relative to that average. The methane plumes manifest as large coherent enhancements (for the 95th percentile and above) that coincide with facility locations (see Figure A.4 and main text).

The primary advantage of using the LFM is that we only have to compute the forward model and Jacobians once at the beginning of the per-pixel retrieval. A disadvantage is that for the parameters that are nonlinear in the forward model, a retrieval using the LFM will introduce systematic biases for deviations far from the linearization point. For the particular case of molecular column density enhancements, this leads to an underestimation that is corrected in post-processing.

The output of this per-pixel retrieval step is a spatially-resolved array of retrieved values for each state vector element. We refer to these arrays as retrieval fields. Portions of the methane column retrieval fields for the Korpezhe observations are shown after thresholding in Figure 2.1, and a complete field is shown in Figure A.4. The 16% column density precision of GHGSat-D for the scenes presented here includes contributions from both normally distributed noise (e.g., from photon shot noise, camera dark current and readout noise) and spatially correlated errors that result from various instrument imperfections (e.g., out-of-field stray light, unwanted reflections within the instrument, and memory lag effects in the camera). The spatially correlated errors ultimately set the detection limit of GHGSat-D, since they are difficult to distinguish from genuine methane enhancements caused by emission plumes in the retrieved column density field. The 16% quoted precision should therefore be regarded as a representative, though imperfect, measure of the instrument performance for the reported set of Korpezhe observations. This precision value is computed as a standard deviation over all non-plume pixels in the scene (i.e., over all background pixels). Plume pixels are pixels within a plume mask, which is constructed by thresholding and smoothing as described in Section A.3. We report 16% precision as the average value of this standard deviation computed for all scenes.

Aside from this precision of 16%, there is also the question of the overall multiplicative scaling of the retrieved columns. Although the GHGSat retrievals tools are built on a detailed model of the radiative transfer and the imaging spectrometer, there are still inaccuracies and unmodeled effects in the forward model. We have performed a series of observation system simulation experiments (OSSEs) of these Korphezhe observation events where various imperfections are included in the simulated image sequences, but either omitted or imperfectly modeled in the retrievals (Figure A.5). Specifically, these simulated effects include stray light, modelling errors associated with the Fabry-Perot and order-sorting filter, systematics related to the plume position within the retrieval domain, motion blur, and errors from co-registration and imperfect sampling. The detailed characteristics of these simulated imperfections are based on knowledge of the instrument properties from extensive pre-launch ground testing and careful analysis of on-orbit data. The simulated image sequences are generated using a reflectance map of the Korpezhe area derived from LandSat-8 imagery (band 6). We use the Varon et al. (2018) large eddy simulation (LES) ensemble to generate the input column density field (a plume from a point-like emitter with magnitude comparable to those in Figure 2.1).

The retrievals on these simulated image sequences are performed with the same software used for the satellite observations, configured the same way. This procedure yields simulated retrieval fields as shown in Figure A.5 (panel A) and a series of these OSSEs are performed for a range of parameter values corresponding to our uncertainty in the true values. Looking at the variation in regression slopes (e.g., Figure A.5, panel C), we find that the methane retrieval has a systematic scaling error such that the columns are underestimated by a factor  $1.25 \pm 0.07$ . This bias has two primary sources: stray light and uncertainty in the Fabry-Perot parameters. Stray light could lead to an apparently reduced absorption contrast, which would explain the general underestimation. As a result of our analysis, all GHGSat column density values reported in this manuscript have been scaled up by 25%, and the uncertainty in this scaling factor is included in the overall column density error analysis discussed in Section A.4 below.

## A.2 QUANTIFYING TROPOMI PLUMES

For methane plumes observed by TROPOMI, we quantify emissions using the CSF method. We consider only high-quality observations with low aerosol concentrations and cloud-free conditions (Hu et al., 2018). We use up to 15 transects between the source and the end of the plume, where concentrations are below the background concentration upwind. We ignore the first three transects because of their proximity to the source, where enhancements may be underestimated (Pandey et al., 2018). We only consider downwind transects that have more than 75% overlap with TROPOMI methane columns. The background is calculated from a transect  $0.1^\circ$  upwind of the source.

To account for background emissions, we include bottom-up emissions for all nearby oil/gas infrastructure from Scarpelli et al. (2020) in our WRF-Chem simulations for the January scenes. For each January simulation, we subtract from our emission estimate for the day all emissions picked up by the CSF method but associated with the background sources. For non-January days, we subtract  $3.1 \text{ t h}^{-1}$ , the average value of background emissions estimated from the January simulations. The Scarpelli et al. emissions are based on infrastructure information for 2012 and assume normal working conditions, so they may underestimate background emissions. Other extreme sources such as the ones observed by GHGSat-D may occur outside of the GHGSat-D domain and contribute to the emissions estimated by TROPOMI.

We only report source rates for plumes with at least three transects and for which the difference in wind direction between the boundary layer GEOS-FP wind and any of the wind ensemble members discussed in Section A.5 below is less than  $90^\circ$ . This discards scenes with rotating winds, where the CSF method is unsuitable for quantifying plumes, and results in a total of 24 quantifiable plumes (Figure 2.4).

To estimate emissions for the full 128 days of TROPOMI methane retrievals over the source area ( $E_{\text{all days}}$ , equation A.7), for each TROPOMI scene we compare the maximum column con-

centration observed by TROPOMI over the GHGSat-D domain to the background, which can be calculated for 127 scenes. For these 127 scenes, we multiply the maximum methane enhancement by the effective wind speed for that day, and find an average ratio of 0.75 between this quantity ( $\Delta$ ) evaluated for all scenes and for only the 24 scenes quantified using the CSF method. We therefore estimate mean emissions over the full observation record as 75% of the mean emissions for quantified plumes ( $E_{\text{CSF days}}$ ):

$$E_{\text{all days}} = \frac{\Delta_{\text{all days}}}{\Delta_{\text{CSF days}}} E_{\text{CSF days}} = 0.75 E_{\text{CSF days}} \quad (\text{A.7})$$

### A.3 PLUME MASK FOR GHGSAT-D PLUME QUANTIFICATION

In the IME and CSF methods, a Boolean plume mask distinguishes plume pixels from background pixels. For plumes detected by GHGSat-D, we first define this mask by a threshold applied to the methane columns at the 95th percentile (see Figure 2.1), and then smooth the mask with median and Gaussian filters to delete random classification errors and avoid loss of plume mass at the mask edges. The median filter replaces each mask element with the median of its  $150 \times 150 \text{ m}^2$  neighborhood ( $3 \times 3$  pixels at 50 m resolution). The Gaussian filter convolves the mask array with a Gaussian kernel of standard deviation 50 m, producing a continuous-valued array in the unit interval [0, 1]. Finally, we apply a threshold  $T = 0.2$  to the filtered mask array to obtain a smoothed Boolean mask.

Note that it is desirable but not essential to reduce the amount of plume mass lost at the mask edges. This is because while reducing lost plume mass can increase signal-to-noise in the plume, the same plume masking approach is applied to our LES plume ensemble when calibrating the effective wind speed functions used to calculate source rates. The effect of lost mass is therefore accounted for in our source rate retrievals.

#### A.4 GHGSAT-D SOURCE RATE ERROR ANALYSIS

We include four sources of error in our emission estimates: (1) error in wind speed, (2) error in the retrieved methane enhancements, (3) error in the IME and CSF models, and (4) error in pixel resolution. We add these errors in quadrature to estimate the total uncertainty in our retrieved source rates, which ranges from 30–90% for the plumes presented here.

(1) Wind speed error arises from using a coarse resolution meteorological database to estimate the local 10-m wind speed  $U_{10}$ . It tends to dominate the overall uncertainty in retrieved source rates. Error in  $U_{10}$  propagates through the effective wind speed function  $U_{\text{eff}} = f(U_{10})$  to affect the retrieved source rate. The resulting source rate uncertainty depends primarily on the magnitude of  $U_{10}$  and which of the IME or CSF methods is used (Varon et al., 2018). For fine-scale column observations of methane plumes with source rates  $0.05 - 2.25 \text{ tons h}^{-1}$  and 10-m wind speeds  $2 - 7 \text{ m s}^{-1}$ , Varon et al. (2018) found relative error standard deviations of 15–50% on source rates retrieved by the IME method and 30–65% by the CSF method (where larger errors correspond to smaller wind speeds) based on a comparison of GEOS-FP modeled 3-hour winds with wind measurements from U.S. airports in the University of Utah MesoWest database (Horel et al., 2002). Specifically, Varon et al. (2018) considered one month of daytime (15:00–21:00 UTC) wind measurements taken at 10 U.S. airports (ABQ, ATL, BOS, DFW, LAX, MCI, MSP, PDX, PHL, and PHX) during June 2017. Repeating this analysis with source rates  $4 - 40 \text{ tons h}^{-1}$ , the  $U_{\text{eff}} = f(U_{10})$  relationships derived for this work (Figure A.2), and GEOS-FP 1-hour winds, we find source rate errors of 10–65% for the IME method and 20–80% for the CSF method over the  $1.5 - 7.5 \text{ m s}^{-1}$   $U_{10}$  range. This may underestimate the true error in GEOS-FP modeled wind speeds for the Korpezhe region, where the reanalysis is less constrained than for the comparatively data-rich United States.

(2) Error in the GHGSat-D methane column enhancements is driven by (a) correlated random errors in the retrieved column densities, (b) our ability to define the background column, and (c)

systematic scaling error of 7% (see Section A.1). To quantify the effects of (a) and (b) on the source rate retrieval for a particular plume observation, we move the plume mask to an ensemble of non-plume locations across the imaging domain. This gives the relative statistics of spatially correlated errors aggregated over the plume mask (for the IME method) or over plume transects (for the CSF method), from which we can infer error distributions for our source rate estimates. Specifically, we subtract the distribution mean to correct for residual scene-wide bias in the column retrieval (see Section A.1), and use the distribution standard deviation to define the uncertainty in the plume's aggregated enhancement (IME or CSF). This uncertainty ranges from 6% to 50%, with larger error for smaller plumes. The source rate error due to (b) arises from uncertainty in the subtracted mean. Here we make the conservative estimate that this additional uncertainty is also equal to the standard deviation of the error distribution (6%–50%), which assumes no uncertainty reduction in the subtracted mean based on the number of independent (non-plume) mask samples. The total error from (a) and (b) then ranges from 8–71%. Finally, to address the effect of (c) on the source rate retrieval, we add an additional 7% error that, unlike the other errors discussed here, applies equally across all observations (i.e., the scaling error would scale all plumes the same way).

(3) Error in the IME and CSF models stems from the difficulty of mapping  $U_{10}$  to  $U_{\text{eff}}$  for plumes of varying shapes and sizes in different meteorological conditions. Figure A.2 shows  $U_{\text{eff}} = f(U_{10})$  mappings for the IME and CSF methods, derived from LES experiments with 16% measurement noise. The fit residuals on average imply source rate errors of 7% for the IME method and 8% for the CSF method. We may underestimate these errors because our LES analysis does not incorporate spatially correlated noise and is not customized to the exact meteorological and topographic conditions of the Korpezhe oil/gas field. The ensemble is for flat terrain, with a  $100 \text{ W m}^{-2}$  sensible heat flux, and covers a range of initial wind speeds ( $2\text{--}8 \text{ m s}^{-1}$ ) and boundary layer depths (800–1500 m). It is intended for wide application to different measurement sites, assuming that the range of simulated meteorological conditions is adequately representative of the true conditions. In this

case, our LES ensemble is broadly consistent with the range of GEOS-FP wind speeds reported for Korpezhe on GHGSat-D observation, and the oil/gas field is relatively flat.

(4) GHGSat pixel resolution for the Korpezhe scenes examined here varies by about 1% between observations, due to differences in viewing angle (ranging from  $0.3^\circ$  to  $6.6^\circ$ ) and instrument altitude (498.4–510.8 km) on different overpasses. The satellite-target distance and viewing angle are well-known from GPS telemetry, but georeferencing imperfections may lead to uncertainty in the pixel resolution for specific observations, and resulting source rate uncertainty of 0.25% for the IME method and 0.35% for the CSF method. This error is small relative to other sources of uncertainty and our total estimated errors of 30–90%, but we include it in the error budget nonetheless.

Our error estimates for mean, total, and annual emissions (upscaled from individual days) do not include uncertainty from unsampled temporal variability of sources, as this variability cannot be determined. As discussed in Section 2.5, we translate our instantaneous emission estimates to total and annual emissions by multiplying mean hourly source rate (including non-detections) by duration (e.g.,  $17.5 \pm 4.2 \text{ t h}^{-1}$  multiplied by 11 months for the total emissions over GHGSat-D observation period). We derive errors on the mean source rate by propagating the error standard deviation of source rates for individual plumes (Figure 2.1 and Table A.1) through the calculation of the mean rate. For  $n$  independent estimates of source rate with error variances  $\sigma_i^2, i = 1 \dots n$ , the error variance of the mean source rate is given by

$$\sigma^2 = \frac{\sum_i \sigma_i^2}{n^2}, \quad (\text{A.8})$$

and the corresponding error standard deviation is given by the square root of this expression. The errors on total/annual emissions are obtained by multiplying the error in the mean rate by duration. This approach relies on the assumption that our observations are a representative sample of the sites' emissions over the observation period.

Finally, as discussed in Section A.1, it is possible for artifacts in the retrieval field to be mistaken for plumes. However, our prior information on the local infrastructure from DigitalGlobe imagery would help prevent such false positives. The plumes in Figures 2.1b, 2.1d, and 2.1h show discontinuities after thresholding. This may be due to plume enhancement variations caused by turbulence, or to plume overlap with retrieval errors. The break in the plume from source #3 (Figure 2.1h) could imply the existence of another nearby source, but we were unable to associate the second downwind plume segment with any facility in the land imagery. Since we observe source #1 on multiple occasions, the plume discontinuities in Figures 2.1b and 2.1d are unlikely to be explained by the existence of additional nearby sources.

## A.5 TROPOMI SOURCE RATE ERROR ANALYSIS

To estimate uncertainty in the emissions derived from TROPOMI observations, we construct a seven-member ensemble of emission retrievals: (1) using the 10-m GEOS-FP wind; (2) using the 10-m ECMWF ERA5 wind (C3S, 2019); (3) using the 10-m ECMWF ERA-Interim wind (Dee et al., 2011), (4) using the GEOS-FP boundary layer wind sampled  $0.5^\circ$  downwind of the source; (5) using the GEOS-FP 10-m wind sampled  $0.5^\circ$  downwind of the source; (6) sampling transects at every  $0.05^\circ$  and offset by  $0.025^\circ$  downwind instead of every  $0.02^\circ$  without offset; and (7) using a background defined  $0.2^\circ$  upwind instead of  $0.1^\circ$  upwind. For each observation, we only consider ensemble members that give valid (non-negative before the subtraction of background emissions, with a well-defined background) emission quantifications. All wind datasets are scaled such that their average magnitude across all scenes matches the average magnitude of GEOS-FP boundary layer winds for the period, so that the same effective wind speed relationship (derived for the GEOS-FP boundary layer wind) can be used in every quantification. In addition to this ensemble, for each observation we also consider the standard deviation of the plume transects used and a base error

level representing uncertainty in the retrieved columns. This base error is calculated by reducing and increasing the background used in the CSF method by 6.5 ppb, which is the average standard deviation of methane columns retrieved between 38–39°N and 55–56°E, an area where we only expect small emissions. For some plume observations, these considerations extend the uncertainty range beyond that of the seven-member source rate retrieval ensemble.

# B

## Supplemental Information for Chapter 3

### B.1 SOURCE RATE RETRIEVAL ERROR ANALYSIS

We consider three types of error affecting the emission retrieval: wind speed error, error in the IME and CSF models (including wind direction error and error in the effective wind speed fit), and error in the retrieved columns. We add these errors in quadrature to estimate the total error ( $1\sigma$ ) on our retrieved source rates.

We evaluate wind speed error by comparing GEOS-FP winds with U.S. airport measurements (Figure 3.2). We find an error standard deviation of  $\sim 2.5 \text{ m s}^{-1}$  when using 1-hour GEOS-FP data to estimate local 5-minute wind speeds, and scale this by  $1/\sqrt{N}$  to reflect reduced error in the average wind speed across  $N$  observations. Propagating this error through the LES-derived  $U_{\text{eff}} = f(U_{10})$  relationships shown in Figure 3.3 provides an estimate of the source rate retrieval error caused by uncertainty in the effective wind speed. We find errors of 17–30% in both the IME and CSF methods, with larger errors for slower winds and when fewer observations are available.

Error in the IME and CSF models is estimated by evaluating the models on our test set of time-averaged LES plumes (without added synthetic measurement noise). The error amounts to 13–24% for the IME method and 16–18% for the CSF method, and includes effects from wind direction uncertainty and uncertainty in the effective wind speed functions (Figure 3.3). We may underestimate these sources of error, as our LES analysis does not incorporate local topography at the coal mines, and because we assess wind data quality by comparing with measurements made at airports in the United States, where meteorological reanalysis products are relatively well-constrained. Furthermore, the DarkSky weather API assimilates surface wind measurements including from airports, which would lead to overly optimistic estimates of its precision for estimating surface wind direction at arbitrary locations.

To estimate the error from measurement noise, we follow the approach of Varon et al. (2019) and move the plume mask to an ensemble of independent non-plume locations across the time-averaged scene. We obtain in this way a distribution of IME (and mean transect) values corresponding to retrieval errors alone. We subtract the distribution mean from the plume’s IME (and mean transect) before computing source rate, and use the distribution standard deviation as an estimate of the source rate error resulting from measurement noise. To account for uncertainty in the subtracted distribution mean, we add an additional error equal to the distribution standard deviation divided by the square root of the number of independent non-plume locations sampled. Finally, we include

7% uncertainty due to systematic scaling error in the retrieved columns, following the analysis presented in Varon et al. (2019). This results in source rate errors of 22–38% for the three coal mine vents in both the IME and CSF methods.

Adding all of these errors in quadrature, we find total source rate error standard deviations for the three coal mines of 39–45% in the IME method and 40–45% in the CSF method (Table 3.1).

# References

- [1] Alvarez, R. A., Zavala-Araiza, D., Lyon, D. R., Allen, D. T., Barkley, Z. R., Brandt, A. R., Davis, K. J., Herndon, S. C., Jacob, D. J., Karion, A., Kort, E. A., Lamb, B. K., Lauvaux, T., Maasakkers, J. D., Marchese, A. J., Omara, M., Pacala, S. W., Peischl, J., Robinson, A. L., Shepson, P. B., Sweeney, C., Townsend-Small, A., Wofsy, S. C., & Hamburg, S. P. (2018). Assessment of methane emissions from the U.S. oil and gas supply chain. *Science*, 361(6398), 186–188.
- [2] Atmospheric and Environmental Research (AER) (2017). Solar irradiance spectrum extract\_solar\_v1.4.4. Retrieved from [http://rtweb.aer.com/solar\\_frame.html](http://rtweb.aer.com/solar_frame.html) (last update August 2017).
- [3] Bovensmann, H., Buchwitz, M., Burrows, J. P., Reuter, M., Krings, T., Gerilowski, K., Schneising, O., Heymann, J., Tretner, A., & Erzinger, J. (2010). A remote sensing technique for global monitoring of power plant co<sub>2</sub> emissions from space and related applications. *Atmospheric Measurement Techniques*, 3(4), 781–811.
- [4] Bovensmann, H., Burrows, J. P., Buchwitz, M., Frerick, J., Noël, S., Rozanov, V. V., Chance, K. V., & Goede, A. P. H. (1999). SCIAMACHY: Mission objectives and measurement modes. *Journal of Atmospheric Science*, 56(2), 127–150.
- [5] Brakeboer, B. N. A. (2015). Development of the structural and thermal control subsystems for an earth observation microsatellite and its payload. Master's thesis, University of Toronto.
- [6] Brasseur, G. & Jacob, D. (2017). *Modeling of Atmospheric Chemistry*. Cambridge University Press.
- [7] Buchwitz, M., Schneising, O., Reuter, M., Heymann, J., Krautwurst, S., Bovensmann, H., Burrows, J. P., Boesch, H., Parker, R. J., Somkuti, P., Detmers, R. G., Hasekamp, O. P., Aben, I., Butz, A., Frankenberg, C., & Turner, A. J. (2017). Satellite-derived methane hotspot emission estimates using a fast data-driven method. *Atmospheric Chemistry and Physics*, 17(9), 5751–5774.
- [8] Butz, A., Guerlet, S., Hasekamp, O., Schepers, D., Galli, A., Aben, I., Frankenberg, C., Hartmann, J. M., Tran, H., Kuze, A., Keppel-Aleks, G., Toon, G., Wunch, D., Wennberg, P.,

- Deutscher, N., Griffith, D., Macatangay, R., Messerschmidt, J., Notholt, J., & Warneke, T. (2011). Toward accurate CO<sub>2</sub> and CH<sub>4</sub> observations from GOSAT. *Geophysical Research Letters*, 38(11), L14812.
- [9] Cambaliza, M. O. L., Shepson, P. B., Bogner, J., Caulton, D. R., Stirm, B., Sweeney, C., Montzka, S. A., Gurney, K. R., Spokas, K., Salmon, O. E., Lavoie, T. N. anf Hendricks, A., Mays, K., Turnbull, J., Miller, B. R., Lauvaux, T., Davis, K., Karion, A., Moser, B., Miller, C., Obermeyer, C., Whetstone, J., Prasad, K., Miles, N., & Richardson, S. (2015). Quantification and source apportionment of the methane emission flux from the city of Indianapolis. *Elementa: Science of the Anthropocene*, 3, 000037.
- [10] Cambaliza, M. O. L., Shepson, P. B., Caulton, D. R., Stirm, B., Samarov, D., Gurney, K. R., Turnbull, J., Davis, K. J., Possolo, A., Karion, A., Sweeney, C., Moser, B., Hendricks, A., Lauvaux, T., Mays, K., Whetstone, J., Huang, J., Razlivanov, I., Miles, N. L., & Richardson, S. J. (2014). Assessment of uncertainties of an aircraft-based mass balance approach for quantifying urban greenhouse gas emissions. *Atmospheric Chemistry and Physics*, 14(17), 9029–9050.
- [11] Cardno (2009). Environmental assessment appin colliery area 7 goaf gas drainage project. Retrieved from [https://www.south32.net/docs/default-source/illawarra-coal/bulli-seam-operations/appin/appin-surface-gasmanagement-project—enviro-asse/environmental-assessment-appin-surface-gas-managementproject.pdf?sfvrsn=321a9200\\_4](https://www.south32.net/docs/default-source/illawarra-coal/bulli-seam-operations/appin/appin-surface-gasmanagement-project—enviro-asse/environmental-assessment-appin-surface-gas-managementproject.pdf?sfvrsn=321a9200_4) (last access: 14 February 2020).
- [12] China State Administation of Coal Mine Safety (SACMS) (2011). Compilation of national coal mine gas level identficiation for 2011. (National Coal Mine Safety Supervision Bureau, 2019).
- [13] Clarisse, L., Van Damme, M., Clerbaux, C., & Coheur, P.-F. (2019). Tracking down global NH<sub>3</sub> point sources with wind-adjusted superresolution. *Atmospheric Measurement Techniques Discussions*.
- [14] Clerbaux, C., Boynard, A., Clarisse, L., George, M., Hadji-Lazaro, J., Herbin, H., Hurtmans, D., Pommier, M., Razavi, A., Turquety, S., Wespes, C., & Coheur, P.-F. (2009). Monitoring of atmospheric composition using the thermal infrared IASI/MetOp sounder. *Atmospheric Chemistry and Physics*, 9(16), 6041–6054.
- [15] Conley, S., Franco, G., Faloona, I., Blake, D. R., Peischl, J., & Ryerson, T. B. (2016). Methane emissions from the 2015 Aliso Canyon blowout in Los Angeles, CA. *Science*, 351(6279), 1317–1320.
- [16] Copernicus Climate Change Service (C3S) (2019). ERA5: Fifth generation of ECMWF atmospheric reanalyses of the global climate. (Copernicus Climate Change Service Climate Data Store (CDS), 2019). Retrieved from <https://cds.climate.copernicus.eu/cdsapp#!/home>.

- [17] Crisp, D., Pollock, H. R., Rosenberg, R., Chapsky, L., Lee, R. A. M., Oyafuso, F. A., Frankenberg, C., O'Dell, C. W., Bruegge, C. J., Doran, G. B., Eldering, A., Fisher, B. M., Fu, D., Gunson, M. R., Mandrake, L., Osterman, G. B., Schwandner, F. M., Sun, K., Taylor, T. E., Wennberg, P. O., & Wunch, D. (2017). The on-orbit performance of the Orbiting Carbon Observatory-2 (OCO-2) instrument and its radiometrically calibrated products. *Atmospheric Measurement Techniques*, 10(1), 59–81.
- [18] Cusworth, D. H., Jacob, D. J., Sheng, J. X., Benmergui, J., Turner, A. J., Brandman, J., White, L., & Randles, C. A. (2018). Detecting high-emitting methane sources in oil/gas fields using satellite observations. *Atmospheric Chemistry and Physics*, 18(23), 16885–16896.
- [19] Cusworth, D. H., Jacob, D. J., Varon, D. J., Chan Miller, C., Liu, X., Chance, K., Thorpe, A. K., Duren, R. M., Miller, C. E., Thompson, D. R., Frankenberg, C., Guanter, L., & Randles, C. (2019). Potential of next-generation imaging spectrometers to detect and quantify methane point sources from space. *Atmospheric Measurement Techniques*, 12(10), 5655–5668.
- [20] Dammers, E., McLinden, C. A., Griffin, D., Shephard, M. W., Van Der Graaf, S., Lutsch, E., Schaap, M., Gainairu-Matz, Y., Fioletov, V., Van Damme, M., Whitburn, S., Clarisse, L., Cady-Pereira, K., Clerbaux, C., Coheur, P.-F., & Erisman, J. W. (2019). NH<sub>3</sub> emissions from large point sources derived from CrIS and IASI satellite observations. *Atmospheric Chemistry and Physics*, 19(19), 12261–12293.
- [21] DarkSky (2019). DarkSky weather application programming interface (API). Available at <https://darksky.net/dev> (last access: 9 May 2019).
- [22] De Foy, B., Lu, Z., Streets, D. G., Lamsal, L. N., & Duncan, B. N. (2015). Estimates of power plant NOx emissions and lifetimes from OMI NO<sub>2</sub> satellite retrievals. *Atmospheric Environment*, 116, 1–11.
- [23] Dee, D. P., Uppala, S. M., Simmons, A. J., Berrisford, P., Poli, P., Kobayashi, S., Andrae, U., Balmaseda, M. A., Balsamo, G., Bauer, P., Bechtold, P., Beljaars, A. C. M., van de Berg, L., Bidlot, J., Bormann, N., Delsol, C., Dragani, R., Fuentes, M., Geer, A. J., Haimberger, L., Healy, S. B., Hersbach, H., Hólm, E. V., Isaksen, L., Källberg, P., Köhler, M., Matricardi, M., McNally, A. P., Monge-Sanz, B. M., Morcrette, J. J., Park, B. K., Peubey, C., de Rosnay, P., Tavolato, C., Thépaut, J. N., & Vitart, F. (2011). The ERA-Interim reanalysis: Configuration and performance of the data assimilation system. *Quarterly Journal of the Royal Meteorological Society*, 137(656), 553–597.
- [24] D'Isidoro, M., Maurizi, A., & Tampieri, F. (2010). Effects of resolution on the relative importance of numerical and physical horizontal diffusion in atmospheric composition modelling. *Atmospheric Chemistry and Physics*, 10(6), 2737–2743.

- [25] Drummond, J. R. (1992). Measurements of Pollution in the Troposphere (MOPITT). In *The Use of EOS for Studies of Atmospheric Physics*, edited by J. C. Gille and G. Visconti, pp. 77–101, North-Holland, New York.
- [26] Duren, R. M., Thorpe, A. K., Foster, K. T., Rafiq, T., Hopkins, F. M., Yadav, V., Bue, B. D., Thompson, D. R., Conley, S., Colombi, N. K., Frankenberg, C., McCubbin, I. B., Eastwood, M. L., Falk, M., Herner, J. D., Croes, B. E., Green, R. O., & Miller, C. E. (2019). California's methane superemitters. *Nature*, 575, 180–184.
- [27] Filetov, V. E., McLinden, C. A., Krotkov, N., & Li, C. (2015). Lifetimes and emissions of SO<sub>2</sub> from point sources estimated from OMI. *Geophysical Research Letters*, 42(6), 1969–1976.
- [28] Frankenberg, C., Meirink, J. F., van Weele, M., Platt, U., & Wagner, T. (2005). Assessing methane emissions from global space-borne observations. *Science*, 308(5724), 1010–1014.
- [29] Frankenberg, C., Thorpe, A. K., Thompson, D. R., Hulley, G., Kort, E. A., Vance, N., Borchart, J., Krings, T., Gerilowski, K., Sweeney, C., & Conley, S. (2016). Airborne methane remote measurements reveal heavy-tail flux distribution in Four Corners region. *Proceedings of the National Academy of Sciences of the United States of America*, 113(35), 9734–9739.
- [30] Germain, S., Durak, B., Gains, D., Jervis, D., McKeever, J., & Sloan, J. J. (2017). Quantifying industrial methane emissions from space with the GHGSat-D satellite. Abstract presented at the American Geophysical Union 2017 Fall Meeting, New Orleans, LA, 11–15 December 2017.
- [31] Global Modeling and Assimilation Office (GMAO) (2020). GEOS-FP. Available at <https://portal.nccs.nasa.gov/cgilats4d/opendap.cgi?&path=>, last access: 19 December 2018.
- [32] Gordon, I., Rothman, L., Hill, C., Kochanov, R., Tan, Y., Bernath, P., Birk, M., Boudon, V., Campargue, A., Chance, K., Drouin, B., Flaud, J.-M., Gamache, R., Hodges, J., Jacquemart, D., Perevalov, V., Perrin, A., Shine, K., Smith, M.-A., Tennyson, J., Toon, G., Tran, H., Tyuterev, V., Barbe, A., Császár, A., Devi, V., Furtenbacher, T., Harrison, J., Hartmann, J.-M., Jolly, A., Johnson, T., Karman, T., Kleiner, I., Kyuberis, A., Loos, J., Lyulin, O., Massie, S., Mikhailenko, S., Moazzen-Ahmadi, N., Müller, H., Naumenko, O., Nikitin, A., Polyansky, O., Rey, M., Rotger, M., Sharpe, S., Sungh, K., Starikova, E., Tashkun, S., Vander Auwera, J., Wagner, G., Wilzewski, J., Wcisło, P., Yu, S., & Zak, E. (2017). The HITRAN<sub>2016</sub> molecular spectroscopic database. *Journal of Quantitative Spectroscopy and Radiative Transfer*, 203, 3–69.
- [33] Grell, G. A. & Freitas, S. R. (2014). A scale and aerosol aware stochastic convective parameterization for weather and air quality modeling. *Atmospheric Chemistry and Physics*, 14(10), 5233–5250.

- [34] Hasekamp, O., Lorente, A., Hu, H., Butz, A., Aan de Brugh, J., & Landgraf, J. (2019). Algorithm Theoretical Baseline Document for Sentinel-5 Precursor Methane Retrieval. (SRON-S5P-LEV2-RP-001, 2019).
- [35] Hill, T. & Nassar, R. (2019). Pixel size and revisit rate requirements for monitoring power plant CO<sub>2</sub> emissions from space. *Remote Sensing*, 11(13), 1608.
- [36] Horel, J., Splitt, M., Dunn, L., Pechmann, J., White, B., Ciliberti, C., Lazarus, S., Slemmer, J., Zaff, D., & Burks, J. (2002). MesoWest: Cooperative mesonets in the western United States. *Bulletin of the American Meteorological Society*, 83(2), 211–225.
- [37] Hu, H., Landgraf, J., Detmers, R., Borsdorff, T., aan de Brugh, J., Aben, I., Butz, A., & Hasekamp, O. (2018). Toward global mapping of methane with TROPOMI: First results and intersatellite comparison to GOSAT. *Geophysical Research Letters*, 45(8), 3682–3689.
- [38] International Energy Agency (IEA) (2017). World energy outlook 2017. Paris/IEA, Paris: OECD Publishing.
- [39] International Panel on Climate Change (IPCC) (2013). Climate change 2013: The physical science basis. contribution of working group i to the fifth assessment report of the intergovernmental panel on climate change. (IPCC, Cambridge University Press, New York, 2013).
- [40] Jacob, D. J., Turner, A. J., Maasakkers, J. D., Sheng, J., Sun, K., Liu, X., Chance, K., Aben, I., McKeever, J., & Frankenberg, C. (2016). Satellite observations of atmospheric methane and their value for quantifying methane emissions. *Atmospheric Chemistry and Physics*, 16(22), 14371–14396.
- [41] Jervis, D., McKeever, J., Gains, D., Varon, D. J., Germain, S., & Sloan, J. J. (2018). High-resolution CH<sub>4</sub> enhancement observations near industrial sites using the GHGSat-D demonstration satellite. Abstract presented at the American Geophysical Union 2018 Fall Meeting, Washington, DC, 10–14 December 2018.
- [42] Jervis, D., McKeever, J., Strupler, M., Gains, D., Tarrant, E., & Germain, S. (2019). Rapid design, build and characterization cycle of the GHGSat constellation. Abstract presented at the American Geophysical Union 2019 Fall Meeting, San Francisco, CA, 9–13 December 2019.
- [43] Jongaramrungruang, S., Frankenberg, C., Matheou, G., Thorpe, A. K., Thompson, D. R., Kuai, L., & Duren, R. (2019). Towards accurate methane point-source quantification from high-resolution 2D plume imagery. *Atmospheric Measurement Techniques*, 12(12), 6667–6681.
- [44] Kirschke, S., Bousquet, P., Ciais, P., Saunois, M., Canadell, J. G., Dlugokencky, E. J., Bergamaschi, P., Bergmann, D., Blake, D. R., Bruhwiler, L., Cameron-Smith, P., Castaldi, S.,

- Chevallier, F., Feng, L., Fraser, A., Heimann, M., Hodson, E. L., Houweling, S., Josse, B., Fraser, P. J., Krummel, P. B., Lamarque, J. F., Langenfelds, R. L., le Quéré, C., Naik, V., O'Doherty, S., Palmer, P. I., Pison, I., Plummer, D., Poulter, B., Prinn, R. G., Rigby, M., Ringeval, B., Santini, M., Schmidt, M., Shindell, D. T., Simpson, I. J., Spahni, R., Steele, L. P., Strode, S. A., Sudo, K., Szopa, S., van der Werf, G. R., Voulgarakis, A., van Weele, M., Weiss, R. F., Williams, J. E., & Zeng, G. (2013). Three decades of global methane sources and sinks. *Nature Geoscience*, 6(10), 813–823.
- [45] Kochanov, R. V., Gordon, I. E., Rothman, L. S., Wcisło, P., Hill, C., & Wilzewski, J. S. (2016). HITRAN Application Programming Interface (HAPI): A comprehensive approach to working with spectroscopic data. *Journal of Quantitative Spectroscopy and Radiative Transfer*, 177, 15–30.
- [46] Kort, E. A., Frankenberg, C., Costigan, K. R., Lindenmaier, R., Dubey, M. K., & Wunch, D. (2014). Four Corners: The largest U.S. methane anomaly viewed from space. *Geophysical Research Letters*, 41(19), 6898–6903.
- [47] Krings, T., Gerilowski, K., Buchwitz, M., Hartmann, J., Sachs, T., Erzinger, J., Burrows, J. P., & Bovensmann, H. (2013). Quantification of methane emission rates from coal mine ventilation shafts using airborne remote sensing data. *Atmospheric Measurement Techniques*, 6(1), 151–166.
- [48] Krings, T., Gerilowski, K., Buchwitz, M., Reuter, M., Tretner, A., Erzinger, J., Heinze, D., Pflüger, U., Burrows, J. P., & Bovensmann, H. (2011). MAMAP – a new spectrometer system for column-averaged methane and carbon dioxide observations from aircraft: retrieval algorithm and first inversions for point source emission rates. *Atmospheric Measurement Techniques*, 4(9), 1735–1758.
- [49] Kuze, A., Suto, H., Shiomi, K., Kawakami, S., Tanaka, M., Ueda, Y., Deguchi, A., Yoshida, J., Yamamoto, Y., Kataoka, F., Taylor, T. E., & Buijs, H. L. (2016). Update on GOSAT TANSO-FTS performance, operations, and data products after more than 6 years in space. *Atmospheric Measurement Techniques*, 9(6), 2445–2461.
- [50] Lagarias, J. C., Reeds, J. A., Wright, M. H., & Wright, P. E. (1998). Convergence properties of the Nelder-Mead simplex method in low dimensions. *SIAM Journal on Optimization*, 9(1), 112–147.
- [51] Levelt, P. F., Van den Oord, G. H. J., Dobber, M. R., Malkki, A., Visser, H., de Vries, J., Stammes, P., Lundell, J. O. V., & Saari, H. (2006). The Ozone Monitoring Instrument. *IEEE Transactions on Geoscience and Remote Sensing*, 44(5), 1093–1101.
- [52] Lyon, D. R., Zavala-Araiza, D., Alvarez, R. A., Harriss, R., Palacios, V., Lan, X., Talbot, R., Lavoie, T., Shepson, P., Yacovitch, T. I., Herndon, S. C., Marchese, A. J., Zimmerle, D.,

- Robinson, A. L., & Hamburg, S. P. (2015). Constructing a spatially resolved methane emission inventory for the Barnett Shale Region. *Environmental Science and Technology*, 49(13), 8147–8157.
- [53] Maasakkers, J., Jacob, D. J., Sulprizio, M. P., Scarpelli, T. R., Nesser, H., Sheng, J.-X., Zhang, Y., Hersher, M., Bloom, A. A., Bowman, K. W., Worden, J. R., Janssens-Maenhout, G., & Parker, R. J. (2019). Global distribution of methane emissions, emission trends, and OH concentrations and trends inferred from an inversion of GOSAT satellite data for 2010–2015. *Atmospheric Chemistry and Physics*, 19(11), 7859–7881.
- [54] Maasakkers, J. D., Jacob, D. J., Sulprizio, M. P., Turner, A. J., Weitz, M., Wirth, T., Hight, C., DeFigueiredo, M., Desai, M., Schmeltz, R., Hockstad, L., Bloom, A. A., Bowman, K. W., Jeong, S., & Fischer, M. L. (2016). Gridded national inventory of U.S. methane emissions. *Environmental Science and Technology*, 50(23), 13123–13133.
- [55] Martin, D. O. (1976). Comment on “the change of concentration standard deviations with distance”. *Journal of the Air Pollution Control Association*, 26, 145–147.
- [56] Mays, K. L., Shepson, P. B., Stirm, B. H., Karion, A., Sweeney, C., & Gurney, K. R. (2009). Aircraft-based measurements of the carbon footprint of Indianapolis. *Environmental Science and Technology*, 43(20), 7816–7823.
- [57] McKeever, J., Durak, B. O. A., Gains, D., Jervis, D., Varon, D. J., Germain, S., & Sloan, J. J. (2017). GHGSat-D: Greenhouse gas plume imaging and quantification from space using a Fabry-Perot imaging spectrometer. Abstract presented at the American Geophysical Union 2017 Fall Meeting, New Orleans, LA, 11–15 December 2017.
- [58] McLinden, C. A., Fioletov, V., Shephard, M. W., Krotkov, N., Li, C., Martin, R. V., Moran, M. D., & Joiner, J. (2016). Space-based detection of missing sulfur dioxide sources of global air pollution. *Nature Geoscience*, 9, 496–500.
- [59] Miller, S. M., Michalak, A. M., Detmers, R. G., Hasekamp, O. P., Bruhwiler, L. M. P., & Schwietzke, S. (2019). China’s coal mine methane regulations have not curbed growing emissions. *Nature Communications*, 10, 303.
- [60] Moeng, C. H., Dudhia, J., Klemp, J., & Sullivan, P. (2007). Examining two-way grid nesting for large eddy simulation of the PBL using the WRF model. *Monthly Weather Review*, 135, 2295–2311.
- [61] Molod, A., Takacs, L., Suarez, M., Bacmeister, J., Song, I. S., & Eichmann, A. (2012). The GEOS-5 atmospheric general circulation model: Mean climate and development from MERRA to Fortuna. Technical Report Series on Global Modeling and Data Assimilation, Volume 28, 2012.

- [62] Nassar, R., Hill, T. G., McLinden, C. A., Wunch, D., Jones, D., & Crisp, D. (2017). Quantifying CO<sub>2</sub> emissions from individual power plants from space. *Geophysical Research Letters*, 44(19), 10045–10053.
- [63] National Center for Atmospheric Research (NCAR) (2018). WRF User Guide, version 3.8. Available at: [http://www2.mmm.ucar.edu/wrf/users/docs/user\\_guide\\_V3.8/contents.html](http://www2.mmm.ucar.edu/wrf/users/docs/user_guide_V3.8/contents.html) (last access: 22 August 2017).
- [64] National Centers for Environmental Prediction (NCEP) (2000). NCEP FNL operational model global tropospheric analyses, continuing from July 1999. Available at: <https://doi.org/10.5065/D6M043C6>, updated daily.
- [65] Nelder, J. A. & Mead, R. (1965). A simplex method for function minimization. *The Computer Journal*, 7(4), 308–313.
- [66] Nottrott, A., Kleissl, J., & Keeling, R. (2014). Modeling passive scalar dispersion in the atmospheric boundary layer with WRF large-eddy simulation. *Atmospheric Environment*, 82, 172–182.
- [67] Nunalee, C. G., Kosović, B., & Bieringer, P. E. (2014). Eulerian dispersion modeling with WRF-LES of plume impingement in neutrally and stably stratified turbulent boundary layers. *Atmospheric Environment*, 9, 571–581.
- [68] of Utah, U. (2018). MesoWest database. Available at: <http://mesowest.utah.edu/> (last access: 21 November 2017).
- [69] Ong, C., Day, S., Halliburton, B., Marvig, P., & White, S. (2017). Regional methane emissions in NSW CSG basins. (Final Report, CSIRO, Australia, 2017).
- [70] Pandey, S., Gautam, R., Houweling, S., van der Gon, H. D., Sadavarte, P., Borsdorff, T., Hasekamp, O., Landgraf, J., Tol, P., van Kempen, T., Hoogeveen, R., van Hees, R., Hamburg, S. P., Maasakkers, J. D., & Aben, I. (2019). Satellite observations reveal extreme methane leakage from a natural gas well blowout. *Proceedings of the National Academy of Sciences of the United States of America*, 116(52), 26376–26381.
- [71] Pandey, S., Houweling, S., Hu, H., Sadavarte, P., Gautam, R., Hasekamp, O., Landgraf, J., Aben, I., & Tsivlidou, M. (2018). Early analysis of TROPOMI XCH<sub>4</sub> for detection and quantification of local CH<sub>4</sub> emissions. Abstract presented at the American Geophysical Union 2018 Fall Meeting, Washington, DC, 12 December 2018.
- [72] Pasquill, F. (1961). The estimation of the dispersion of wind-borne material. *The Meteorological Magazine*, 90(1063), 33–49.
- [73] Polonsky, I. N., O'Brien, D. M., Kumer, J. B., O'Dell, C. W., & the geoCARB Team (2014). Performance of a geostationary mission, geoCARB, to measure CO<sub>2</sub>, CH<sub>4</sub> and CO column-averaged concentrations. *Atmospheric Measurement Techniques*, 7(4), 959–981.

- [74] Pommier, M., McLinden, C. A., & Deeter, M. (2013). Relative changes in CO emissions over megacities based on observations from space. *Geophysical Research Letters*, 40(14), 3766–3771.
- [75] Rayner, P. J., Utembe, S. R., & Crowell, S. (2014). Constraining regional greenhouse gas emissions using geostationary concentration measurements: a theoretical study. *Atmospheric Measurement Techniques*, 7(10), 3285–3293.
- [76] Razavi, A., Clerbaux, C., Wespes, C., Clarisse, L., Hurtmans, D., Payan, S., Camy-Peyret, C., & Coheur, P.-F. (2009). Characterization of methane retrievals from the IASI space-borne sounder. *Atmospheric Chemistry and Physics*, 9(20), 7889–7899.
- [77] Rodgers, C. D. (2000). *Inverse methods for atmospheric sounding: Theory and practice* (Vol. 2). World scientific.
- [78] Roy, D. P., Wulder, M. A., Loveland, T. R., Allen, R. G., Anderson, M. C., Helder, D., Irons, J. R., Johnson, D. M., Kennedy, R., Scambos, T. A., Schaaf, C. B., Schott, J. R., Sheng, Y., Vermote, E. F., Belward, A. S., Bindschadler, R., Cohen, W. B., Gao, F., Hippel, J. D., Hostert, P., Huntington, J., Justice, C. O., Kilic, A., Kovalskyy, V., Lee, Z. P., Lymburner, L., Masek, J. G., McCorkel, J., Shuai, Y., Trezza, R., Vogelmann, J., Wynne, R. H., & Zhu, Z. (2014). Landsat-8: Science and product vision for terrestrial global change research. *Remote Sensing of Environment*, 145, 154–172.
- [79] Saunois, M., Bousquet, P., Poulter, B., Peregon, A., Ciais, P., Canadell, J. G., Dlugokencky, E. J., Etiope, G., Bastviken, D., Houweling, S., Janssens-Maenhout, G., Tubiello, F. N., Castaldi, S., Jackson, R. B., Alexe, M., Arora, V. K., Beerling, D. J., Bergamaschi, P., Blake, D. R., Brailsford, G., Brovkin, V., Bruhwiler, L., Crevoisier, C., Crill, P., Covey, K., Curry, C., Frankenberg, C., Gedney, N., Höglund-Isaksson, L., Ishizawa, M., Ito, A., Joos, F., Kim, H. S., Kleinen, T., Krummel, P., Lamarque, J. F., Langenfelds, R., Locatelli, R., Machida, T., Maksyutov, S., McDonald, K. C., Marshall, J., Melton, J. R., Morino, I., Naik, V., O'Doherty, S., Parmentier, F. J. W., Patra, P. K., Peng, C., Peng, S., Peters, G. P., Pison, I., Prigent, C., Prinn, R., Ramonet, M., Riley, W. J., Saito, M., Santini, M., Schroeder, R., Simpson, I. J., Spahni, R., Steele, P., Takizawa, A., Thornton, B. F., Tian, H., Tohjima, Y., Viovy, N., Voulgarakis, A., vanWeele, M., van der Werf, G. R., Weiss, R., Wiedinmyer, C., Wilton, D. J., Wiltshire, A., Worthy, D., Wunch, D., Xu, X., Yoshida, Y., Zhang, B., Zhang, Z., & Zhu, Q. (2016). The global methane budget 2000–2012. *Earth System Science Data*, 8(2), 697–751.
- [80] Scarpelli, T. R., Jacob, D. J., Maasakkers, J. D., Sulprizio, M. P., Sheng, J., Rose, K., Romeo, L., Worden, J., & Janssens-Maenhout, G. (2020). A global gridded ( $0.1^\circ \times 0.1^\circ$ ) inventory of methane emissions from oil, gas, and coal exploitation based on national reports to the United Nations Framework Convention on Climate Change. *Earth System Science Data*, 12(1), 563–575.

- [81] Schroeder, W., Oliva, P., Giglio, L., & Csiszar, I. A. (2014). The new VIIRS 375 m active fire detection data product: Algorithm description and initial assessment. *Remote Sensing of Environment*, 143, 85–96.
- [82] Schwandner, F. M., Gunson, M. R., Miller, C. E., Carn, S. A., Eldering, A., Krings, T., Verhulst, K. R., Schimel, D. S., Nguyen, H. M., Crisp, D., & O'Dell, C. W. (2017). Spaceborne detection of localized carbon dioxide sources. *Science*, 358(6360).
- [83] Skamarock, W. C., Klemp, J. B., Dudhia, J., Gill, D. O., Barker, D. M., Duda, M. G., Huang, X.-Y., Wang, W., & Powers, J. G. (2008). A description of the advanced research WRF version 3. NCAR Tech. Note NCAR/TN-475+STR, 113 pp., available at: <https://doi.org/10.5065/D68S4MVH>.
- [84] Sloan, J. J., Durak, B., Gains, D., Ricci, F., McKeever, J., Lamorie, J., Mark, S. D. A. O., Latendresse, V., Lavoie, J., & Kruzelecky, R. (2016). Fabry-Perot interferometer based satellite detection of atmospheric trace gases. US 9,228,897 B2, United States Patent and Trademark Office. Retrieved from <https://patentimages.storage.googleapis.com/85/4e/65/b3f964823f2f3b/US9228897.pdf>.
- [85] Smith, M. L., Gvakharia, A., Kort, E. A., Sweeney, C., Conley, S. A., Faloona, I., Newberger, T., Schnell, R., Schwietzke, S., & Wolter, S. (2017). Airborne quantification of methane emissions over the Four Corners Region. *Environmental Science and Technology*, 51(10), 5832–5837.
- [86] Thompson, D. R., Leifer, I., Bovensmann, H., Eastwood, M., Fladeland, M., Frankenberg, C., Gerilowski, K., Green, R. O., Kratwurst, S., Krings, T., Luna, B., & Thorpe, A. K. (2015). Real-time remote detection and measurement for airborne imaging spectroscopy: a case study with methane. *Atmospheric Measurement Techniques*, 8(10), 4383–4397.
- [87] Thompson, D. R., Thorpe, A. K., Frankenberg, C., Green, R. O., Duren, R., Guanter, L., Hollstein, A., Middleton, E., Ong, L., & Ungar, S. (2016). Space-based remote imaging spectroscopy of the Aliso Canyon CH<sub>4</sub> superemitter. *Geophysical Research Letters*, 43(12), 6571–6578.
- [88] Thorpe, A. K., Frankenberg, C., Aubrey, A. D., Roberts, D. A., Nottrott, A. A., Rahn, T. A., Sauer, J. A., Dubey, M. K., Costigan, K. R., Arata, C., Steffke, A. M., Hills, S., Haselwimmer, C., Charlesworth, D., Funk, C. C., Green, R. O., Lundein, S. R., Boardman, J. W., Eastwood, M. L., Sarture, C. M., Nolte, S. H., McCubbin, I. B., Thompson, D. R., & McFadden, J. P. (2016). Mapping methane concentrations from a controlled release experiment using the next generation airborne visible/infrared imaging spectrometer (AVIRIS-NG). *Remote Sensing of Environment*, 179, 104–115.
- [89] Tobin, D. C., Revercomb, H. E., Knuteson, R. O., Lesht, B. M., Strow, L. L., Hannon, S. E., Feltz, W. F., Moy, L. A., Fetzer, E. J., & Cress, T. S. (2006). Atmospheric Radiation Measure-

- ment site atmospheric state best estimates for Atmospheric Infrared Sounder temperature and water vapor retrieval validation. *Journal of Geophysical Research: Atmospheres*, 111(D9).
- [90] Tratt, D. M., Buckland, K. N., Hall, J. L., Johnson, P. D., Keim, E. R., Leifer, I., Westberg, K., & Young, S. J. (2014). Airborne visualization and quantification of discrete methane sources in the environment. *Remote Sensing of Environmnet*, 154, 74–88.
  - [91] Tratt, D. M., Young, S. J., Lynch, D. K., Buckland, K. N., Johnson, P. D., Hall, J. L., Westberg, K. R., Polak, M. L., Kasper, B. P., & Qian, J. (2011). Remotely sensed ammonia emission from fumarolic vents associated with a hydrothermally active fault in the Salton Sea Geothermal Field, California. *Journal of Geophysical Research: Atmospheres*, 116(D21).
  - [92] Turner, A. J., Jacob, D. J., Wecht, K. J., Maasakers, J. D., Lundgren, E., Andrews, A. E., Biraud, S. C., Boesch, H., Bowman, K. W., Deutscher, N. M., Dubey, M. K., Griffith, D. W. T., Hase, F., Kuze, A., Notholt, J., Ohyama, H., Parker, R., Payne, V. H., Sussmann, R., Sweeney, C., Velasco, V. A., Warneke, T., Wennberg, P. O., & Wunch, D. (2015). Estimating global and North American methane emissions with high spatial resolution using GOSAT satellite data. *Atmospheric Chemistry and Physics*, 15(12), 7049–7069.
  - [93] United States Environmental Protection Agency (EPA) (2006). Reducing emissions when taking compressors off-line. Available at [https://www.epa.gov/sites/production/files/2016-06/documents/l1\\_compressoroffline.pdf](https://www.epa.gov/sites/production/files/2016-06/documents/l1_compressoroffline.pdf).
  - [94] United States Environmental Protection Agency (EPA) (2017). Facility Level Information on Greenhouse Gases Tool (FLIGHT). Available at: <https://ghgdata.epa.gov/ghgp/service/html/2017?id=1009342&et=undefined> via <https://ghgdata.epa.gov/ghgp/main.do> (last access: 1 July 2019).
  - [95] United States Environmental Protection Agency (EPA) (2018). XTO energy well blowout—E18512—Removal Polrep—Initial Removal Polrep. (U.S. Environmental Protection Agency Pollution/Situation Report). Available at [https://www.fractracker.org/a5ej2osjfwe/wp-content/uploads/2018/03/XTOPowhatenPoint\\_polrep\\_1.pdf](https://www.fractracker.org/a5ej2osjfwe/wp-content/uploads/2018/03/XTOPowhatenPoint_polrep_1.pdf).
  - [96] United States National Aeronautics and Space Agency (NASA) (1976). U.S. Standard Atmosphere. (Technical Report NASA-TM-X-74335, NASA, 1976). Available at <https://ntrs.nasa.gov/search.jsp?R=19770009539>.
  - [97] Valin, L. C., Russell, A. R., & Cohen, R. C. (2013). Variations of OH radical in an urban plume inferred from NO<sub>2</sub> column measurements. *Geophysical Research Letters*, 40(9), 1856–1860.
  - [98] Varon, D. J., Jacob, D. J., Jervis, D., & McKeever, J. (in review). Quantifying time-averaged methane emissions from individual coal mine vents with GHGSat-D satellite observations. *Environmental Science and Technology*.

- [99] Varon, D. J., Jacob, D. J., McKeever, J., Jervis, D., Durak, B. O. A., Xia, Y., & Huang, Y. (2018). Quantifying methane point sources from fine-scale satellite observations of atmospheric methane plumes. *Atmospheric Measurement Techniques*, 11(10), 5673–5686.
- [100] Varon, D. J., McKeever, J., Jervis, D., Maasakkers, J. D., Pandey, S., Houweling, S., Aben, I., Scarpelli, T., & Jacob, D. J. (2019). Satellite discovery of anomalously large methane point sources from oil/gas production. *Geophysical Research Letters*, 46(22), 13507–13516.
- [101] Veefkind, J. P., Aben, I., McMullan, K., Förster, H., de Vries, J., Otter, G., Claas, J., Eskes, H. J., de Haan, J. F., Kleipool, Q., van Weele, M., Hasekamp, O., Hoogeveen, R., Landgraf, J., Snel, R., Tol, P., Ingmann, P., Voors, R., Kruizinga, B., Vink, R., Visser, H., & Levelt, P. F. (2012). TROPOMI on the ESA Sentinel-5 Precursor: A GMES mission for global observations of the atmospheric composition for climate, air quality and ozone layer applications. *Remote Sensing of Environment*, 120, 70–83.
- [102] White, W. H., Anderson, J. A., Blumenthal, D. L., Husar, R. B., Gillani, N. V., Husar, J. D., & Wilson, W. E. (1976). Formation and transport of secondary air pollutants: ozone and aerosols in the St. Louis urban plume. *Science*, 194(4261), 187–189.
- [103] Worden, J., Wecht, K., Frankenberg, C., Alvarado, M., Bowman, K., Kort, E., Kulawik, S., Lee, M., Payne, V., & Worden, H. (2013). CH<sub>4</sub> and CO distributions over tropical fires during October 2006 as observed by the Aura TES satellite instrument and modeled by GEOS-Chem. *Atmospheric Chemistry and Physics*, 13(7), 3679–3692.
- [104] Wunch, D., Toon, G. C., Blavier, J. F. L., Washenfelder, R. A., Notholt, J., Connor, B. J., Griffith, D. W. T., Sherlock, V., & Wennberg, P. O. (2011). The total carbon column observing network. *Philosophical Transactions of the Royal Society A: Mathematical, Physical and Engineering Sciences*, 369(1943), 2087–2112.
- [105] Zavala-Araiza, D. (2019). MethaneSAT: mapping global oil and gas methane emissions to accelerate mitigation. Abstract presented at the 2019 Industrial Methane Measurements conference, Rotterdam, NL, 22–23 May 2019.
- [106] Zavala-Araiza, D., Lyon, D., Alvarez, R. A., Palacios, V., Harriss, R., Lan, X., Talbot, R., & Hamburg, S. P. (2015). Toward a functional definition of methane super-emitters: Application to natural gas production sites. *Environmental Science and Technology*, 49(13), 8167–8174.
- [107] Zhang, Y., Gautam, R., Zavala-Araiza, D., Jacob, D. J., Zhang, R., Zhu, L., Sheng, J.-X., & Scarpelli, T. (2019). Satellite-observed changes in Mexico's offshore gas flaring activity linked to oil/gas regulations. *Geophysical Research Letters*, 46(3), 1879–1888.